ABSTRACT

Title of Dissertation: **EXPERIMENTAL INVESTIGATION OF THE LIPID-BINDING MECHANISM OF OSH4 PROTEIN**

Dinara Konakbayeva, Doctor of Philosophy, 2024

Dissertation directed by: Professor Amy J. Karlsson, Department of Chemical and Biomolecular Engineering

Recent findings show that intracellular lipid traffic between organelles primarily occurs through a non-vesicular pathway involving lipid transport proteins (LTPs) and is facilitated by areas of close apposition between two organelles so called membrane contact sites (MCS). Oxysterol-binding homologue (Osh) proteins in the yeast *Saccharomyces cerevisiae* serve as examples of LTPs. Osh proteins are crucial for transporting signaling lipids and are believed to form MCSs. In this study, we examined the binding mechanism of the Osh4 protein, aiming to gain a better understanding of its explicit membrane-binding mechanism.

The Osh4 protein possesses an α-helical binding domain known as the amphipathic lipid-packing sensor (ALPS)-like motif. Our approach involved utilizing experimental methods to examine the biophysical interactions of both the ALPS peptide and the full-length Osh4 protein. To investigate the binding interactions of ALPS with membranes of different lipid compositions, we

examined its interactions with three different mixtures of 1-palmitoyl-2-oleoyl-sn-glycero-3-phosphocholine (POPC; has a zwitterionic head group) and 1-palmitoyl-2-oleoyl-sn-glycero-3-phospho-L-serine (POPS; has a negatively charged head group)—1:1 POPC-POPS, 4:1 POPC-POPS, and 9:1 POPC-POPS—as well as pure POPC.

To understand the structural changes in ALPS and model membranes during peptide-membrane interactions, we performed a series of experimental studies. Circular dichroism (CD) was used to study the changes in the secondary structure of ALPS in different environments. The CD data indicated that the α-helical conformation of the ALPS peptide was more pronounced in the presence of POPC-POPS liposomes, especially with a higher content of POPS lipid, compared to liposomes composed entirely of POPC. This observation underscores the significant influence of anionic lipids in the facilitation of peptide folding at the membrane-water interface. X-ray diffraction was utilized to study the changes in membrane structure upon ALPS binds to it. The X-ray diffraction results showed that the ALPS peptide caused thinning of the multilayer with an increased POPS lipid ratio. This could be due to the electrostatic interaction of the positively charged Lys residue in the ALPS sequence with the anionic POPS lipid. We also studied the binding of the peptide to membranes by observing changes in the Trp fluorescence emission spectrum of ALPS upon the addition of liposomes. We observed a blue shift in the fluorescence emission maximum of Trp with higher POPS content. This suggests that the ALPS peptide was experiencing a more hydrophobic and less polar environment in the presence of the liposomes, indicating possible penetration of the peptide into the hydrocarbon region of the bilayer. The blue shifts of Trp emission in the presence of POPS liposomes were higher than those observed with POPC liposomes and suggest that the ALPS peptide binds better to charged POPS lipids, which is consistent with the X-ray diffraction data.

We also conducted Trp fluorescence titration and ITC experiments to gain deeper insights into the binding affinity of the ALPS peptide to a model membrane. Using fluorescence data, we estimated the binding constant for the binding of ALPS to liposomes by performing titration measurements of vesicles with the ALPS peptide. Our analysis demonstrated that ALPS binding to 4:1 POPC-POPS lipid membranes had a K_d of 1.88 ± 0.47 μM, which corresponds to a free energy change (ΔG) of -7.82 ± 0.15 kcal/mol. Additionally, the ITC experiments performed with the same vesicles yielded a ΔG of -4.41± 0.04 kcal/mol. This result is slightly less than the ΔG value of -7.82 ± 0.15 kcal/mol obtained from fluorescence spectroscopy titration. The observed discrepancy of -3.41 kcal/mol may indicate the energy associated with the folding of the ALPS peptide.

In order to understand how Osh4 forms MCSs between two membranes, we need to examine how the membranes interact with the full-length protein. The first step to achieve this is to produce the protein through recombinant protein production methods. After evaluating two different fusion tags, glutathione S-transferase (GST) and small ubiquitin-related modifier (SUMO), it was found that the SUMO tag resulted in higher protein yield and greater protein purity. Our work lays the foundation for future experiments with the full-length Osh4 protein to improve our understanding of the mechanisms of lipid transport between membranes.

Our results emphasize the ALPS peptide's selectivity for specific lipid environments, particularly its affinity for anionic lipids. We demonstrated that the presence of anionic lipids is crucial for the motif's ability to induce conformational changes upon binding to a membrane, and these conformational changes likely play a critical role in intracellular lipid trafficking and membrane organization.

EXPERIMENTAL INVESTIGATION OF THE LIPID-BINDING MECHANISM OF OSH4 PROTEIN

by

Dinara Konakbayeva

Dissertation submitted to the Faculty of the Graduate School of the
University of Maryland, College Park, in partial fulfillment
of the requirements for the degree of
Doctor of Philosophy
2024

Advisory Committee:
Professor Amy J. Karlsson, Chair
Professor Jeffery B. Klauda
Professor Ella Mihailescu
Professor Sergei Sukharev
Professor Taylor J. Woehl

Dedication

I dedicate my PhD dissertation to my mom, my late grandmom, and my grandad for all the encouragement and support they provided me throughout my PhD studies.

Acknowledgments

I want to express my heartfelt appreciation to my mentor, Dr. Amy J. Karlsson, for her invaluable guidance, encouragement, and friendship. Her personal attention, research expertise, and academic support have been instrumental in shaping my professional development and personal growth. I am deeply grateful for the time and effort she has invested in me and feel honored to have had the opportunity to work under her supervision.

I would also like to thank the fellow graduate students who made valuable contributions to the research, including Wright Makambi, Marzyeh Kheradmand-Hajibashi, Futoon Al-Jirafi, Faraz Ahmed Burni, and Ren-Jhe Chung. They always extended help when I needed it most and created a welcoming research environment that was enjoyable to work in. I also thank Dr. Shakiba Nikfarjam for guiding me on how to run a chromatography purification and advising me to replace the GST expression tag with the SUMO tag. Dr. Madolyn Britt and Jessica Bodosa assisted in running and analyzing isothermal titration calorimetry (ITC) experiments. Dr. Robert Allsopp and Dr. Sharmistha Karmakar were great collaborators on the project.

I would like to thank the National Science Foundation (Award # 1951425) for making this research possible. I also want to express my sincere gratitude to Dr. Jeffery Klauda for his invaluable guidance, support, and collaboration on this project. I am also deeply thankful to Dr. Ella Mihailescu from the Institute for Bioscience and Biotechnology Research, whose extensive help with running and analyzing X-ray diffraction experiments was crucial for the success of this project. My heartfelt thanks

also go to Dr. Sergei Sukharev from the Department of Biology for his training and guidance on running ITC experiments, and to Dr. Daoning Zhang from the NMR Facility and Dr. Mary F. Roberts from Boston College, whose assistance in collecting the field cycling NMR data was beneficial. I would also like to thank Dr. Taylor J. Woehl and Dr. Srinivasa R. Raghavan for their kind permission to use the fluorometer and nitrogen gas, respectively.

Finally, I would like to express my sincere gratitude to my mom, Altyngul, as well as my grandparents and my closest friends from Kazakhstan–Alina, Akzhunis, Gulnaz, Dinara, Madina, Bota, and Tima. I am also extremely grateful to my close friend from Morocco, Ilham, for their unwavering encouragement and support throughout my PhD journey.

.

Table of Contents

Dedication ..... **ii**
Acknowledgments ..... **iii**
List of Tables ..... **vii**
List of Figures ..... **viii**
List of Abbreviations ..... **xii**
1. Chapter 1: Background and motivation **1**
1.1. Biological membranes 1
1.2. Membrane composition 1
1.3. Membrane dynamics 5
1.4. Transport of lipids 6
1.5. LTPs 9
1.5.1. ALPS 10
1.5.2. Osh4 11
1.6. Experimental biophysical methods for lipid-protein interactions 13
1.6.1. CD 13
1.6.2. Tryptophan fluorescence 15
1.6.3. Isothermal titration calorimetry 18
1.6.4. X-ray diffraction 21
1.7. Overview of dissertation 23
2. Chapter 2: ALPS-like peptide of the Osh4 protein **24**
2.1. Introduction 24
2.2. Methods 27
2.2.1. Peptide synthesis and preparation 27
2.2.2. Liposome preparation 27
2.2.3. Circular dichroism 28
2.2.4. X-ray diffraction 28
2.2.5. Fluorescence spectroscopy 29
2.2.6. Isothermal titration calorimetry 31
2.3. Result and discussion 32
2.3.1. ALPS peptide structure 32
2.3.2. ALPS membrane interaction 35
2.3.3. ALPS binding influences membrane structure 38
2.4 Binding affinity of ALPS to membranes 41
2.4. Conclusions 48
3. Chapter 3: Production and Purification of Osh4 ..... **49**
3.1. Introduction 49
3.2. Methods 50
3.2.1. Plasmid construction: (pGEX4T1-GST-TEV site-Osh4) 50
3.2.2. Plasmid construct: (pGEX4T1-GST-FactorXa site-Osh4) 51
3.2.3. Plasmid construct: (pET41a+-6×His-SUMO-Osh4(D191C)) 52
3.2.4. Site-directed mutagenesis 54
3.3. Protein expression and preparation 55
3.4. Media optimization 56

3.5. Cell strain optimization 56
3.6. Protein extraction and purification 57
3.6.1. GST-Osh4 constructs 57
3.6.2. 6×His-SUMO-Osh4 construct 59
3.7. Results and discussion 61
3.7.1. Plasmid construct: (pET41a+-6×His-SUMO-Osh4(D191C)) 61
3.8. Protein expression and preparation 61
3.9. Media optimization 63
3.10. Cell strain optimization 64
3.11. Protein extraction and purification 65
3.11.1. GST-Osh4 constructs 65
3.11.2. 6×HisSUMO-Osh4 construct 66
3.12. Conclusions 68
4. Chapter 4: Conclusion and future work 70
4.1. Neutron diffraction 71
4.2. NMR and high resolution field cycling NMR 72
4.3. Cryo-EM 79
Appendices 81
References 84

List of Tables

1. Chapter 1: Background and motivation
Table 1.1. Phospholipid composition of various subcellular compartments S*accharomyces cerevisiae.* Reproduced from Ref. [13]. 5

2. Chapter 2: ALPS-like peptide of the Osh4 protein
Table 2.1. Percentages of secondary structure elements of ALPS in different environments. 35
Table 2.2. Blue shift of Trp fluorescence in ALPS due to interaction with liposomes of varying composition and concentration. 37
Table 2.3. The membrane parameters obtained from x-ray diffraction measured in the presence and absence of ALPS at a peptide to lipid molar ratio of 1:25 measured at 298 K and 308 K. 40
Table 2.4. Thermodynamic parameters for the ALPS peptide binding to the LUVs vesicle obtained from ITC. 44

3. Chapter 3: Production and Purification of Osh4
Table 3.1. Oligonucleotides used for the site-directed mutagenesis. 54

List of Figures

1. Chapter 1: Background and motivation

Figure 1.1. The structure of plasma membrane. Image reprinted, with permission, from Ref. *[5]* © (2017) Elsevier. 2

Figure 1.2. Schematic diagram of three types of membrane lipids. Image reprinted from Ref. *[6]* with some modifications. Frontiers and CC BY 4.0 DEED do not require any special permission to reprint images. 2

Figure 1.3. Mechanisms of non-vesicular lipid transport include monomeric lipid exchange, lateral diffusion, and transbilayer flip-flop. In monomeric lipid exchange, lipids are transferred between membranes either spontaneously or with the help of LTPs. LTPs can transfer a lipid to the acceptor membrane or exchange it with another lipid from the acceptor membrane. Lateral diffusion of lipids occurs within the same layer of the membrane. The transfer of lipids between the two opposite layers of the bilayer, also known as transbilayer flip-flops, can occur spontaneously or with the help of proteins such as flippases and translocases. Image reprinted, with permission, from Ref. *[19]* © (2010) Springer Nature. 7

Figure 1.4. Proposed diagram showing how an LTP facilitates MCS formation. The red domain binds to the membrane at the top and the green domain binds to another membrane at the bottom. Created with BioRender.com. 8

Figure 1.5. Helical wheel of Osh4's ALPS-like peptide. Hydrophobic residues are color-coded white, polar residues are color-coded green, and the charged residue (+) is highlighted in blue. The wheel was created with Heliquest (https://heliquest.ipmc.cnrs.fr/). (Data courtesy of Dr. Jeffery Klauda and Dr. Robert Allsopp) 10

Figure 1.6. Structure of the Osh4 protein, where the domains responsible for targeting the membrane are highlighted in color. Image reprinted, with permission, from Ref. *[9]* © (2022) Elsevier. 12

Figure 1.7. Standard CD spectra redrawn by *[49]* from *[50]*. Image reprinted, with permission and some modifications, from Ref. *[49]* © (2014) Elsevier. Secondary structures were created with BioRender.com. 14

Figure 1.8. Tryptophan fluorescence spectra of a protein before (black line) and after (red line). Image reprinted from Ref *[61]*. MDPI does not require any special permission to reprint images. 17

Figure 1.9. The fundamental concept of isothermal titration calorimetry: A) schematic diagram of ITC instrument where lipid in the syringe is titrated into the sample cell, B) typical ITC thermogram where the top plot is a raw data plot of heat flow over time and the bottom plot is integrated heats upon injection (black circles) and the data fit of the raw data (black line). Image reprinted, with permission and some modification, from Ref *[73]* © (2022) American Chemical Society. 20

Figure 1.10. Illustration of the conditions necessary for X-ray reflection according to Bragg's law. Image reprinted, with permission, from Ref *[78]* © (2023) Elsevier. ... 22

2. Chapter 2: ALPS-like peptide of the Osh4 protein

Figure 2.1. Domain structure of Osh4 with ALPS highlighted in red. (Figure 25
Figure 2.2. Structure of POPC and POPS lipids. Image reprinted, with permission, from Ref. [85] © (2022) Springer Nature. Some modifications were applied. 26
Figure 2.3. CD spectra of 45 μM ALPS peptide in the form of mean residue ellipticity measured in water, TFE (and in the presence of large uniamellar vesicles (LUVs) composed of POPC and POPC-POPS lipids. The final concentration of lipids was 1.125 mM in water. The temperature was maintained at 298 K. Each experiment was reported as an average of 3 scans. 34
Figure 2.4. Fluorescence of Trp of ALPS peptide (20 μM) alone and in the presence of POPC liposomes and POPC-POPS liposomes. Liposomes were prepared at three molar ratios of POPC to POPS lipids with total lipid concentrations of 1-4 mM. 37
Figure 2.5. MD simulations of the ALPS peptide bound to a membrane with 4:1 POPC-POPS. (Data courtesy of Dr. Jeffery Klauda and Dr. Robert Allsopp). 38
Figure 2.6. X-ray density profile of POPC-POPS bilayers alone and in the presence of ALPS at a peptide to lipid molar ratio of 1:25 and at 97% relative humidity measured **A-B)** at 298 K and **C-D)** at 308 K. 40
Figure 2.7. Fluorescence intensities resulting from the titration of 20 μM ALPS with 4:1 POPC-POPS liposomes at 298 K. The blue dots represent the corrected peak intensity changes using Trp zwitterion fluorescence as a reference, and the red line represents the fits to the corrected intensities. Error bars represent standard error of the mean (n = 2). 42
Figure 2.8. ITC thermogram of POPC liposomes (100 nm average size) titrated into the cell containing 100-150 μM ALPS peptide solution. The heat (*Q*) released or absorbed as a result of the interaction was measured at 298 K. The upper plot shows the raw data generated by the series of liposome injections, while the lower plot illustrates the binding isotherm resulting from the integration of each injection peak. The experiments were repeated at least three times. The buffer consisted of 50 mM KCl, 9.3 mM K_2HPO_4, and 0.7 mM KH_2PO_4 (pH=7). The heat of dilution was consistently negligible; thus, it was not deducted from the reaction heat. 45
Figure 2.9. ITC thermogram of 4:1 POPC-POPS liposomes (100 nm average size) titrated into the cell containing 100-150 μM ALPS peptide solution. The heat (*Q*) released or absorbed as a result of the interaction was measured at 298 K. The upper plot shows the raw data generated by the series of liposome injections, while the lower plot illustrates the binding isotherm resulting from the integration of each injection peak. The experiments were repeated at least two times. The buffer consisted of 50 mM KCl, 9.3 mM K_2HPO_4, and 0.7 mM KH_2PO_4 (pH=7). The heat of dilution was consistently negligible; thus, it was not deducted from the reaction heat. 46
Figure 2.10. ITC thermogram of 3:1 POPC-POPA liposomes (100 nm average size) titrated into the cell containing 100-150 μM ALPS peptide solution. The heat (*Q*) released or absorbed as a result of the interaction was measured at 298 K. The upper plot shows the raw data generated by the series of liposome injections, while the lower plot illustrates the binding isotherm resulting from the integration of each injection peak. The experiments were repeated only one time. The buffer consisted of

50 mM KCl, 9.3 mM K_2HPO_4, and 0.7 mM KH_2PO_4 (pH=7). The heat of dilution was consistently negligible; thus, it was not deducted from the reaction heat. 47

3. Chapter 3: Production and Purification of Osh4
Figure 3.1. Plasmid map of pGEX4T1-GST-TEVsite-Osh4. 51
Figure 3.2. Plasmid map of pGEX4T1-GST-Factor Xa site-Osh4. 52
Figure 3.3. Plasmid map of pET41a+-6×His-SUMO-Osh4(ΔC-D191C). 53
Figure 3.4. Schematic diagram of purification of GST-Osh4 constructs. Figure made in BioRender.com. 58
Figure 3.5. Schematic diagram of purification of GST-Osh4 constructs. Figure made in BioRender.com. 60
Figure 3.6. **A)** Amplified Osh4 protein's gene with ΔC-D191C mutation **B)** Digested pET41a+-6×His-SUMO plasmid **C)** Ligation product pET41a+-6×His-SUMO-Osh4(ΔC-D191C). 61
Figure 3.7. A) Expression of the GST-TEV site -Osh4 fusion protein. **B)** Expression of the GST-Factor Xa site -Osh4 fusion. Both fusion proteins were expressed in BL21(DE3) cells at 37 °C for 5 h with 100 μM IPTG. The Western blots were probed using an anti-GST (rabbit) antibody. 62
Figure 3.8. Expression of the 6×His-SUMO-Osh4 fusion protein which was expressed in BL21(DE3) cells at 37 °C for 5 h with 0.1 mM IPTG. The Western blots were probed using an anti-6×His (rabbit) antibody. 63
Figure 3.9. Expression of the GST-TEV site -Osh4 fusion protein, which was expressed in BL21(DE3) cells in three different media (LB. TB, and SB) at 37 °C for 5 h with 100 μM IPTG. Western blots were probed using an anti-GST (rabbit) antibody. To eliminate any variations between the samples, each of them was loaded into three wells. 64
Figure 3.10. Expression of the GST-Factor Xa site -Osh4 fusion protein, which was expressed in four different *E. coli* strains (DH5α, BL21, BL21(DE3), AND MC4100) at 37 °C for 5 h with 0.1 mM IPTG. Western blots were probed using an anti-GST (rabbit) antibody. 65
Figure 3.11. A) Purified and 3-fold concentrated Osh4 protein solution from the GST-TEV site-Osh4 fusion protein construct visualized via gel electrophoresis. **B)** Purification stages of the GST-Factor Xa site-Osh4 fusion protein visualized via gel electrophoresis. The image shows protein fractions collected at different purification steps: the initial eluate from the glutathione agarose column (GCE1), the overnight Factor Xa cleavage product (CLV), the dialyzed cleavage solution (CLV&D), the flow-through from a subsequent glutathione agarose column (GF2), and the final flow-through from the benzamidine-agarose column (FXaC) used for the removal of Factor Xa protease. The bands corresponding to the GST-Factor Xa site-Osh4 fusion protein (75.8 kDa) and the cleaved Osh4 protein (50 kDa) are indicated with arrows.The purity assessment of the fusion proteins was evaluated using Coomassie Brilliant Blue staining. 66
Figure 3.12. Size exclusion chromatogram of the 6xHisSUMO-Osh4 fusion protein compared to the gel filtration standard (Bio-Rad). 67
Figure 3.13. Purification stages of the 6×His-SUMO-Osh4 fusion protein. The purification process and purity assessment of the fusion proteins were monitored

using Coomassie Brilliant Blue staining. Displayed are the fractions obtained from the initial immobilized metal affinity chromatography (MA1), followed by size exclusion chromatography (SE). Subsequent cleavage with SUMO protease is depicted (CLV), along with the resulting flow-through from a second round of immobilized metal affinity chromatography (MA2). 68

4. Chapter 4: Conclusion and future work

Figure 4.1. The ^{1}H NMR spectrum of vesicles containing POPC (5 mM) lipids sealed in a 5-mm NMR tube (524-PP-7 Wilmad-LabGlass) in ultrapure water measured by 600 MHz Bruker Ultrashield Plus NMR Spectrometer with BBFO probe. 73
Figure 4.2. ^{31}P spectra from a T_1 experiment for POPC (10 mM) liposomes (100 nm in diameter) sealed in a 5-mm NMR tube (524-PP-7 Wilmad-LabGlass) in ultrapure water measured by 600 MHz Bruker Ultrashield Plus NMR Spectrometer with BBFO probe. The relaxation delay time, τ, in seconds spent is indicated next to each spectrum. 75
Figure 4.3.Peak fitting of ^{31}P spectra from a T_1 experiment for POPC (10 mM)..... 76
Figure 4.4. ^{31}P R_1 as function of magnetic field for 5 mM POPC in SUVs with 5mM d3-DOPMe. Image reprinted, with permission, from Ref. [108] © (2004) American Chemical Society Publications. 77
Figure 4.5. Peak fitting of ^{31}P high resolution field cycling NMR spectra from a T_1 experiment for POPC (10 mM) measured at: **A)** 0.5 T and **B)** at 9.8 T. 78

List of Abbreviations

ALPS: amphipathic lipid-packing sensor
CD: circular dichroism
CL: cardiolipin
d: interplanar spacing between rows of (i.e atoms, ions, molecules), also known as a repeat distance in the multilayered lipid sample
ER: endoplasmic reticulum
ITC: isothermal titration calorimetry
Ka: binding affinity
LB: Luria-Bertani broth
LTP: lipid transfer proteins
MCS: membrane contact site
MD: molecular dynamic simulations
ND: not detectable
NMR: nuclear magnetic resonance
OD: optical density
ORP: oxysterol-binding protein (OSBP)-related protein
OSBP: oxysterol-binding protein
Osh: oxysterol-binding homology protein
PA: phosphatidic acid
PC: phosphatidylcholine
PE: phosphatidylethanolamine
PI: phosphatidylinositol
PIP: phosphoinositide
PM: plasma membrane
POPA: 1-palmitoyl-2-oleoyl-sn-glycero-3-phosphate
POPC: 1-palmitoyl-2-oleoyl-glycero-3-phosphocholine
POPS: 1-palmitoyl-2-oleoyl-sn-glycero-3-phospho-L-serine
PS: phosphatidylserine
SM: sphingomyelins
TGN: trans-Golgi network

1. Chapter 1: Background and motivation

1.1. Biological membranes

Biological membranes play a vital role in cellular function by acting as dynamic barriers that protect cells from the outer environment while also facilitating internal organization [1]. These membranes consist mainly of lipids, which are amphiphilic molecules that can self-arrange into a bilayer. The specific composition of the membrane is tailored to interact with specific proteins and small molecules, allowing for diverse functionality [2]. This diversity is essential to maintain cellular health and survival. Within a single membrane, different regions have distinct lipid distributions, creating specialized areas known as lipid rafts or domains that serve specific functions [3]. These specialized regions ensure that only specific proteins interact with particular parts of the membrane, enabling proper cellular function.

1.2. Membrane composition

Biological membranes have a bilayer structure made up of lipid molecules, which is commonly referred to as the phospholipid bilayer. Along with various lipid types, membrane proteins and oligosaccharides (sugars) are important components of this structure as shown in **Figure 1.1** [1, 4]. Sugars are exclusively found on one side of the bilayer and are covalently bonded to specific lipids and proteins [1]. Membrane proteins play a crucial role in maintaining structural integrity, organization, and facilitating material flow across membranes.

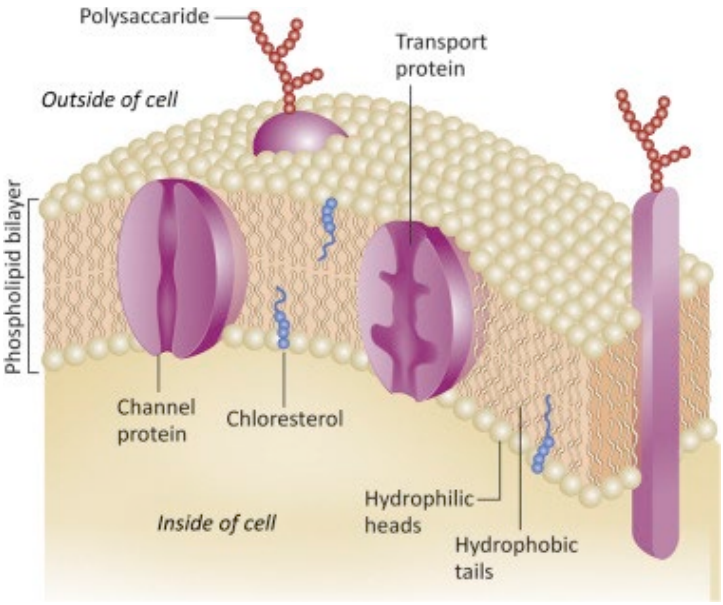

Figure 1.1. The structure of plasma membrane. Image reprinted, with permission, from Ref. *[5]* © (2017) Elsevier.

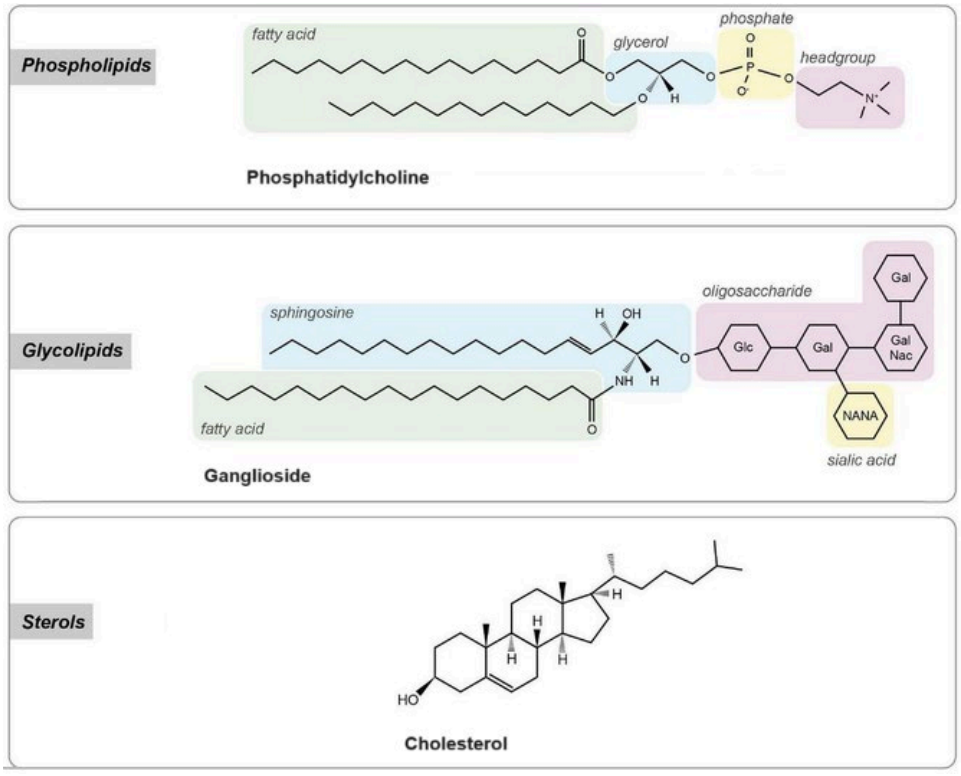

Figure 1.2. Schematic diagram of three types of membrane lipids. Image reprinted from Ref. *[6]* with some modifications. Frontiers and CC BY 4.0 DEED do not require any special permission to reprint images.

Three main lipid types populate biological membranes: phospholipids, glycolipids, and sterols (**Figure 1.2**). Phospholipids are among the most prevalent types of lipids found in cellular membranes [4]. Phospholipids such as phosphatidylcholine (PC) consist of fatty acid chains linked by glycerol to a phosphate group. Phosphatidylserine (PS) and phosphatidylethanolamine (PE) are examples of glycerophospholipids, with serine and ethanolamine respectively attached to their phosphate groups. Sphingophospholipids like sphingomyelin are based on sphingosine. Glycolipids are a type of lipid molecule that have a carbohydrate group covalently bonded to them through a glycosidic linkage. Sterols, predominantly cholesterol in vertebrates, stigmasterol in plants, and ergosterol in yeast and other fungi, possess distinct structures compared to other lipids [7]. Because of their structural diversity, sugars attached to lipids and proteins serve as markers. Carbohydrate markers on diseased cells aid in diagnosis and treatment [8]. All membrane lipids have amphipathic properties, containing both hydrophilic and hydrophobic regions. This characteristic allows lipids to spontaneously form bilayers with hydrophilic heads facing outward towards the aqueous environment and hydrophobic tails inward [4].

Organelles within cells have diverse lipid landscapes that exhibit notable structural and functional variety. Sterols, a vital component of cell membranes, are present in the highest concentration (~40%) at the plasma membrane (PM). However, its level is substantially low (~5%) at its production site, which is the endoplasmic reticulum (ER) [9]. Since most lipids are synthesized at the ER, they must be effectively transported to other organelles to maintain such lipid diversity.

A fundamental feature of cellular PMs are lipid asymmetry. This leads to different properties of the bilayer leaflets due to different lipid compositions, which influences the physical properties of bilayers and affects various cellular functions [10]. For instance, the extracellular leaflet of PMs is primarily enriched in PC and sphingomyelins (SM), dominant sphingolipid in mammalian membranes. In contrast, cytoplasmic leaflet is composed of PS and PE lipids [11]. Similarly, aminophospholipids predominantly reside in the inner leaflet, while cholinephospholipids are largely found in the outer leaflet [12].

Asymmetric distribution of lipids across phospholipid bilayers generates a charge disparity, with the negative charge of PS lipids at neutral pH contributing to a more negatively charged cytosolic side compared to the exterior [4]. Other lipids like PE, PC, and SM, being neutral, do not affect the charge balance.

Zinser et al. [13] summarized the percentage of different phospholipids extracted from yeast subcellular membranes as shown in Table 1.1. Among all the membrane fractions tested, phosphatidylcholine, phosphatidylethanolamine, phosphatidylinositol, and phosphatidylserine are the most abundant glycerophospholipid classes. PC lipids are found in greater quantities in subcellular membranes with the exception of the PM. Cardiolipin is found in significant quantities in the mitochondrial inner membrane (16% of total phospholipids) as well as in the outer mitochondrial membrane (6% of total phospholipids) and peroxisomal membrane (7% of total phospholipids). The diverse lipid composition of various subcellular compartments within a cell significantly impacts bilayer properties and must be taken into account in studies of lipid-protein interactions.

Table 1.1. Phospholipid composition of various subcellular compartments S*accharomyces cerevisiae.* Reproduced from Ref. [13].

Subcellular fraction	**PC** [a], **%**	**PE** [b], *%*	**PI** [c], *%*	**PS** [d], *%*	**CL** [e], *%*	**PA** [f], *%*	**Others** [b], *%*
Plasma membrane	16.8	20.3	17.7	33.6	0.2	3.9	6.9
Secretory vesicles	35	22.3	19.1	12.9	0.7	1.2	8.8
Vacuoles	46.5	19.4	18.3	4.4	1.6	2.1	7.7
Nucleus	44.6	26.9	15.1	5.9	<1.0	2.2	4.3
Peroxisomes	48.2	22.9	15.8	4.5	7	1.6	ND [h]
Light microsomes	51.3	33.4	7.5	6.6	0.4	0.2	0.5
Mitochondria	40.2	26.5	14.6	3	13.3	2.4	ND [h]
Inner mitochondrial membrane	38.4	24	16.2	3.8	16.1	1.5	ND [h]
Outer mitochondrial membrane	45.6	32.6	10.2	1.2	5.9	4.4	ND [h]

[a] PC – phosphatidylcholine
[b] PE – phosphatidylethanolamine
[c] PI – phosphatidylinositol
[d] PS – phosphatidylserine
[e] CL – cardiolipin
[f] PA – phosphatidic acid
[g] Others – other phospholipids
[h] ND – not detectable

1.3. Membrane dynamics

Although biological membranes are commonly illustrated using static diagrams, they are dynamic structures, and each individual phospholipid molecule is highly mobile [10, 14]. The fluid mosaic model, a fundamental model of the cell membrane structure proposed by Seymour Jonathan Singer and Garth L. Nicolson in 1972 [15], represents membranes as fluid bilayers of lipids in which proteins are embedded. This

fluidity gives membrane flexibility, enabling cells to alter their shape, divide, and fuse. The fatty acid tails of phospholipids can flex and spin freely on their head-to-tail axis. Additionally, within a single membrane leaflet, phospholipids and protein can diffuse laterally [1]. The fluid mosaic model of cell membranes provides a comprehensive explanation of how the structure and behavior of cell membranes are influenced by various factors such as temperature, lipid composition, and cholesterol level [15].

1.4. Transport of lipids

Lipids are predominantly synthesized within the ER before being distributed to various organelles [16]. The internal trafficking of lipids involves two main routes — vesicular and non-vesicular mechanisms. The vesicular route involves the use of small sacs made of lipids called vesicles, which transport lipids from one organelle to another. On the other hand, the non-vesicular mechanism does not involve vesicles and operates via direct transfer of lipids between organelles. Certain cellular compartments such as mitochondria, chloroplasts, and lipid droplets that cannot obtain sufficient lipids by vesicular routes necessitate an alternative mode of lipid delivery, highlighting the importance of non-vesicular transport [17].

In addition, cells can modify their lipid composition more accurately and quickly through non-vesicular lipid transport compared to vesicular trafficking. This pathway is particularly helpful during stressful conditions when vesicular trafficking is limited [18]. However, the mechanism by which lipids reach their intended destinations is not yet completely understood.

Lev [19], in his review of non-vesicular lipid transport, states that there are three mechanisms of lipid movement in and between biological membranes: monomeric lipid exchange, lateral diffusion, and transbilayer flip-flop (**Figure 1.3**). In monomeric lipid exchange, lipids are transported between different membranes and this process does not require energy from metabolism and can occur spontaneously or with the help of lipid transfer proteins (LTPs) [19]. In lateral diffusion, lipid movement can also occur within each leaflet of the lipid bilayer [20]. The movement of lipids between a membrane's leaflets is called transbilayer flip-flop, which can be facilitated by proteins like flippases, translocases, and scramblases. While flip-flop does not directly enable lipid transfer between organelles, it indirectly impacts vesicle formation and dynamics by modifying membrane curvature [21].

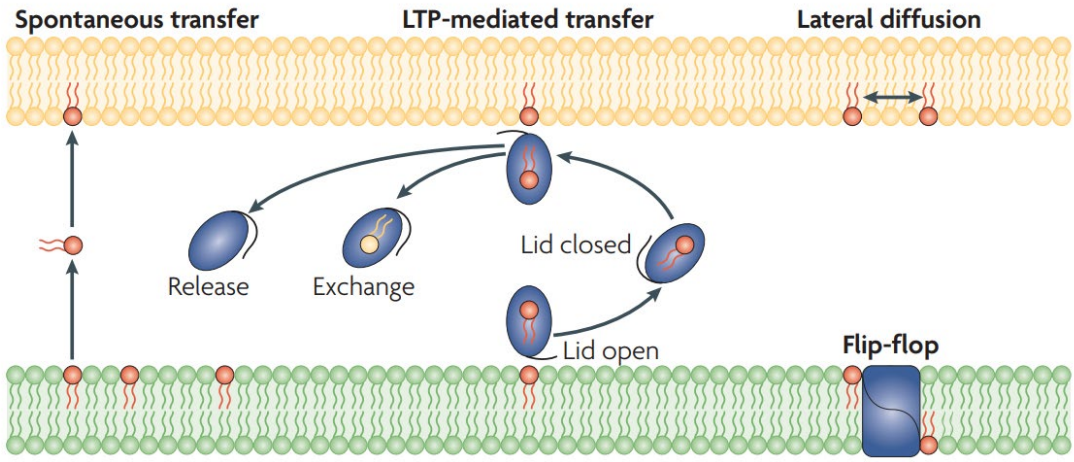

Figure 1.3. Mechanisms of non-vesicular lipid transport include monomeric lipid exchange, lateral diffusion, and transbilayer flip-flop. In monomeric lipid exchange, lipids are transferred between membranes either spontaneously or with the help of LTPs. LTPs can transfer a lipid to the acceptor membrane or exchange it with another lipid from the acceptor membrane. Lateral diffusion of lipids occurs within the same layer of the membrane. The transfer of lipids between the two opposite layers of the bilayer, also known as transbilayer flip-flops, can occur spontaneously or with the help of proteins such as flippases and translocases. Image reprinted, with permission, from Ref. *[19]* © (2010) Springer Nature.

Based on the monomeric lipid exchange mechanism described above, LTPs can remove lipids from a donor membrane, enclose them in their hydrophobic cavity, and then transfer them to the acceptor membrane by diffusing through the cytoplasm [9].

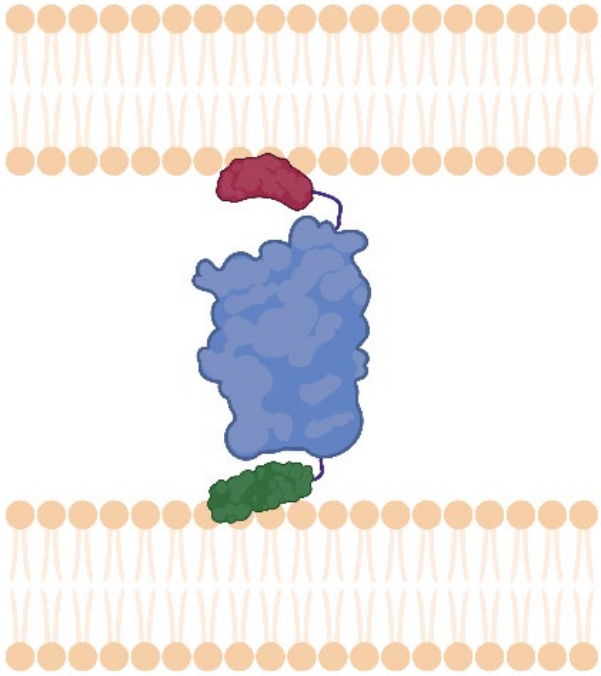

Figure 1.4. Proposed diagram showing how an LTP facilitates MCS formation. The red domain binds to the membrane at the top and the green domain binds to another membrane at the bottom. Created with BioRender.com.

According to another theory, LTPs operate at sites of close proximity between heterologous membranes called membrane contact sites (MCSs) and bind to both membranes simultaneously as shown in **Figure 1.4**. This allows them to move a lipid across different membranes [19, 22]. However, the exact mechanism by which LTPs bind to membrane and facilitate lipid transport at MCSs between organelles is not fully understood. Furthermore, it is unclear which other factors such as lipid

composition, lipid curvature, and lipid packing can affect the binding of LTPs to membrane.

1.5. LTPs

LTPs represent a subgroup of peripheral membrane proteins that bind to the membrane's surface. These proteins are characterized by having binding domains or areas that interact with membranes through a mix of non-specific and specific interactions [23]. LTPs form a vast and structurally varied class of proteins that include members from numerous protein (super)families, including StARkin, OSBP, bridge-like, prokaryotic, and tubular lipid-binding proteins, among others [24]. The oxysterol-binding proteins (OSBPs) play crucial roles in a variety of cellular functions, including signaling, vesicular trafficking, lipid metabolism, and the non-vesicular transfer of sterols. The oxysterol-binding protein (OSBP)-related proteins (ORPs) are a large family of mammalian LTPs that are conserved across species from yeast to humans [25]. Within the OSBP family, the most extensively studied are the mammalian ORP and the yeast oxysterol-binding homology (Osh) proteins [26]. Human ORP proteins have been conserved from yeast Osh proteins during evolution [27]. Humans possess 12 ORP genes, which through alternative splicing, give rise to 16 distinct protein variants [25]. In contrast, yeast cells, specifically *Saccharomyces cerevisiae*, have 7 ORP genes, known as Osh1 through Osh7, some of which are known by alternative names as well [28]. These were initially assumed to transport sterols and oxysterols [29-31], but they have recently been discovered to have a role in the transport of signaling lipids [32]. This discovery expands our understanding of the functional versatility and importance of these proteins within cellular processes.

1.5.1. ALPS

LTPs can have domains dedicated to sensing particular lipids or membrane characteristics. Lipid packing and curvature, for example, can serve as a signal to lipid transport proteins [33]. A good example of such lipid sensors is ArfGAP1, a Golgi-localized protein, which has an amphipathic lipid packing sensor (ALPS) motif that recognizes highly curved membranes through hydrophobic interactions [34]. Similar ALPS motifs have been found on other membrane-binding proteins [35]. ALPS motifs consist of 20-40 amino acids and, despite having different sequences, they exhibit similar physicochemical characteristics [33, 35]. ALPS motifs are a specific type of amphipathic helices characterized by a high abundance of serine and large hydrophobic residues (Phe, Leu, and Trp), as well as a low density of charged amino acids as shown in **Figure 1.5** [36, 37].

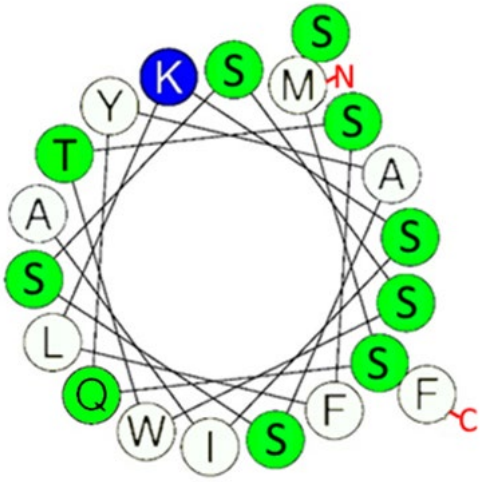

Figure 1.5. Helical wheel of Osh4's ALPS-like peptide. Hydrophobic residues are color-coded white, polar residues are color-coded green, and the charged residue (+) is highlighted in blue. The wheel was created with Heliquest (https://heliquest.ipmc.cnrs.fr/). (Data courtesy of Dr. Jeffery Klauda and Dr. Robert Allsopp).

ALPS motifs play a role in cellular stress response and are involved in membrane targeting for lipid trafficking [38]. These motifs prefer binding to membranes that have significant packing defects [38, 39].

1.5.2. Osh4

Among the seven Osh LTPs, Osh4 is the most abundantly expressed [40] and has been selected for the studies in this dissertation. It consists solely of the OSBP-related domains (ORDs) domain and is the best-studied example of LTP up to date due to its structural simplicity [41]. Osh4 is a 51 kDa protein responsible for transporting sterols, including cholesterol and ergosterol [30]. According to the crystal structure of Osh4, it has a β-barrel shape that consists of 19 antiparallel β-sheet strands (**Figure 1.6**). This structure creates a hydrophobic core that makes it easier for Osh4 to capture sterols. Additionally, Osh4 has an α-helix that is an amphipathic lipid packing sensor (ALPS) motif located at the protein's mouth, which acts as a barrier between the sterol and the exterior environment [42]. The Osh4 protein also possesses an ALPS-like motif, composed of 20 amino acids [23]. This sequence is located at the N-terminus of the Osh4 protein, representing one of its main membrane binding regions [40].

In addition to the ALPS motif, Osh4 has another membrane-binding motif formed by the α6/α7 helices. Osh4's α6/α7 domain attaches to membranes by utilizing three residues: R314, K325, and K336, and this leads to strong membrane binding and the insertion of multiple hydrophobic residues beneath the lipid head group [34].

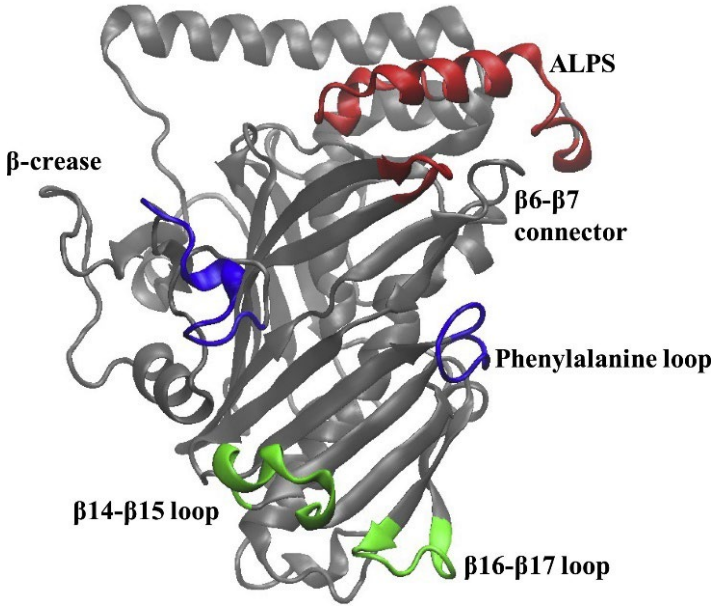

Figure 1.6. Structure of the Osh4 protein, where the domains responsible for targeting the membrane are highlighted in color. Image reprinted, with permission, from Ref. *[9]* © (2022) Elsevier.

The biologic function of Osh4 is not completely understood. Through *in vitro* assays, Raychaudhuri et al. [30] found that Osh4 plays a key role in the transfer of cholesterol and ergosterol between membranes, and the transfer of sterols is faster between membranes that contain phosphoinositide (PIP) lipids (anionic), indicating that PIPs regulate the process. This was confirmed by observing a significant decrease in PM to ER sterol transport in the yeast cells with conditional defects in PIP biosynthesis. Additionally, de Saint-Jean et al. suggested that Osh4 shuttles sterol from the ER to late compartments marked by PI 4-phosphate (PI(4)P) lipids and reciprocally transports PI(4)P back [43]. Schulz et al. [44] conducted experiments that revealed the ability of Osh4 to make contact with two opposing membranes simultaneously. Recently, through molecular dynamics simulations, Karmakar and Klauda [8] discovered that the stable binding of the phenylalanine loop of Osh4 allows other

regions, like the ALPS motif, β6-β7 connector, β14-β15 loop, β16-β17 loop, and β-crease (**Figure 1.6**), to have increased contact with the membrane. This finding is different from the previous work, which suggested that Osh4-model membrane contact was stabilized by salt bridges alone [45] .

The specific biological purpose of Osh4 within the cell remains uncertain. It is unclear whether it operates as a carrier of sterols, a controller of MCS formation, or a lipid sensor that influences lipid metabolism, signaling, and the cellular membrane's composition. In addition to elucidating the lipid binding mechanism of LTPs such as Osh4, this study has the potential to impact the understanding of human diseases caused by a mutation in LTPs, such as Niemann-Pick type C, Cohen syndrome, and early-onset Parkinson's disease [18].

1.6. Experimental biophysical methods for lipid-protein interactions

Studying lipid-protein interactions requires using methods that help gain information about protein structure and the molecular-level interactions of proteins and lipids. Various experimental methods provide biophysical data that reveals information about the lipid-protein interactions.

1.6.1. CD

Circular dichroism (CD) spectroscopy is a technique commonly used for analyzing biomolecules, and it can be used to provide information on the interaction of proteins and lipids. When a chiral molecule absorbs left- and right-circularly polarized light differently, it results in a CD spectrum [46]. This spectrum is related to the properties

of the biomolecules, such as their secondary structure. As a result, it is possible to determine the folding and conformational changes of biomolecules from their CD spectra [47].

One of the primary applications of CD spectroscopy is the determination of the secondary structure composition of proteins. The CD spectral features of various secondary structure elements, such as α-helices, β-sheets, turns, and random coils, are well established as shown in **Figure 1.7** [48]. By analyzing the shape and intensity of these features, the relative proportions of different secondary structure components can be estimated in a sample.

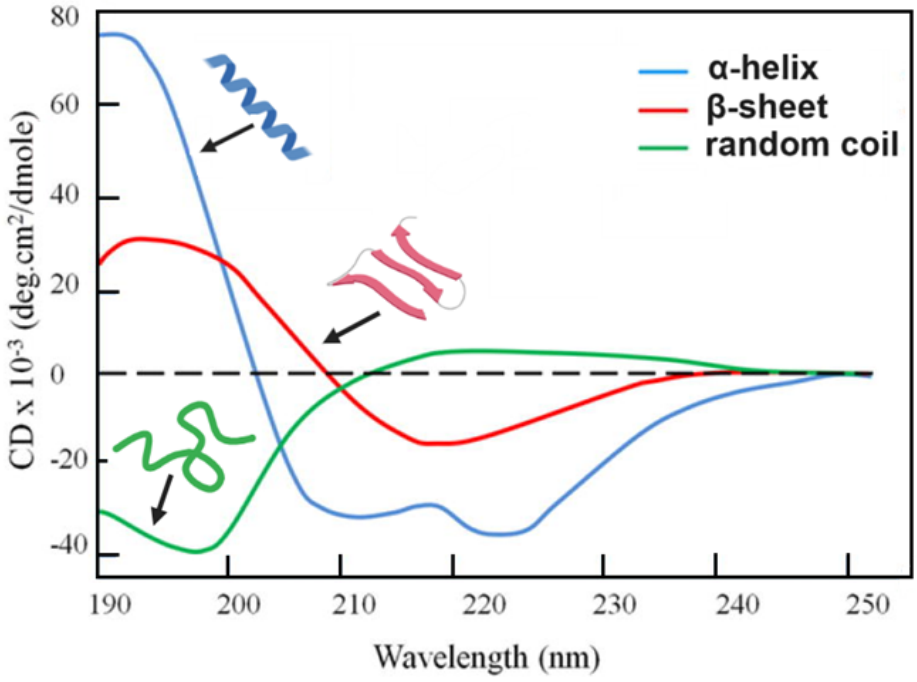

Figure 1.7. Standard CD spectra redrawn by *[49]* from *[50]*. Image reprinted, with permission and some modifications, from Ref. *[49]* © (2014) Elsevier. Secondary structures were created with BioRender.com.

CD studies can be valuable for investigating conformational changes induced by protein-lipid binding [51]. Binding events often lead to shifts or alterations in the CD spectrum, reflecting changes in the secondary structure or conformation of the protein upon interaction with its lipid.

In addition to soluble proteins, CD spectroscopy is also widely applied in the study of membrane proteins [52] and peripheral proteins [53]. By analyzing the CD spectra of membrane proteins in various membrane mimetic environments, such as detergents, lipids, or lipid bilayers, information on their secondary structure and conformation within a membrane-like context can be obtained [54] . For example, Davidson et al. noticed similarities in the sequences of the unstructured α-synuclein signaling peptide and the amphipathic α-helical domains of the exchangeable apolipoproteins, and wanted to determine if binding to lipids would bring structure to the membrane. Using CD, they showed that α-synuclein binds to small unilamellar phospholipid vesicles containing anionic phospholipids, but not to vesicles with a net neutral charge. That α-helicity increased from 3% to approximately 80% [55].

1.6.2. Tryptophan fluorescence

Tryptophan fluorescence can be employed to determine whether peptides or short binding domains of proteins containing the tryptophan amino acid interact with lipids. The unique ring structures found in the functional groups of tryptophan, phenylalanine, and tyrosine contribute to their distinct fluorescence properties. These amino acids' fluorescence is highly responsive to the local environment's polarity.

Due to its high quantum yield, tryptophan is recognized as the primary intrinsic fluorophore in peptides and proteins [56].

This technique is particularly useful for studying lipid-peptide interactions as it allows researchers to leverage the fluorescent properties of tryptophan [57]. By exploiting the fluorescence emission of tryptophan, the behavior of peptides within lipid environments can be investigated, revealing insight on the peptide-lipid binding dynamics. Tryptophan fluorescence is highly responsive to the local surroundings, as changes in the intrinsic tryptophan fluorescence of proteins often arise due to conformational modifications or interactions with lipids. Generally, tryptophan fluorescence intensity increases when exposed to a hydrophobic environment, while it decreases in an aqueous medium [56, 58]. This change in quantum yield is often accompanied by a blue shift of the emitted light (shorter wavelength), as shown in **Figure 1.8.** [57-59]. The depth of insertion into the lipid bilayer can be associated with the degree of blue shift [60].

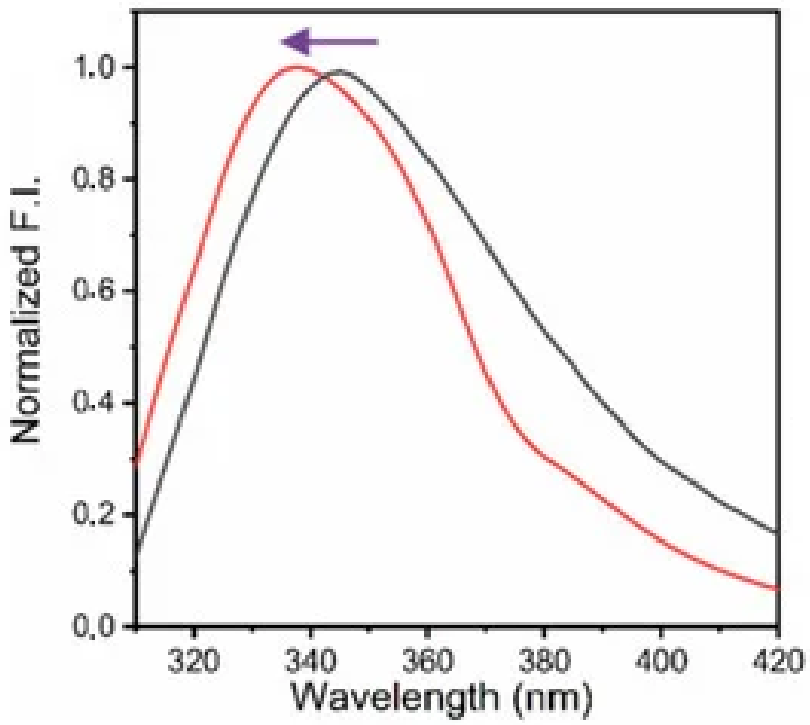

Figure 1.8. Tryptophan fluorescence spectra of a protein before (black line) and after (red line). Image reprinted from Ref *[61]*. MDPI does not require any special permission to reprint images.

The popularity of fluorescence is due to the availability and ease of basic data acquisition and analysis, especially when compared to other spectroscopic techniques. Despite its simplicity, it does not seem to compromise its primary benefits, one of which is exceptional sensitivity [62]. For example, Killian et al. mutated Val to Trp in the signaling peptide sequence of the *E. coli* outer membrane protein PhoE. This mutation was used to probe the interaction using tryptophan fluorescence spectroscopy. They found that a larger blue shift occurred in the presence of phosphatidylglycerol (PG) or cardiolipin (CL) than with phosphatidylcholine (PC). They further found fluorescence quenching was prevented upon binding to the anionic membranes [63].

1.6.3. Isothermal titration calorimetry

Isothermal titration calorimetry (ITC) is an analytical method utilized to investigate interactions between molecules, including protein and lipids. It evaluates the heat changes associated with binding events, offering valuable insights into thermodynamic parameters like equilibrium association constant (K_a), stoichiometry (N), enthalpy change (ΔH), and entropy change (ΔS) [64, 65].

One of the significant advantages of ITC over other techniques is that it can explore interactions in a native-like environment [66], such as physiological conditions, without the need for labeling or immobilization [67]. Moreover, it can furnish valuable information regarding the nature of the binding interaction, such as whether it is enthalpically or entropically driven.

To perform an ITC experiment, one reactant (ligand; lipids in the case of lipid-protein interactions) is gradually introduced into a solution containing the other reactant (macromolecule; protein in the case of lipid-protein interactions), while maintaining a constant temperature. In the ITC microcalorimeter, there are two cells, one of which contains water and serves as a reference cell. The other cell contains the sample and is used for titration of a binding partner using an injection syringe [65]. During an experiment, the temperature of both the reference cell and sample cell are set to the desired level. A syringe containing the lipid is inserted into the cell containing the protein of interest. The lipid is injected into the protein solution in small amounts, and any heat changes associated with the binding of the lipid to the protein are detected and measured with remarkable accuracy. The microcalorimeter continues measuring all heat released until the binding reaction reaches equilibrium after the first injection.

This measured heat is directly proportional to the amount of binding that has taken place [68]. If the reaction is exothermic in nature, the sample cell will become warmer than the reference cell, causing a downward peak in the signal. For endothermic reactions, upward peaks are observed [69]. As the temperature of the two cells returns to equilibrium, the signal returns to its starting position. The microcalorimeter compensates for the small heat changes detected as the second small aliquot of the lipid is injected into the sample cell.

The molar ratio of the lipid to the protein is gradually increased through the series of lipid injections. As the protein becomes more saturated with lipid, less binding occurs, and the heat change decreases until the sample cell contains an excess of lipid relative to protein, indicating saturation [70]. The area of each injection peak is then integrated and plotted against the molar ratio of lipid to protein, resulting in an isotherm that can be fitted to a binding model, from which the binding affinity is estimated (**Figure 1.9)**. The molar ratio at the center of the binding isotherm is used to determine the reaction stoichiometry [71].

From the binding isotherm, the binding enthalpy (ΔH) is estimated as the difference between the initial H value and the plateau H value. The slope of the line that intercepts the exponential phase of the isothermal curve corresponds to K_a, the association equilibrium constant [72].

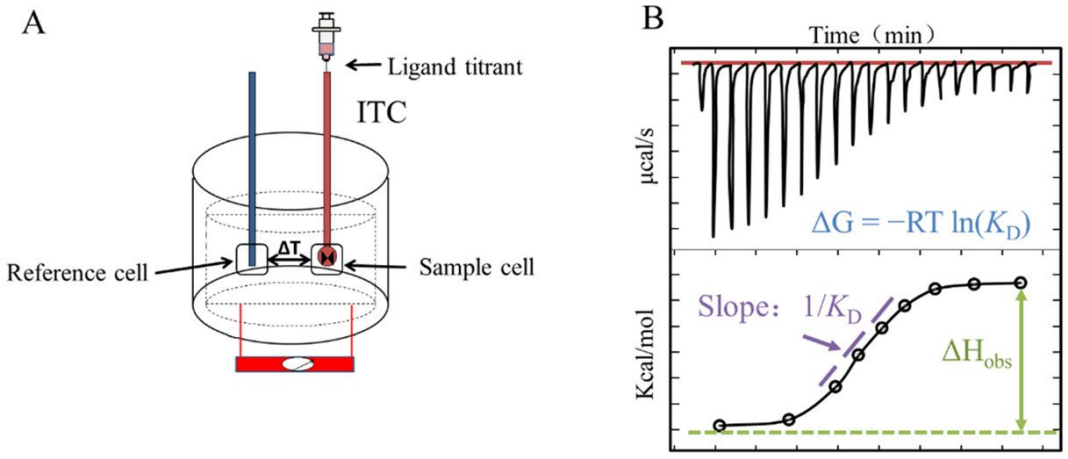

Figure 1.9. The fundamental concept of isothermal titration calorimetry: A) schematic diagram of ITC instrument where lipid in the syringe is titrated into the sample cell, B) typical ITC thermogram where the top plot is a raw data plot of heat flow over time and the bottom plot is integrated heats upon injection (black circles) and the data fit of the raw data (black line). Image reprinted, with permission and some modification, from Ref *[73]* © (2022) American Chemical Society.

The dissociation equilibrium constant (K_d), which is commonly used to describe the affinity of biomolecules, can be manually calculated by using the following equation:

$$K_d = 1/K_a \tag{1.1}$$

The binding entropy (ΔS) is indirectly calculated from

$$\Delta S = (\Delta H - \Delta G)/T \tag{1.2}$$

The Gibbs free energy (ΔG) can be indirectly calculated by using the following equation:

$$\Delta G = -RT \ln K_a \tag{1.3}$$

where R is the universal gas constant (8.31 J K^{-1} mol^{-1}), T is the temperature (K), and K_a is the association constant.

ITC enables us to quantify the strength and specificity of lipid-protein interactions without the need for labeling. By measuring the thermodynamic properties of the interactions between protein and various lipid compositions, we can determine which type of lipid the protein prefers to bind.

1.6.4. X-ray diffraction

The changes in the lipid multilayer structure caused by interaction with peptides can be measured by X-ray diffraction. X-rays have a shorter wavelength compared to visible light. This property makes them suitable for diffraction studies, as the X-ray wavelength is comparable to the unit-cell spacing in crystals [74]. The process of X-ray diffraction involves directing an X-ray beam toward a sample that is positioned at the center of the instrument as shown in **Figure 1.10**. The intensity of the scattered X-rays is then measured as a function of outgoing direction [75].

The equation developed by William H. Bragg and William L. Bragg and also known as Bragg's Law plays a critical role in understanding X-ray diffraction [76]:

$$n\lambda = 2dsin\theta \tag{1.3}$$

where λ is the wavelength of the X-ray beam, n is an integer representing the order of the diffraction peak, d is the interplanar spacing between rows of lattice planes (i.e., atoms, ions, molecules), and θ is the scattering angle of the X-ray beam with respect to these planes [77]. Bragg's equation ensures that X-ray beams scattered by atoms in a periodic structure are in phase, allowing X-ray diffraction only in the θ direction [77].

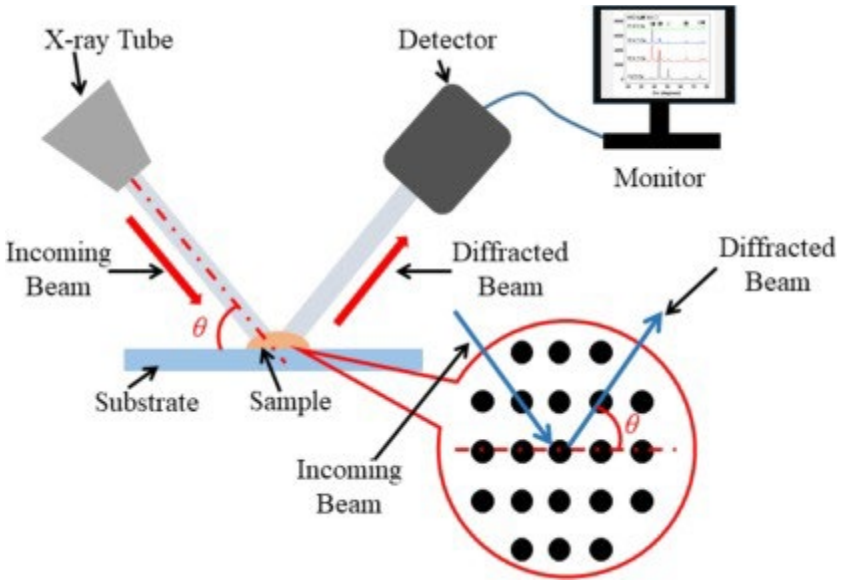

Figure 1.10. Illustration of the conditions necessary for X-ray reflection according to Bragg's law. Image reprinted, with permission, from Ref *[78]* © (2023) Elsevier.

Liquid crystallography is an X-ray diffraction technique that was developed by Wiener & White back in 1991 [79, 80]. It is widely used to determine the structure of liquid crystalline lipid multilayers and is particularly useful in analyzing the complete one-dimensional structures of fluid multilayers that exhibit liquid-crystalline properties. To carry out this method, dry lipid membranes are first hydrated from the vapor phase of a saturated salt solution. The resulting electron density profile of the multilayer provides valuable insights into the structure and behavior of the multilayer, and can even reveal the impact of the addition of peptides or proteins on its electron density profile.

The field of liquid crystallography has been instrumental in investigating the structural perturbations in the lipid multilayers caused by various peptides [81-84]. Upon addition of these peptides to the multilayer, thinning of the lipid multilayer can

be observed, which is often associated with the effect of membrane-active peptides. This thinning is evident through a measurable reduction in the repeat distance (*d*) in the multilayered samples. Thinning of the lipid multilayer could signify the perturbation resulting from the peptide's integration into the multilayer, underscoring the importance of X-ray diffraction studies for investigating peptide-lipid interactions.

1.7. Overview of dissertation

In my dissertation, I characterize the binding of the Osh4 protein to a model membrane and address the questions raised earlier. **Chapter 2** presents my studies on the ALPS-like peptide and the biophysical characterization of the peptide with membranes. In **Chapter 3**, I describe the expression and purification of the Osh4 protein and compare the different fusion tags for expression and purification. **Chapter 4** includes discussions, conclusions, and future research directions on Osh4 and Osh family proteins.

2. Chapter 2: ALPS-like peptide of the Osh4 protein

2.1. Introduction

The Osh4 protein has a 20 amino acid, amphipathic lipid-packing sensor (ALPS)-like motif at its N-terminus. This motif is α-helical in nature (**Figure 2.1**). Due to its amphipathic structure, ALPS has a preference for membranes with a strong positive curvature and a low lipid packing density [45]. Drin et al. [33] found that the binding of the ALPS-like peptide of the Osh4 protein was enhanced by less lipid packing. They also showed that removing the ALPS motif resulted in the loss of the Osh4 protein's natural ability to detect lipid-packing. Other studies have shown that the ALPS motif has a slightly stronger affinity for membranes that have a higher anionic character, such as TGN systems (42.7% anionic character) and ER membranes (37% anionic character) [33]. However, the exact process by which lipid-packing is detected is still unknown.

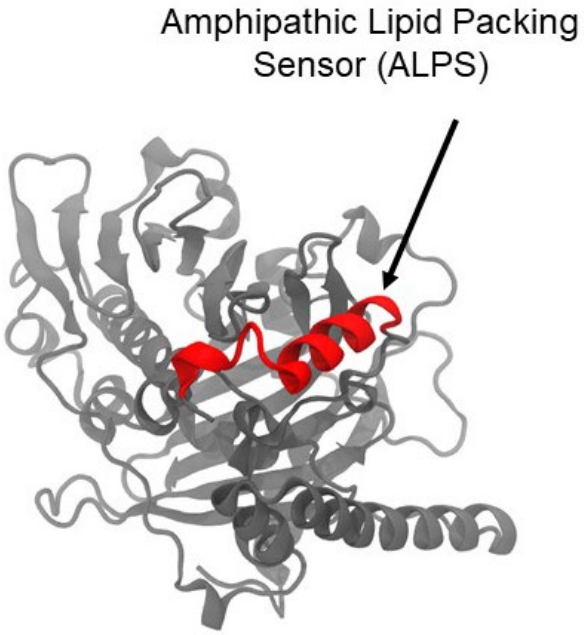

Figure 2.1. Domain structure of Osh4 with ALPS highlighted in red. (Figure courtesy of Dr. Jeffery Klauda and Dr. Robert Allsopp).

Due to the abundance of uncharged polar residues, such as serine, threonine, and glycine, on the polar face of the peptide, the ALPS-like peptide exhibits a reduced sensitivity to the typical electrostatic interactions that occur between the predominantly cationic peripheral proteins and the anionic membrane surface [33]. This raises an intriguing question about the necessity of anionic lipids, such as 1-palmitoyl-2-oleoyl-sn-glycero-3-phospho-L-serine (POPS) and 1-palmitoyl-2-oleoyl-sn-glycero-3-phosphate (POPA), for ALPS binding, in addition to zwitterionic phospholipids like 1-palmitoyl-2-oleoyl-glycero-3-phosphocholine (POPC), which were chosen for this study. POPC, known for its zwitterionic headgroup and hydrophobic tail, is a predominant component of cell membranes (**Figure 2.2**).

Conversely, POPS, characterized by its anionic headgroup and comparable hydrophobic tail, is vital in cellular signaling and membrane dynamics.

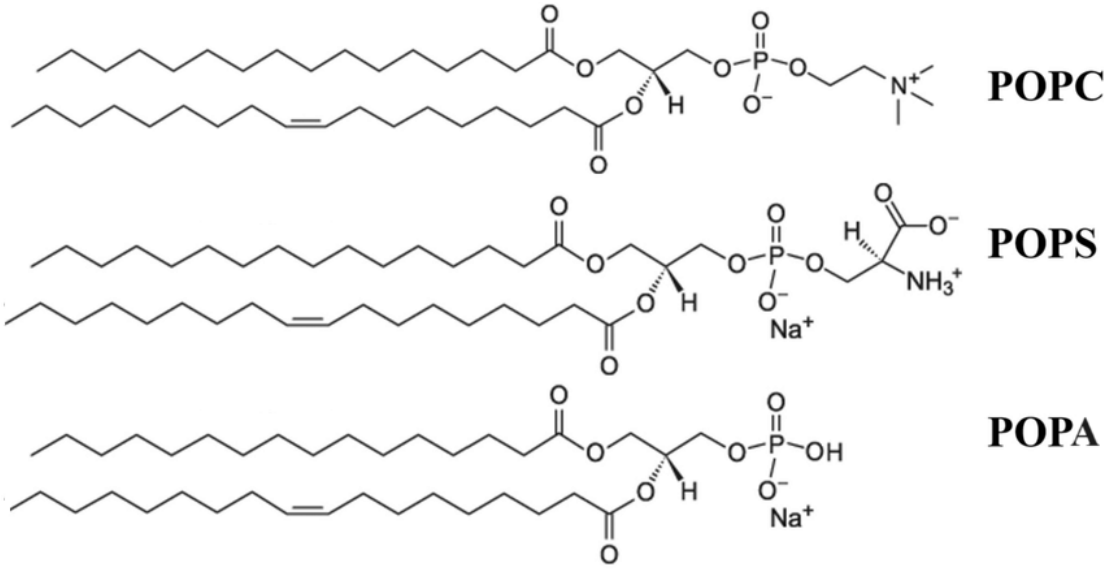

Figure 2.2. Structure of POPC and POPS lipids. Image reprinted, with permission, from Ref. [85] © (2022) Springer Nature. Some modifications were applied.

There are already some publications detailing the binding processes of short amphipathic peptides and even computational kinetic studies of the binding process [23, 86, 87]. However, there is a notable absence of experimental studies on the ALPS-like motif of Osh4.

Here, we use experimental methods to characterize the binding of the ALPS peptide to phospholipid membranes. To probe how the secondary structure of the ALPS peptide changes due to its environment, circular dichroism (CD) measurements were performed. To determine how the ALPS peptide binding impacts the structure of model membranes, measurements were performed using X-ray diffraction. Binding thermodynamics are essential to probe how lipid composition can influence ALPS

peptide binding. For this work, we used ITC to obtain peptide binding free energies and compared this with Trp fluorescence work with a binding isotherm model to derive dissociation constant K_d.

2.2. Methods

2.2.1. Peptide synthesis and preparation

The ALPS peptide (MSQYASSSSWTSFLKSIASF-NH_2) was commercially synthesized with HCl salt (Biosynth) and a purity of >95%. Before use, the ALPS peptide was dissolved in ultrapure water and further dialyzed against water or buffer, as appropriate for the experiment, overnight to remove HCl salt.

2.2.2. Liposome preparation

Large unilamellar vesicles (LUVs) were used to study the binding interaction of ALPS with model membranes. The lipids POPC, POPS, and POPA were obtained from Avanti Polar Lipids, Inc. (USA) in chloroform. Prior to use, chloroform from pure POPC and a mixture of POPC and POPS was removed under a stream of dry nitrogen. The lipids were further dried under a vacuum overnight and then hydrated in water above the transition temperature for 30 min. The suspension was extruded using Avanti's mini-extruder through filters with a 0.1 μm pore size to form LUVs. The particle sizes of the resulting liposomes were characterized using the multi-angle light scattering mode of a Zetasizer Ultra (Malvern Panalytical). The LUVs were 110-140 nm in diameter.

2.2.3. Circular dichroism

Circular dichroism (CD) spectroscopy experiments were performed to assess the conformation of the ALPS peptide. ALPS samples at a final concentration of 45 μM were prepared in water in the absence and in the presence of POPC and POPC/POPS LUVs at a total lipid concentration of 1.125 mM at a peptide-to-lipid molar ratio of 1:25 or in pure tetrafluoroethylene (TFE). A Jasco J-1500 CD Spectrophotometer (Jasco Analytical Instruments, Tokyo, Japan) was used to perform the measurements. Spectra were acquired at 298 K in the wavelength range of 190 to 300 nm, with 0.5 nm step resolution, a sweep speed of 50 nm/min, a response time of 2 s, and a bandwidth of 1 nm, using a 0.1 cm path length quartz cuvette. The spectra were processed with Jasco software to subtract the solvent spectra. The peptide's secondary structure content was calculated from the CD spectra using Jasco Secondary Structure Estimation (SSE) estimation tool. Each experiment was reported as an average of 3 scans.

2.2.4. X-ray diffraction

We performed x-ray diffraction to understand how the ALPS peptide interacts with highly oriented phospholipid multilayers. Highly oriented multilayers were prepared by application of 2 mg of lipid dissolved in water mixed with ALPS solution or water (for blanks) to glass coverslips. The samples were equilibrated for at least 4 h before the measurements and maintained at 97% relative humidity using a saturated solution of potassium nitrate (KNO_3) and a temperature of 298 K during the measurement. The x-ray beam was directed toward a sample, and the diffraction intensity was continuously recorded as a function of the outgoing direction. The diffraction data

were collected in a θ-2θ (specular) mode. Diffracted intensity for each Bragg order was calculated by integrating the counts below the peaks. The structure factors, denoted as *f(h)*, were determined by calculating the square root of the peak integrals. The scattering-length density *ρ(z)* along the bilayer normal direction *z* was calculated from the equation provided by King et al. [88] and Jacobs and White [89]

$$\rho(z) = \frac{2}{d}\sum_{h=1}^{M} f(h)cos\left(\frac{2\pi hz}{d}\right) \quad (2.1)$$

where the *f(h)* is the measured structure factor for the *h*th order peak, *d* is the Bragg spacing, and *M* is the highest observed diffraction order. Both POPC and POPC-POPS were tested at a peptide to lipid molar ratio of 1:25.

2.2.5. Fluorescence spectroscopy

We used fluorescence spectroscopy to examine the Trp fluorescence emission spectrum of ALPS in the presence of LUVs. The ALPS peptide was prepared as a 40 μM stock solution, dissolving it either in water or in a buffer solution of 50 mM KCl at pH 7.0, which also included 9.3 mM K_2HPO_4 and 0.7 mM KH_2PO_4. The LUVs were prepared using the same buffer as the peptide. Titrations were conducted by measuring the emission spectra of the ALPS peptide solution at a consistent concentration of 20 μM. The lipid concentrations ranged from 0 to 4 mM, with measurements taken at 2-fold dilutions. Using Jasco spectrofluorometer FP-8300, we recorded emission spectra ranging from 300 to 500 nm at an excitation wavelength of 280 nm (with a 10 nm excitation (Ex) bandwidth and a 5 nm emission (Em) bandwidth). To reduce fluorescence scattering background, polarizers were set at Ex_{pol} = 90° and Em_{pol} = 0°. We calculated corrected fluorescence intensities of the

ALPS peptide $F_{peptide}^{corrcted}([L])$ at lipid concentration *[L]* using the Trp zwitterion fluorescence as a reference to account for the decrease in the intensity at high lipid concentration associated with the losses arising from the scattering of both exciting and fluorescence light [59]. The following equation was used:

$$F_{peptide}^{corrcted}([L]) = F_{peptide}([L])\frac{F_{Trp}^{buffer}}{F_{Trp}([L])} \tag{2.2}$$

where $F_{peptide}$ is the raw uncorrected fluorescence intensity of the ALPS peptide at lipid concentration *[L]*; F_{Trp}^{buffer} is the fluorescence intensity of pure Trp at the same concentration as the ALPS peptide in the absence of LUVs; $F_{Trp}([L])$ is the fluorescence intensity of pure Trp, matched with the concentration of the ALPS peptide in the presence of LUVs at lipid concentration *[L]*.

Fluorescence data was used to predict the dissociation constant K_d using the equation from Tatulian [90]:

$$\frac{\Delta F}{\Delta F_{max}} = \frac{1}{2}\left(1 + \frac{\delta[L]}{N[P]} + \frac{K_d}{[P]}\right) - \sqrt{\frac{1}{4}\left(1 + \frac{\delta[L]}{N[P]} + \frac{K_d}{[P]}\right)^2 - \frac{\delta[L]}{N[P]}} \tag{2.3}$$

where ΔF is fluorescence intensity of the peptide-vesicle mixture minus the fluorescence intensity of the pure peptide; ΔF_{max} is the saturating value of ΔF at high lipid concentration; *[L]* is the lipid concentration; δ is the fraction of the lipid in the external leaflet of the vesicles (δ = 0.52 for 100 nm vesicles); N is the number of binding sites of the protein; [P] is the total protein concentration. For the fitting experiment, two sets of data were collected. Theoretical binding curves ($\Delta F / \Delta F_{max}$ vs. *[L]*) were constructed using **Equation 2.3**, and the best fit values of K_d and N

were determined by minimizing the sum of squares error for each set of data. The standard error of the mean (n=2) for K_d (and consequently ΔG) and N, derived from the fitting of each set of data, was calculated.

2.2.6. Isothermal titration calorimetry

To understand the thermodynamics of the binding of the ALPS peptide to liposomes, ITC was utilized. The ALPS peptide was prepared as a 100-150 μM stock solution by dissolving it in a buffer solution containing 50 mM KCl, 9.3 mM K_2HPO_4, and 0.7 mM KH_2PO_4 (pH=7). Similarly, LUVs were prepared at a lipid concentration of 2 mM in the same buffer as the peptides. The LUVs were then dialyzed in the same buffer to minimize the heat of dilution. We injected 10-15 μL of the ALPS peptide into the reaction cell containing the LUVs with 200−300 s time intervals. The reference power was set to 15 μcal/s, using a syringe stirring speed of 300 rpm. Titrations were carried out on a VP-ITC microcalorimeter (MicroCal, Inc) at 298 K. For each experimental setup, the dilution heat was subtracted from the reaction heat obtained in the peptide-to-lipid binding experiments. The total lipid concentration was used in the estimation of the thermodynamic binding parameters. The experimental data were fit to a one-site model [91]:

$$Q(i) = \frac{nP_t\Delta HV}{2}\left(1 + \frac{L_t}{nP_t} + \frac{1}{nKP_t} - \sqrt{\left(1 + \frac{L_t}{nP_t} + \frac{1}{nKP_t}\right)^2 - \frac{4L_t}{nP_t}}\right) \quad (2.4)$$

where $Q(i)$ the total heat released or absorbed (kcal/mol) for the ith injection, n is the number of binding sites, P_t is the total peptide concentration (mM), L_t is the total lipid concentration, V is the cell volume (1.32 mL), K_a is the association constant (mM^{-1}), and ΔH is the binding enthalpy change.

The heat for the ith injection, $\Delta Q(i)$, is calculated by subtracting $Q(i-1)$ from $Q(i)$ and using the equation that includes the correction factor for the displaced volume (i.e., the injection volume dV_i).

$$\Delta Q(i) = Q(i) + \frac{dV_i}{V}\left[\frac{Q(i) + Q(i-1)}{2}\right] - Q(i-1) \qquad (2.5)$$

The ITC instrument measures $\Delta Q(i)$ for each injection and fits these values to an equation using Origin® [MicroCal™]. The fitting process involves an initial guess of n, K_a, and ΔH, which are improved by comparing calculated and experimental values. This process is repeated until no further significant improvement is achieved.

2.3. Result and discussion

2.3.1. ALPS peptide structure

Based on the crystal structure reported by Im et al. [42], the ALPS peptide features a primary helix with distinct polar and nonpolar surfaces. To delve deeper into the conformational behavior of the ALPS peptide, particularly during its interaction with membranes, we employed CD spectroscopy. According to our CD results, when the ALPS peptide is in water, it showed a largely unstructured nature, as reflected by the negative band appearing near 220 nm (**Figure 2.3**). The JASCO multivariate Secondary Structure Estimation (SSE) software showed that the majority of the ALPS peptide structure was identified as unstructured; however, there were traces of α-helix and β-sheet structures, which are signals of the peptide's complex structure (**Table 2.1**).

Further investigation was conducted using 100% trifluoroethanol (TFE) to mimic the hydrophobic core of the phospholipid bilayer. In the hydrophobic solvent, the ALPS peptide displayed a double-minimum peak around 205 and 222 nm (**Figure 2.3**), which are characteristics of an α-helical structure, and according to the SSE analysis, the peptide had a helical content of 51.6% (**Table 2.1**). The formation of the amphipathic helical ALPS peptide may allow the peptide residues to assemble to better protect hydrophilic residues from the hydrophobic environment.

When we introduced the peptide to POPC vesicles in water, a notable change was observed in its secondary structure compared to water: the helical content shifted from 18.4% to 28.5% (**Table 2.1**) These results suggest that the peptide is more structured in the presence of POPC vesicles than it is in pure water. We also investigated the structure of the ALPS peptide in the presence of vesicles formed from the negatively charged phospholipid POPS. Upon incorporating negatively charged POPS into the zwitterionic POPC vesicles, we observed significant changes in the CD spectrum of the peptide. The peptide underwent notable conformational changes, showing the double minima (at 210 and 222 nm). The α-helical conformation was more prominent in the presence of 1:1 POPC-POPS (87.8%), 4:1 POPC-POPS (79.3%), and 9:1 POPC-POPS (49.0%) liposomes than in liposomes solely consisting of POPC (28.5%). This suggests that the presence of anionic lipids plays a crucial role in the folding of the ALPS peptide at the membrane/water surface.

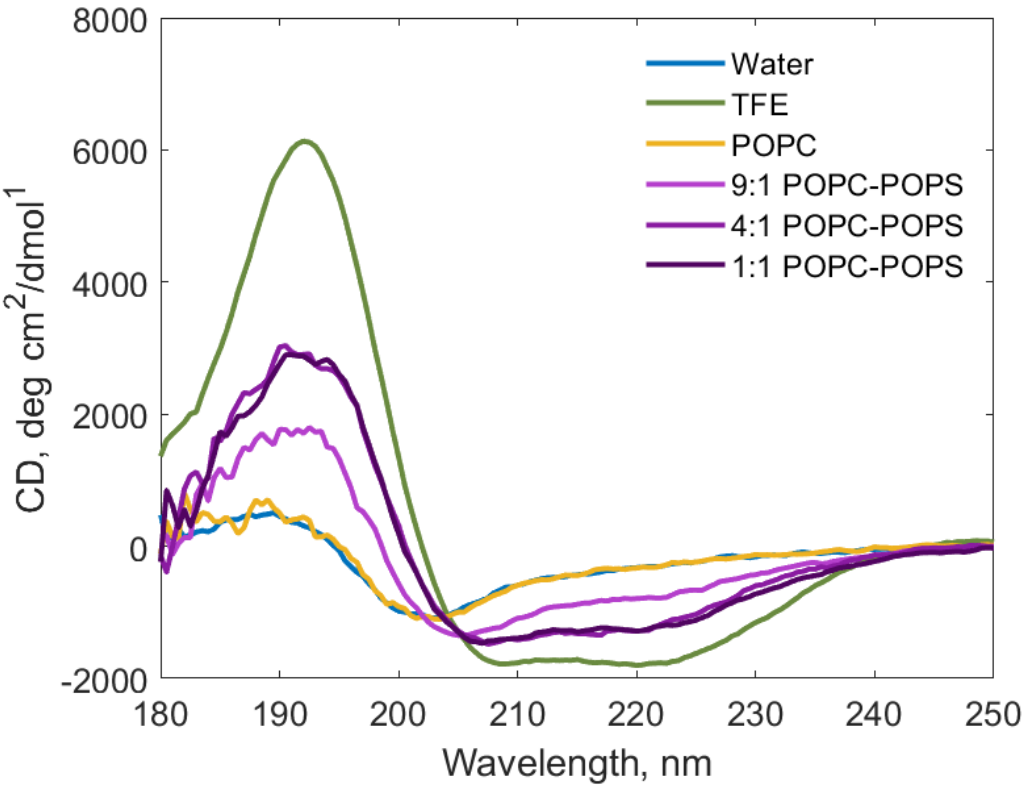

Figure 2.3. CD spectra of 45 μM ALPS peptide in the form of mean residue ellipticity measured in water, TFE (and in the presence of large uniamellar vesicles (LUVs) composed of POPC and POPC-POPS lipids. The final concentration of lipids was 1.125 mM in water. The temperature was maintained at 298 K. Each experiment was reported as an average of 3 scans.

Table 2.1. Percentages of secondary structure elements of ALPS in different environments.

Solvents and Liposomes [a]	Secondary structure composition [b]			
	α-helix	**β -sheet**	**turn**	**random**
Water	18.4%	24.0%	17.9%	39.7%
TFE	51.6%	40.8%	7.6%	0.0%
POPC	28.5%	19.5%	15.9%	36.1%
9:1 POPC-POPS	49.0%	5.9%	15.6%	29.5%
4:1 POPC-POPS	79.3%	14.4%	6.3%	0.0%
1:1 POPC-POPS	87.8%	0.0%	9.4%	2.8%

[a] Liposomes had a peptide-to-lipid molar ratio of 1:25 molar ratio.
[b] Secondary structure elements were obtained from the deconvolution of CD spectra of ALPS peptide in the absence and in the presence of the reported vesicles.

2.3.2. ALPS membrane interaction

Our next focus was on how ALPS interacts with model membranes, and we used Trp fluorescence as a probe to start this investigation. The changes in the fluorescence emission of the single Trp residue in Osh4 protein's ALPS-like peptide allows monitoring of the interaction of the peptide with liposomes by observing a blue shift of the fluorescence emission maximum of Trp in a hydrophobic environment [58]. In fluorescence spectroscopy, a blue shift refers to a shift in the emission spectrum toward shorter wavelengths, resulting in higher energy emissions, and this shift causes the light to move toward the blue end of the spectrum [92].

The ALPS peptide in water has a fluorescence emission maximum of 352 nm (**Figure 2.4**), typical for Trp in a polar environment [93]. Upon the addition of POPC

liposomes at a concentration of 1-4 mM, a blue shift of the fluorescence emission maximum of Trp was observed (**Figure 2.4**). These spectra suggest that the Trp residue of the ALPS peptide penetrates the hydrocarbon region of the bilayer. Interestingly, when vesicles contained both POPC and POPS lipids, the blue shift was more noticeable. Additionally, there was a more substantial increase in fluorescence intensity compared to vesicles composed solely of POPC lipids. (**Table 2.2**). The emission intensity of Trp exhibited a blue shift that increased with a higher percentage of POPS in the lipid composition of the liposomes. For instance, in liposomes with a 1:1 POPC-POPS lipid composition, the blue shift was more pronounced than in those with a 9:1 POPC-POPS ratio. This could indicate that the ALPS peptide has better interaction with anionic POPS lipids than with zwitterionic POPC lipids, which can be explained by the presence of the positively charged Lys residue in the sequence of the ALPS peptide.

The emission intensity for the POPC-POPC lipid mixture is expected to increase with rising lipid concentration, as observed for pure POPC lipids (**Figure 2.4**). However, the decrease in intensity at higher lipid concentrations is likely due to scattering artifacts, as described by Ladokin [59, 62].

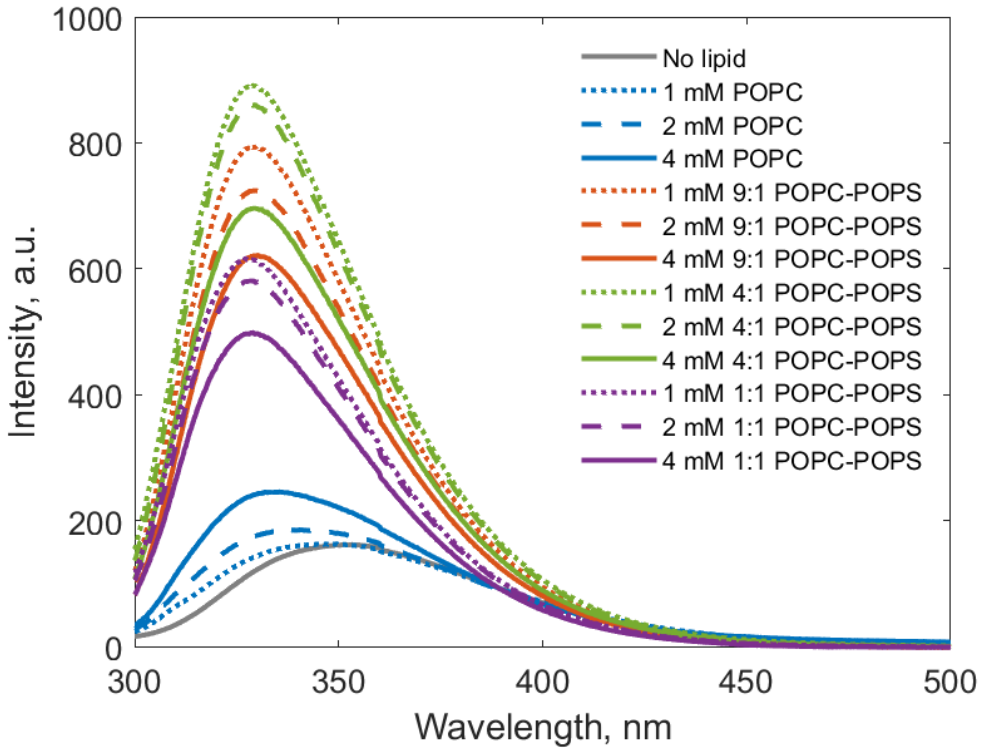

Figure 2.4. Fluorescence of Trp of ALPS peptide (20 μM) alone and in the presence of POPC liposomes and POPC-POPS liposomes. Liposomes were prepared at three molar ratios of POPC to POPS lipids with total lipid concentrations of 1-4 mM.

Table 2.2. Blue shift of Trp fluorescence in ALPS due to interaction with liposomes of varying composition and concentration.

	Blue Shift, nm		
Liposomes	1 mM	2 mM	4 mM
POPC	4.60 ± 0.26	10.64 ± 0.22	16.59 ± 0.51
9:1 POPC-POPS	22.04 ± 0.12	21.81 ± 0.07	21.27 ± 0.13
4:1 POPC-POPS	22.34 ± 0.02	22.24 ± 0.06	21.83 ± 0.03
1:1 POPC-POPS	23.31 ± 0.03	22.92 ± 0.08	22.49 ± 0.07

Dr. Jeffery Klauda's lab conducted molecular dynamic (MD) simulations to investigate the binding of this peptide to 4:1 POPC-POPS membranes. They

employed the highly mobile membrane mimetic (HMMM) approach to enhance simulation efficiency and subsequently converted to all-atom (AA) molecular dynamics simulations. The MD simulations revealed that the ALPS peptide binds at the membrane interface by burying its hydrophobic side in the lipid tails (**Figure 2.5**).

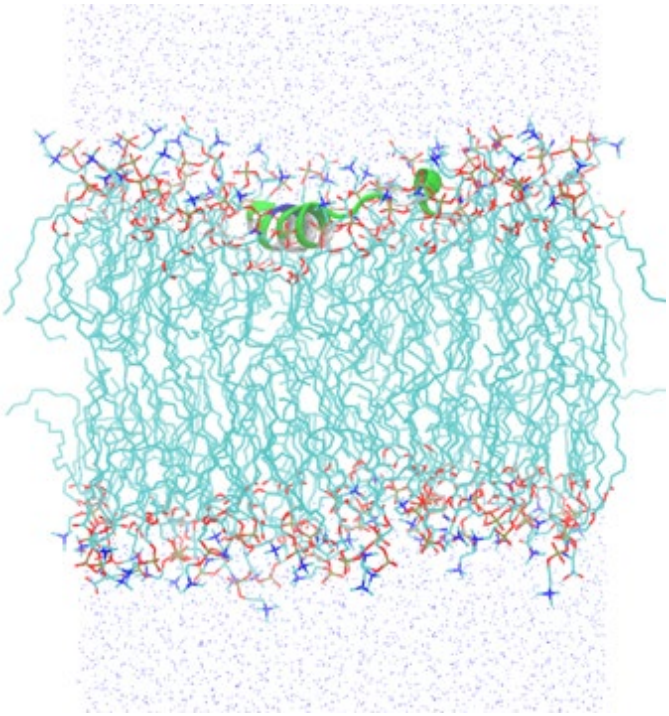

Figure 2.5. MD simulations of the ALPS peptide bound to a membrane with 4:1 POPC-POPS. (Data courtesy of Dr. Jeffery Klauda and Dr. Robert Allsopp).

2.3.3. ALPS binding influences membrane structure

While fluorescence spectroscopy enables us to determine the location of the Trp in the peptide, specifically whether it is situated in the hydrophobic or hydrophilic part of the membrane, it does not reveal any effects of the peptide on the membrane itself. X-ray diffraction offers insights into the structural changes in the phospholipid bilayer caused by the peptide's presence. We employed x-ray diffraction to investigate the effects of incorporating the ALPS peptide in POPC and a binary mixture of POPC

and POPS at a peptide-to-lipid molar ratio of 1:25. X-ray diffraction can provide valuable insights into changes in the bilayer thickness of membranes. In the context of x-ray diffraction measurements, the bilayer thickness was defined by the peak-to-peak distance of the normalized electron density profiles, which corresponded to the phosphate-to-phosphate distance in the bilayer.

The repeat spacing (bilayer thickness + water layer) decreased, and the chain disorder increased (the central trough broadened) with the incorporation of the ALPS peptide for both pure POPC and POPC-POPS mixtures, as seen in the electron density profiles shown in **Figure 2.6**. The observed thinning of the bilayer upon the incorporation of peptides can be attributed to the cross-sectional area expansion at constant hydrocarbon density that occurs when peptides partition at the bilayer-water interface [83, 94, 95]. This is a common feature that is also observed in the presence of peptides that interact with membranes [81]. We also observed that the thickness of the hydrocarbon core (bilayer carbonyl-to-carbonyl distance) significantly decreased after adding the peptide to the bilayers. The strongest thinning effect (2.17 Å) was observed for the 1:1 POPC-POPS mixture at 298 K, which could be due to the electrostatic interaction between Lys15 in ALPS and the anionic POPS lipid (**Table 2.3**).

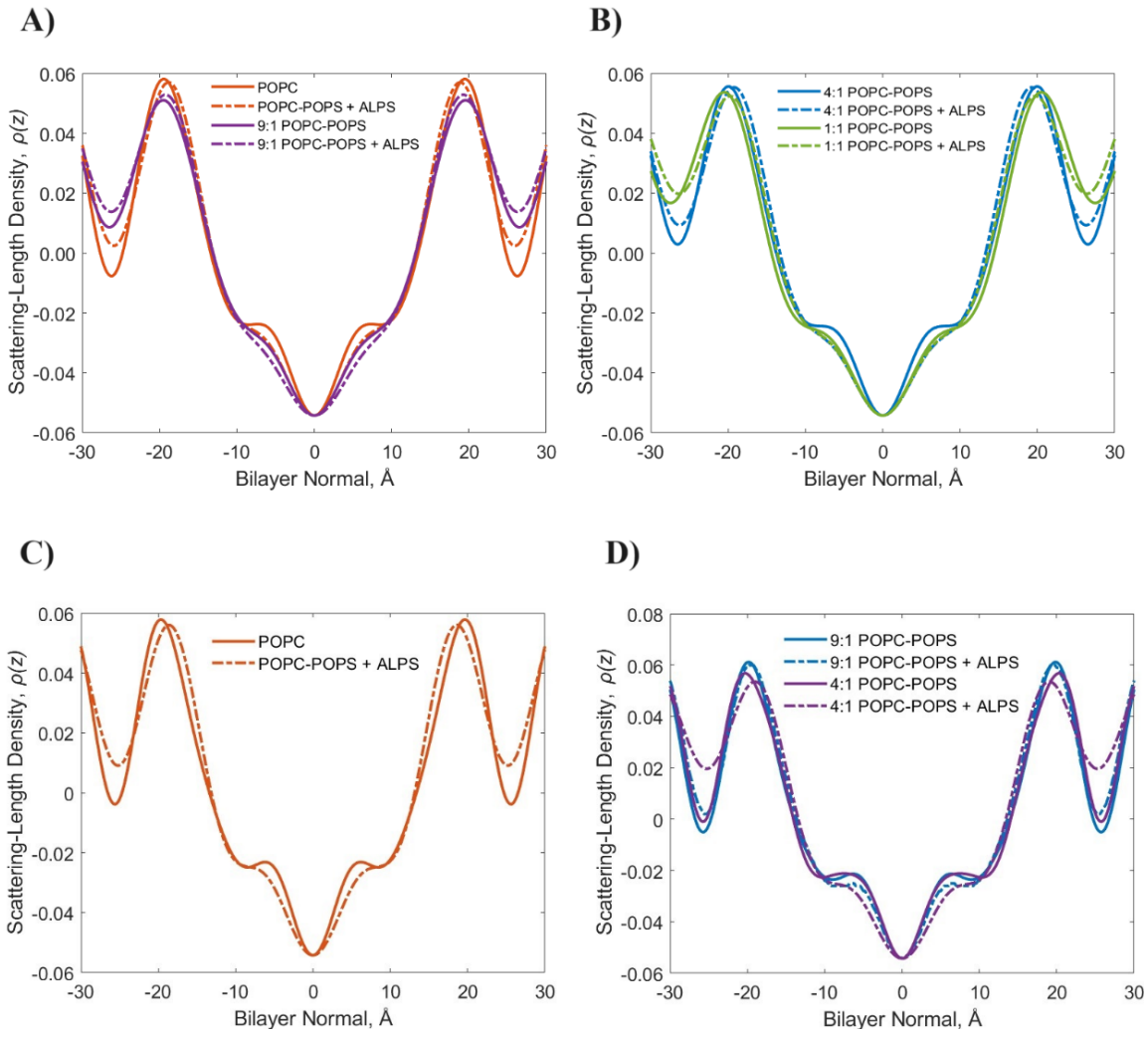

Figure 2.6. X-ray density profile of POPC-POPS bilayers alone and in the presence of ALPS at a peptide to lipid molar ratio of 1:25 and at 97% relative humidity measured **A-B)** at 298 K and **C-D)** at 308 K.

Table 2.3. The membrane parameters obtained from x-ray diffraction measured in the presence and absence of ALPS at a peptide to lipid molar ratio of 1:25 measured at 298 K and 308 K.

	Membranes	***d*, Å**	***Δd*, Å**	***d_{HC}*, Å**	***Δd_{HC}*, Å**
T = 298 K	**POPC**	52.45 ± 0.13	0.61	38.92 ± 0.02	1.24
	POPC + ALPS	51.84 ± 0.17		37.68 ± 0.10	
	9:1 POPC-POPS	52.98 ± 0.13	0.45	39.16 ± 0.03	0.64
	9:1 POPC-POPS + ALPS	52.53 ± 0.28		38.52 ± 0.08	

T = 308 K	**4:1 POPC-POPS**	53.02 ± 0.08	0.46	39.88 ± 0.04	1.28
	4:1 POPC-POPS + ALPS	52.56 ± 0.21		38.60 ± 0.12	
	1:1 POPC-POPS	54.89 ± 0.15	2.17	41.05 ± 0.05	1.65
	1:1 POPC-POPS + ALPS	52.72 ± 0.26		39.40 ± 0.05	
	POPC	51.19 ± 0.10	0.81	39.28 ± 0.03	2.03
	POPC + ALPS	50.38 ± 0.15		37.25 ± 0.10	
	9:1 POPC-POPS	51.44 ± 0.09	0.59	39.56 ± 0.06	0.72
	9:1 POPC-POPS + ALPS	50.85 ± 0.14		38.84 ± 0.07	
	4:1 POPC-POPS	51.46 ± 0.14	0.94	40.60 ± 0.05	1.48
	4:1 POPC-POPS + ALPS	50.52 ± 0.19		39.12 ± 0.09	

*d – Bragg spacing also known as a repeat spacing
*d_{HC} – thickness of hydrocarbon core (bilayer carbonyl-to-carbonyl distance)

2.4 Binding affinity of ALPS to membranes

Having outlined the details regarding the structure of ALPS and its impact on membrane structure, a key remaining question pertains to the strength of the thermodynamic driving force for the Osh4 ALPS peptide when it binds to model membranes. As noted above, tryptophan fluorescence is highly effective for studying how peptides interact with model membranes. For this section, we utilized Trp fluorescence data to estimate the binding constant for the ALPS-membrane interaction. To do this, we performed titration measurements of vesicles with the ALPS peptide. The fluorescence data for this analysis was corrected for scattering artifacts using Ladokhin et al.'s correction method [59] obtained using the fluorescence measurements of pure Trp interacting with the identical model membrane under similar conditions. Using the equation described by Tatulian [90],

we predicted the K_d (dissociation constant) and N (number of binding sites of the peptide) using the corrected titration curve of the ALPS peptide in the presence of 4:1 POPC-POPS liposomes (**Figure 2.7**). From this analysis, we determined that the dissociation constant K_d is 1.88 ± 0.47 μM, which corresponds to ΔG = -7.82 ± 0.15 kcal/mol, and the number of lipids per peptide binding site N equals 7.34 ± 0.08 (which represents the number of lipids bound to the peptide).

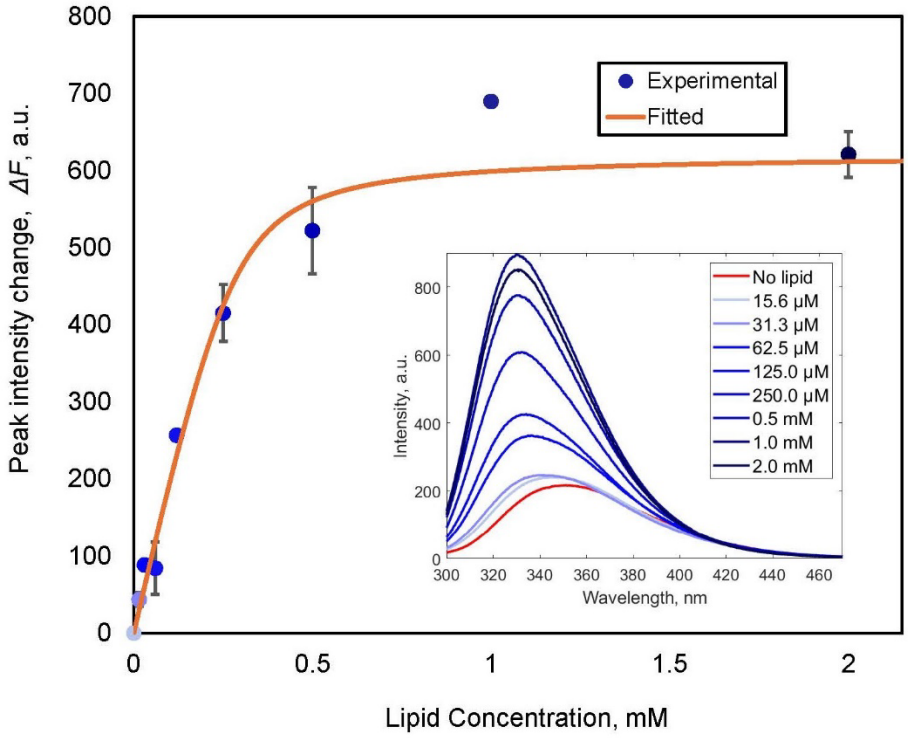

Figure 2.7. Fluorescence intensities resulting from the titration of 20 μM ALPS with 4:1 POPC-POPS liposomes at 298 K. The blue dots represent the corrected peak intensity changes using Trp zwitterion fluorescence as a reference, and the red line represents the fits to the corrected intensities. Error bars represent standard error of the mean (n = 2).

ITC is another crucial experiment that measures binding free energy from a binding isotherm and is a more direct and whole-peptide measure compared to Trp fluorescence based on a single residue. The binding isotherms were determined by

injecting POPC, 4:1 POPC-POPS, and 3:1 POPC-POPS lipid vesicles into the peptide solution, i.e. by gradually reducing the free peptide concentration in the reaction cell. On this basis, the enthalpy of binding of the ALPS peptide to the liposome (ΔH) was determined as well as a binding constant, K_d, reflecting the affinity of the peptide for the liposomes and the stoichiometry of the binding, N, that is the number of binding sites of the peptide (**Table 2.4**). As the negative binding enthalpies indicate, the binding is an enthalpy-driven exothermic reaction (**Table 2.4**).

The binding affinity of ALPS to pure POPC (**Figure 2.8**) is stronger (lower K_d) than to the vesicles containing 4:1 POPC-POPS (**Figure 2.9**) and 3:1 POPC-POPA (**Figure 2.10**) lipids. However, **Tabel 2.4** shows that the addition of POPS at a molar fraction of 20% to POPC lipids (4:1 POPC-POPS) raised the enthalpy released by ALPS binding significantly compared to the pure POPC lipids. This increase in negative enthalpy indicates a greater number of favorable molecular interactions between the ALPS peptide and the lipid molecules of the membrane. The increase in negative enthalpy was accompanied by a decrease in entropy, as obtained by fitting a single-site binding model to the raw data.

For the 4:1 POPC-POPS vesicles, we determined a ΔG value of -4.41± 0.04 kcal/mol, which is marginally higher (less negative) than the Gibbs free energy derived from fluorescence spectroscopy titration, calculated to be -7.82 ± 0.15 kcal/mol. This discrepancy, amounting to -3.41 kcal/mol, could potentially represent the folding energy of the ALPS peptide. Drawing from the CD results, the ALPS peptide undergoes significant conformational changes upon binding with vesicles (**Table 2.4**). Garidel et al. reported that the alteration in Gibbs free energy for the folding

reaction, precipitated by the binding of amphipathic peptides or proteins to phospholipid membranes [96], falls in the range of -0.140 to -0.400 kcal/mol per amino acid, inducing the formation of α-helix or β-sheet structures. The ALPS peptide, which contains 20 amino acids, might have a folding free energy of - 2.8 kcal – -8.0 kcal.

Another reason for the discrepancy in the Gibbs free energy calculated from the Trp fluorescence measurements and ITC could be that during ITC of the 4:1 POPC-POPS mixture, the lipids might have aggregated, leading to a higher K_d value. Therefore, additional ITC experiments at lipid concentrations lower than 100-150 μM will be conducted to ensure the accuracy of the binding constants obtained from ITC.

Table 2.4. Thermodynamic parameters for the ALPS peptide binding to the LUVs vesicle obtained from ITC.

Membrane	**4:1 POPC-POPS**	**POPC**	**POPA**
N	0.73 ± 0.67	0.59 ± 0.35	4.00
K_a, 10^4 M^{-1}	0.17 ± 0.01	13.22 ± 4.55	0.77
ΔG, kcal/mol	-4.41 ± 0.04	-6.88 ± 0.28	-5.30
K_d, μM	592.67±41.95	11.61 ± 5.94	129.53
ΔH, kcal/mol	-107.65±51.65	-0.84 ± 0.07	-0.84
ΔS, cal/mol/K	-346.49 ± 173.20	20.23 ± 0.72	15.00

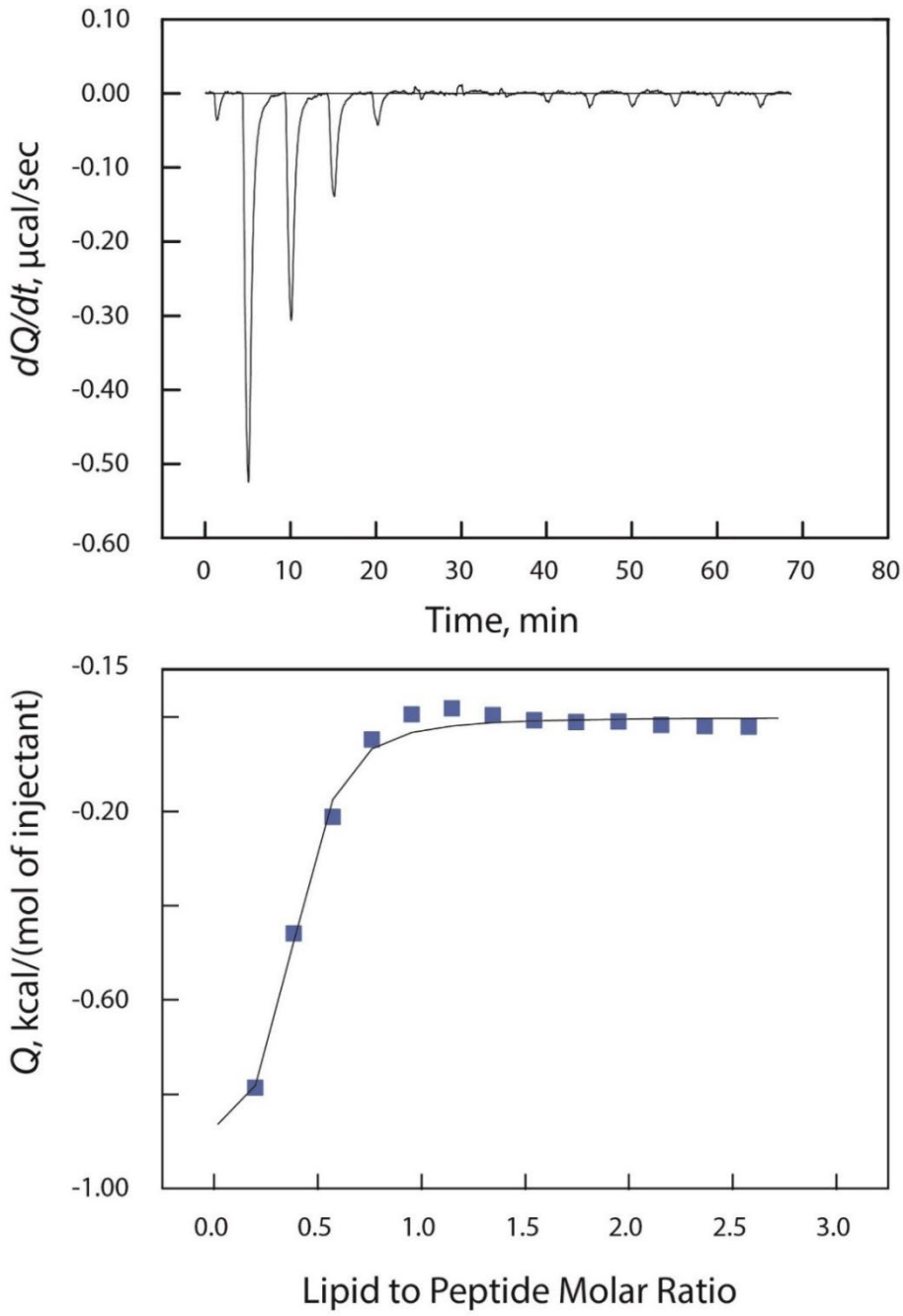

Figure 2.8. ITC thermogram of POPC liposomes (100 nm average size) titrated into the cell containing 100-150 µM ALPS peptide solution. The heat (*Q*) released or absorbed as a result of the interaction was measured at 298 K. The upper plot shows the raw data generated by the series of liposome injections, while the lower plot illustrates the binding isotherm resulting from the integration of each injection peak. The experiments were repeated at least three times. The buffer consisted of 50 mM KCl, 9.3 mM K_2HPO_4, and 0.7 mM KH_2PO_4 (pH=7). The heat of dilution was consistently negligible; thus, it was not deducted from the reaction heat.

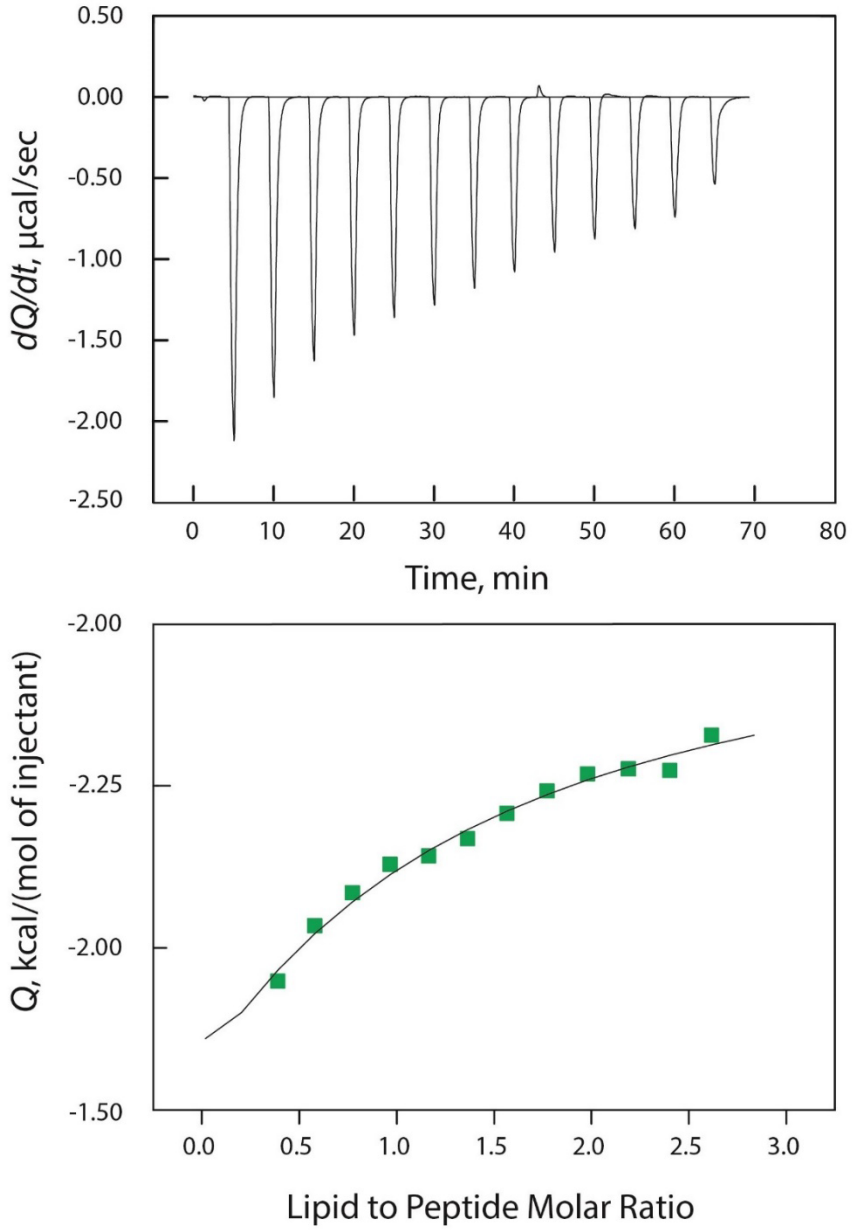

Figure 2.9. ITC thermogram of 4:1 POPC-POPS liposomes (100 nm average size) titrated into the cell containing 100-150 µM ALPS peptide solution. The heat (*Q*) released or absorbed as a result of the interaction was measured at 298 K. The upper plot shows the raw data generated by the series of liposome injections, while the lower plot illustrates the binding isotherm resulting from the integration of each injection peak. The experiments were repeated at least two times. The buffer consisted of 50 mM KCl, 9.3 mM K_2HPO_4, and 0.7 mM KH_2PO_4 (pH=7). The heat of dilution was consistently negligible; thus, it was not deducted from the reaction heat.

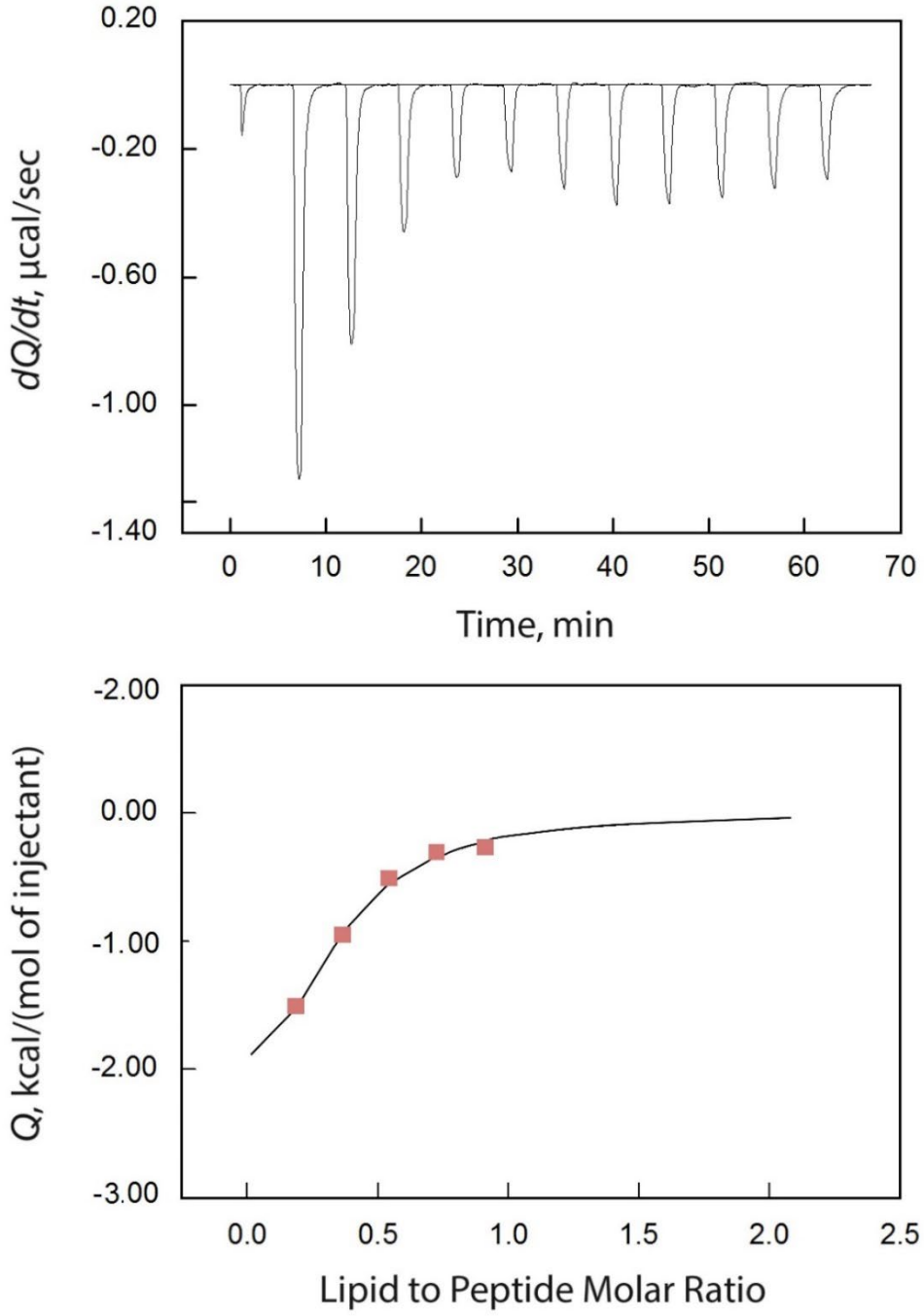

Figure 2.10. ITC thermogram of 3:1 POPC-POPA liposomes (100 nm average size) titrated into the cell containing 100-150 µM ALPS peptide solution. The heat (*Q*) released or absorbed as a result of the interaction was measured at 298 K. The upper plot shows the raw data generated by the series of liposome injections, while the lower plot illustrates the binding isotherm resulting from the integration of each injection peak. The experiments were repeated only one time. The buffer consisted of 50 mM KCl, 9.3 mM K_2HPO_4, and 0.7 mM KH_2PO_4 (pH=7). The heat of dilution was consistently negligible; thus, it was not deducted from the reaction heat.

2.4. Conclusions

This chapter provides a detailed examination of the lipid-binding properties of the ALPS-like motif of Osh4. Using CD measurement, our study revealed that the peptide structure changes from a random coil in the aqueous phase to a structure dominated by a-helical content in the presence of the membrane. In addition, Trp fluorescence studies confirmed that the peptide bound to the membrane and supported the equilibrated MD simulations of the ALPS peptide done by our collaborators. We used fluorescence titration to calculate the binding isotherm and derive the binding constant, which was then compared with a thermally derived ITC binding constant. We have identified a discrepancy in the estimated free energy change by Trp fluorescence titration and ITC (-3.41 kcal/mol), which could be linked to the folding of the ALPS peptide. The presence of the peptide also impacted the membrane thickness, as indicated by the X-ray diffraction data. Our findings highlight that the ALPS peptide shows a preference for particular lipid environments, especially its attraction to anionic lipids. We have shown that specific binding is essential for the motif to trigger structural changes when attaching to a membrane, and these changes are crucial for intracellular lipid movement and membrane structure.

3. Chapter 3: Production and Purification of Osh4

3.1. Introduction

This chapter summarizes the protein expression and purification strategy used for the full-length Osh4 protein. Since the Osh4 protein is known to have other binding domains in addition to ALPS, which was discussed in Chapter 2, it is also important to study the full-length protein. Therefore, expression and purification of the full-length Osh4 were essential for the characterization of its membrane binding mechanism.

A common method for recombinant protein expression involves incorporating a fusion tag (small protein or peptide) to the protein of interest. Fusion tags can assist in correctly folding the protein of interest, thereby improving its solubility and stability [97]. Additionally, they can aid in the efficient identification, production, and isolation of the target protein[98]. Fusion tags such as glutathione S-transferase (GST), polyhistidine (His-tag), and maltose-binding protein (MBP) are commonly used for protein expression in *Escherichia coli*[99]. Selecting the appropriate fusion tag and optimizing the purification conditions was critical for producing a sufficient quantity the Osh4 protein and with an acceptable purity for further biophysical analysis. This process involves molecular cloning, protein expression, cell lysis, affinity and polishing purification all of which will be discussed further in detail.

To optimize the purification process, two different purification partners were compared: GST and 6×His-SUMO tag. The GST tag is frequently integrated into expression vector due to its ability to increase the solubility of expressed proteins and

facilitate their purification through glutathione affinity chromatography. In contrast, 6×His tag allows purification through nickel affinity chromatography, while a small ubiquitin-like modifier (SUMO) tag is known for enhancing protein solubility and proper folding. By comparing the yield and purity of the Osh4 protein produced with these fusion partners, I aimed to determine the most effective strategy for purifying the full-length Osh4 protein, ensuring its suitability for detailed biophysical characterization.

3.2. Methods

3.2.1. Plasmid construction: (pGEX4T1-GST-TEV site-Osh4)

Our lab had stock of the pGEX4T1 plasmid that contained different variants of the Osh4 protein (A169C, D191C, and G241C mutants), which all lacked natural cysteine residues (C88S, C98S, and C229S). The plasmid also had a tobacco etch virus (TEV) protease recognition site and a GST tag fused to the N-terminus. However, we did not have the plasmid containing the wild-type Osh4 protein gene. Therefore, we decided to have the gene commercially synthesized and requested the company (Genewiz, USA) to clone it into a pGEX4T1 plasmid that contained both the TEV cleavage site and GST tag using BamHI and XhoI restriction enzyme sites for cloning. This resulted in pGEX4T1-GST-TEV site-Osh4 plasmid (**Figure 3.1**).

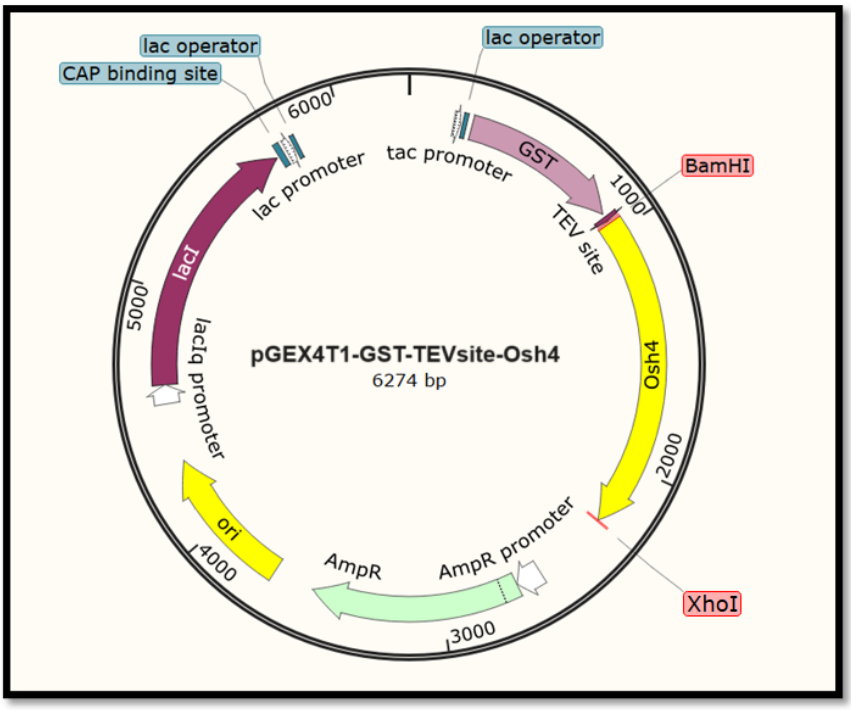

Figure 3.1. Plasmid map of pGEX4T1-GST-TEVsite-Osh4.

3.2.2. Plasmid construct: (pGEX4T1-GST-FactorXa site-Osh4)

We also investigated the possibility of reducing the production cost of the Osh4 protein by using Factor Xa protease instead of the more expensive TEV protease. To do so, we commercially synthesized DNA encoding Factor Xa cleavage site and a portion of the Osh4 protein, which was cloned into the pGEX4T1 plasmid containing a GST tag using BspDI and EcoRI restriction enzyme sites. This resulted in pGEX4T1-GST-FactorXa site-Osh4 plasmid (**Figure 3.2).**

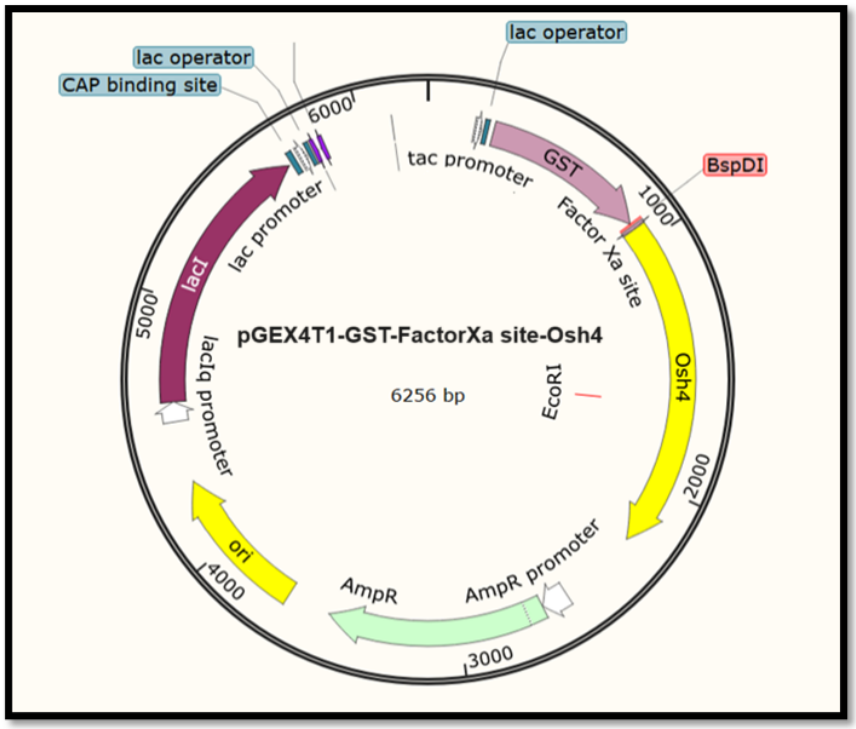

Figure 3.2. Plasmid map of pGEX4T1-GST-Factor Xa site-Osh4.

3.2.3. Plasmid construct: (pET41a+-6×His-SUMO-Osh4(D191C))

To improve the purity and yield of Osh4, we created another expression plasmid using pET41a+-6×His-SUMO (5747 bp) plasmid gifted from Dr. Taylor Woehl's lab. Their plasmid contained a C-terminal 6×His Tag and a SUMO fusion partner. The Osh4 mutant, which had a D191C mutation and all natural cysteines mutated to serine, was amplified from the pGEX4T1-GST-TEVsite-Osh4(ΔC-D191C) plasmid using the BamHI-Osh4-ΔC-D191C-F and Osh4-ΔC-D191C-AgeI-R primers by Vent DNA polymerase (NEB) (**Table 3.1**). Purified pET41a+-6×His-SUMO plasmid and the amplified Osh4 gene was digested using BamHI and AgeI restriction enzymes (New England Biolabs).

The insert corresponding to the Osh4 gene and the vector backbone were ligated at 16 °C overnight using T4 DNA ligase (New England Biolabs). Subsequently, the resultant ligation product was transformed into DH5α strain of electrocompetent *E. coli* cells via electroporation. These transformed cells were then cultured on LB agar plates and incubated overnight to facilitate growth. This resulted in pET41a+-6×His-SUMO-Osh4(ΔC-D191C) plasmid (**Figure 3.3).**

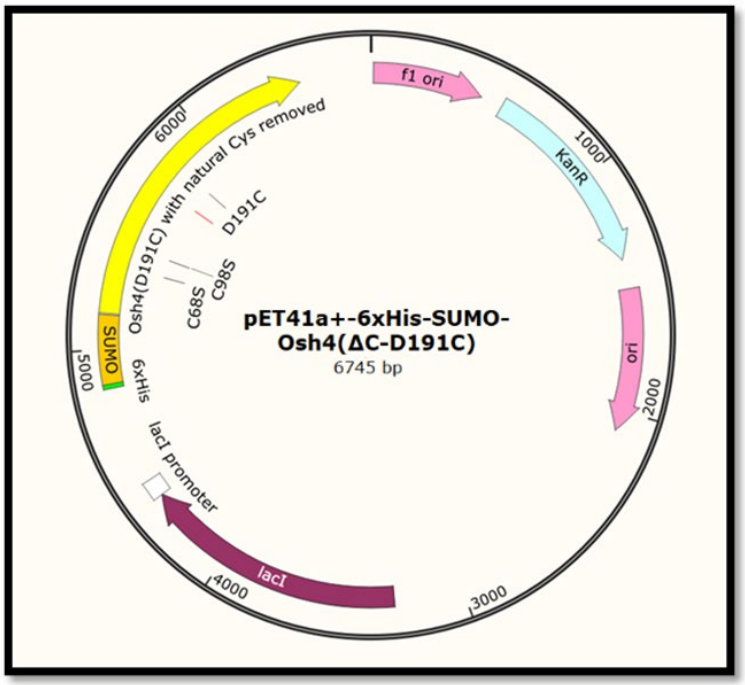

Figure 3.3. Plasmid map of pET41a+-6×His-SUMO-Osh4(ΔC-D191C).

Table 3.1. Oligonucleotides used for the site-directed mutagenesis.

Oligonucleotide sequence name	Sequence (5' to 3')
BamHI-Osh4(ΔC-D191C)-F	AACTAGGGATCCATGTCTCAATACGCAAGCTCATCCTCATGG
Osh4(ΔC-D191C)-AgeI-R	AACTAGACCGGTTTACAAAACAATTTCCTTTTCTTCGTCCCAC AAC
C191D-F	GGTCACACTATGTTGGATATTAAGGACGAGAGTTATTTGGTT ACCCCACCT
C191D-R	AGGTGGGGTAACCAAATAACTCTCGTCCTTAATATCCAACAT AGTGTGACC
P310C-F	AGCCTTTGGAGGAGCAACACTGTCTGGAAAGTAGAAAAGCCT G
P310C-R	CAGGCTTTTCTACTTTCCAGACAGTGTTGCTCCTCCAAAGGCT
L207C-F	CCACCTCCATTGCATATTGAAGGTATTTGTGTCGCTTCTCCCT
L207C-R	AGGGAGAAGCGACACAAATACCTTCAATATGCAATGGAGGT GG
F239C-F	TGAATTTTCAGGTAGAGGCTACTGTTCTGGTAAAAAGAATTC ATTCA
F239C-R	TGAATGAATTCTTTTTACCAGAACAGTAGCCTCTACCTGAAA ATTCA
G241C-F	GCCTTGAATGAATTCTTTTTACAAGAAAAGTAGCCTCTACCTG
G241C-R	CAGGTAGAGGCTACTTTTCTTGTAAAAAGAATTCATTCAAGG C

3.2.4. Site-directed mutagenesis

Site-directed mutagenesis was used to remove the three natural cysteines and place a single cysteine in regions of interest for spin labeling for high-field cycling NMR studies. P310C, L207C, F239C, and G241C mutants were created using pET41a+-6×His-SUMO-Osh4(ΔC-D191C) plasmid. For this purpose, we introduced new cysteine mutations at the desired sites while restoring the natural cysteine at the D191 position using the C191D-F and C191D-R primers (**Table 3.1**). Using the primers in the table above, additional site-directed mutations were introduced via the QuikChange II Site-Directed Mutagenesis Kit from Agilent. As a result, we produced 5 variants of Osh4 protein (ΔC-D19C, ΔC-P310C, ΔC-L207C, ΔC-F239C, and ΔC-G241C).

3.3. Protein expression and preparation

After plasmid construction, all plasmids were sequenced to ensure accuracy and then transformed into *E. coli* BL21(DE3) cells for protein expression. An overnight culture of around 12 mL for each fusion construct was subcultured into 1000 mL of fresh Luria-Bertani (LB) broth supplemented with ampicillin (100 μg/mL) at an optical density of OD_{600} = 0.05 and grown until it reached mid-log phase (OD_{600} = 0.6-0.8) at 37 °C. Isopropyl β-D-1-thiogalactopyranoside (IPTG) was added to each culture aliquot to a final concentration of 100 μM to induce the expression of the fusion proteins. The cells were then incubated at 18 °C for 16 hours overnight.

Protein expression levels were assessed through Western blotting in the crude soluble cell lysates. Sample volumes were normalized according to culture volume and resolved on Any kD Mini-PROTEAN TGX gels (Bio-Rad). After electrophoresis, gels containing proteins were transferred onto a polyvinylidene difluoride (PVDF) membrane. The detection of the GST-Osh4 fusion proteins was carried out using an anti-GST antibody from rabbit (Abcam) and the detection of the 6×His-SUMO-Osh4 fusion protein was performed using an anti-6×His antibody from goat (Abcam). For visualization, the membrane was treated with Clarity Western ECL substrate (Bio-Rad), and the chemiluminescent signal was captured using the ChemiDoc MP imaging system (Bio-Rad).

3.4. Media optimization

The growth medium was optimized to enhance the expression of the target Osh4 protein. Three well-known bacterial growth media were evaluated: LB, Terrific Broth (TB), and Super Broth (SB). For each fusion construct, an overnight culture of approximately 5 mL was subcultured into 20 mL of fresh medium, supplemented with ampicillin (100 μg/mL), starting at an optical density (OD600) of 0.05. The cultures were grown until they reached the mid-log phase (OD600 = 0.6-0.8) at 37 °C. IPTG was then added to each culture tube to a final concentration of 100 μM to induce the expression of the fusion proteins. Following this, the cells were incubated at 37 °C for 5 hours. The levels of expression were analyzed using a western blot with an anti-GST antibody.

3.5. Cell strain optimization

To enhance the expression of the Osh4 target protein, we conducted an optimization study using four well-characterized *E. coli* strains: DH5α, BL21, BL21(DE3), and MC4100. The electrocompetent variants of each strain were prepared and then transformed with the pGEX4T1-GST-FactorXa site-Osh4 plasmid via electroporation. Subsequently, a 5 mL overnight culture of each transformed strain was used to inoculate 20 mL of fresh medium, following the previously detailed protocol. After incubation for 5 hours at 37 °C, the cells were collected for protein analysis. The expression levels of the protein were evaluated by western blot, employing an anti-GST antibody to detect the fusion protein.

3.6. Protein extraction and purification

3.6.1. GST-Osh4 constructs

The cells were collected by centrifugation at 4000×g and then suspended in a buffer containing 125 mM Tris, 100 mM Sodium chloride, pH=8. To prevent degradation of extracted proteins, 50 µL of protease inhibitor cocktail set I (Calbiochem) was added to the cell lysate from 2 L of cell culture. To reduce the viscosity of the lysate, 10 µL of benzonase nuclease (MilliporeSigma) was also added to the cell lysate from 2 L of cell culture. The cells were lysed using a high-pressure homogenizer (Avestin EmulsiFlex C3). Lysates were pelleted by centrifugation at 12,000 ×g for 20 min. The supernatants containing the soluble fraction of the cell lysates were collected and passed through a 0.2 µm sterile filter to remove cell debris.

Pierce GST spin purification kit (ThemoFisher Scientific) was used to purify the GST-Osh4 fusion protein from cellular lysates. The column was first equilibrated with resin-bed volumes of the Equilibration/Wash Buffer containing 125 mM Tris, 150 mM sodium chloride, pH 8.0. Then, the protein extract was added to the column and incubated for 60 min at room temperature to allow the GST-fusion protein to bind. The column was washed three times with two resin-bed volumes of the Equilibration/Wash Buffer to remove the impurities. Finally, the fusion proteins were eluted three times with one resin-bed volume of Elution Buffer containing 10mM glutathione, 125mM Tris, 150mM Sodium chloride, pH 8.0.

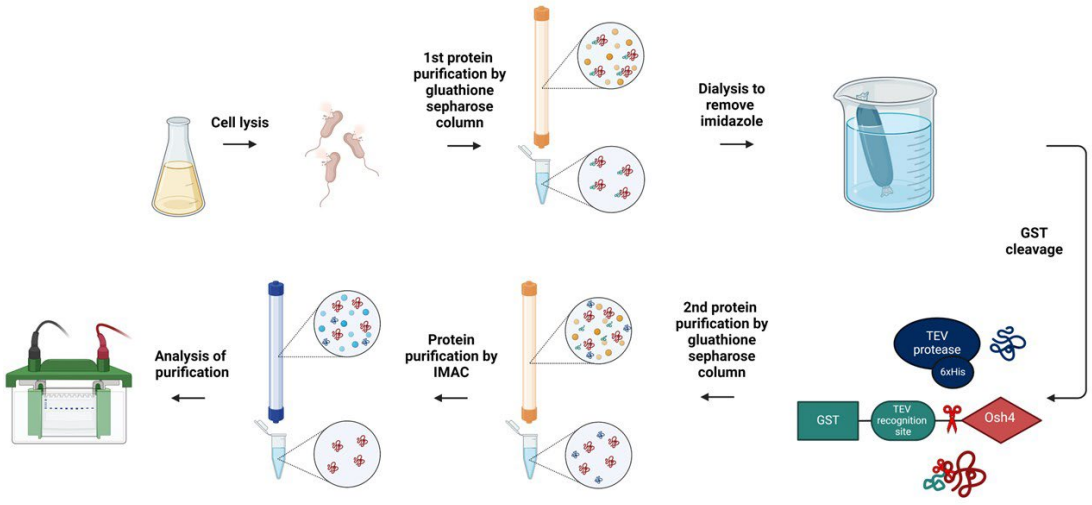

Figure 3.4. Schematic diagram of purification of GST-Osh4 constructs. Figure made in BioRender.com.

The GST-Osh4 constructs had either TEV or Factor Xa protease cleavage sites between the GST and the Osh4 proteins, so TEV (New England Biolabs) or Factor Xa (New England Biolabs and Haematologic Technologies) proteases, respectively, were used to remove unwanted GST tag. The protein extract was dialyzed against the protease cleavage buffer overnight at 4°C. After the cleavage, unwanted GST tags were removed by passing the protein extract through the glutathione column (**Figure 3.4**).

The Factor Xa protease was removed by passing the reaction mixture through a small benzamidine-agarose column (Cytiva HiTrap). The TEV protease was removed by passing the reaction mixture through an Ni-NTA spin Kit (Qiagen). Protein sample from each step of purification process were analyzed using SDS-PAGE electrophoresis.

3.6.2. 6×His-SUMO-Osh4 construct

To purify the 6×His-SUMO-Osh4 fusion protein from cellular lysates, EconoFit prepacked immobilized metal affinity chromatography (IMAC) column (Bio-Rad) was used by connecting it to an NGC liquid chromatography system (Bio-Rad). The column was equilibrated five column volumes of the Wash Buffer I buffer containing 300 mM sodium chloride, 50 mM sodium phosphate, 5 mM imidazole, pH 8.0. After loading the sample lysate, the column was washed with 6 column volumes of Wash Buffer I and Wash Buffer II (300 mM sodium chloride, 50 mM sodium phosphate, 25 mM imidazole, pH 8.0). The fusion protein was eluted using Elution Buffer containing 300 mM sodium chloride, 50 mM sodium phosphate, 350 mM imidazole, pH 8.0. Soluble lysate, flow-through, washes, and elutes were collected to further run a gel. Coomassie stain was used to estimate the purity of the proteins.

The eluate was applied to HiLoad 16/600 and 26/600 Superdex 75 size exclusion chromatography column (SEC) to remove the aggregates and other impurities. The Superdex column was equilibrated with one column volume of 0.05 M $NaPO_4$, 0.15 M NaCl, pH 7.2. Next, the sample was loaded into the column and the protein of interest was eluted with 2 column volumes of the same equilibration buffer.

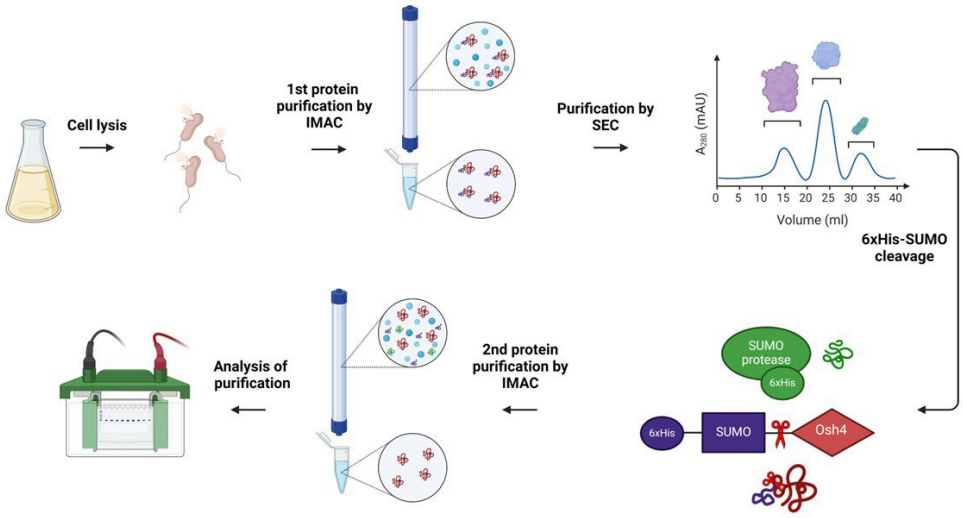

Figure 3.5. Schematic diagram of purification of GST-Osh4 constructs. Figure made in BioRender.com.

After the size exclusion purification, SUMO protease (containing a 6×His Tag) and 10× SUMO protease buffer (500 mM Tris-HCl, 1.5 M NaCl, 5 mM DTT, pH 8.0) were added to cleave the SUMO moiety overnight at 4 °C. After the cleavage, the protein solution was dialyzed against a buffer containing 300 mM sodium chloride, 50 mM sodium phosphate, 5 mM imidazole, pH 8.0, using a 30 kDa Amicon Ultra centrifugal filter devices. After dialysis, the SUMO protease and SUMO degradation product (6×His-SUMO tag) are removed over an Ni-NTA spin Kit (Qiagen) (**Figure 3.5**). Protein sample from each purification step was analyzed for the purity and yield using SDS-PAGE electrophoresis.

3.7. Results and discussion

3.7.1. Plasmid construct: (pET41a+-6×His-SUMO-Osh4(D191C))

The Osh4 protein gene, containing a ΔC-D191C mutation, was amplified and its size was verified using DNA gel electrophoresis. The results confirmed the expected DNA fragment size of 1328 bp, as shown in **Figure 3.6A**. In parallel, pET41a+-6×His-SUMO plasmid, containing a different gene of interest, was digested with AgeI and BamHI enzymes. The size decreased from 5747 bp to 5417 bp after digestion, as illustrated in **Figure 3.6B**. After ligation, the resulting plasmid, pET41a+-6×His-SUMO-Osh4(ΔC-D191C), was confirmed to have a size of 6745 bp. Subsequent cleavage with AgeI and BamHI enzymes produced two fragments on a DNA gel: the backbone (5417 bp) and the Osh4 gene insert (1328 bp), as shown in **Figure 3.6C**.

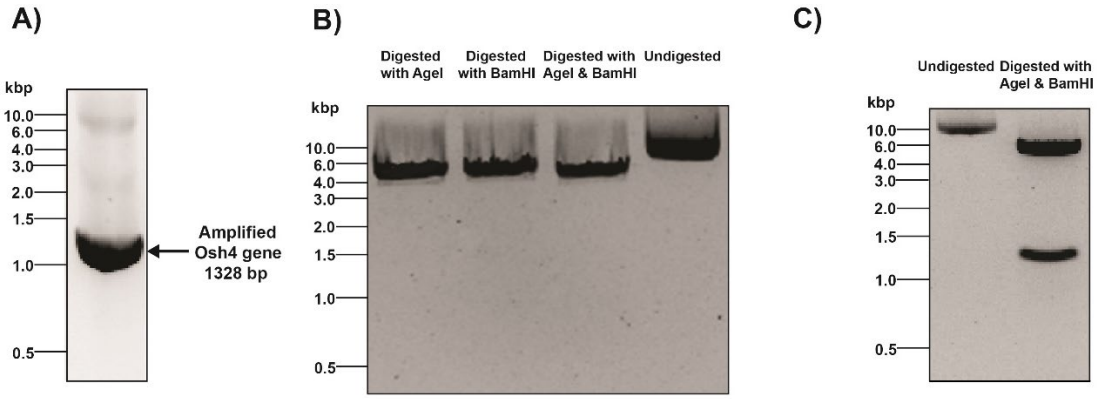

Figure 3.6. **A)** Amplified Osh4 protein's gene with ΔC-D191C mutation **B)** Digested pET41a+-6×His-SUMO plasmid **C)** Ligation product pET41a+-6×His-SUMO-Osh4(ΔC-D191C).

3.8. Protein expression and preparation

Western blot analysis revealed the expression of both GST-TEV site-Osh4 (76.6 kDa) and GST-Factor Xa-Osh4 (75.8 kDa) fusion proteins. However, alongside the desired

constructs, there was also detectable expression of protein (25 kDa), which can be seen in **Figure 3.7**. This indicates that while the expression system is functional for the fusion proteins, there is a concurrent generation of impurities. This byproduct can consumes purification column capacity, thereby reducing the overall yield of protein purification.

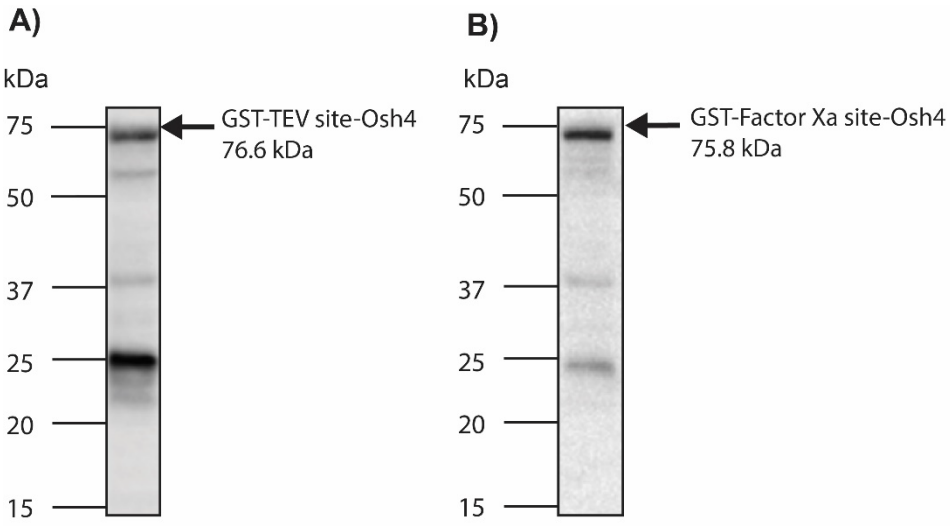

Figure 3.7. A) Expression of the GST-TEV site -Osh4 fusion protein. **B)** Expression of the GST-Factor Xa site -Osh4 fusion. Both fusion proteins were expressed in BL21(DE3) cells at 37 °C for 5 h with 100 μM IPTG. The Western blots were probed using an anti-GST (rabbit) antibody.

Western blot analysis was conducted on the wild-type 6×His-SUMO-Osh4 fusion protein, a variant where all naturally occurring cysteine residues were substituted with serine (referred to as WT-ΔC), and additional mutants. In these additional mutants, all natural cysteines where mutated to serine, while residues of interest were altered to cysteines for spin labeling. All variants were successfully expressed, with the wild type and ΔC-D191C exhibiting the highest level and lowest level of production respectively (**Figure 3.8)**.

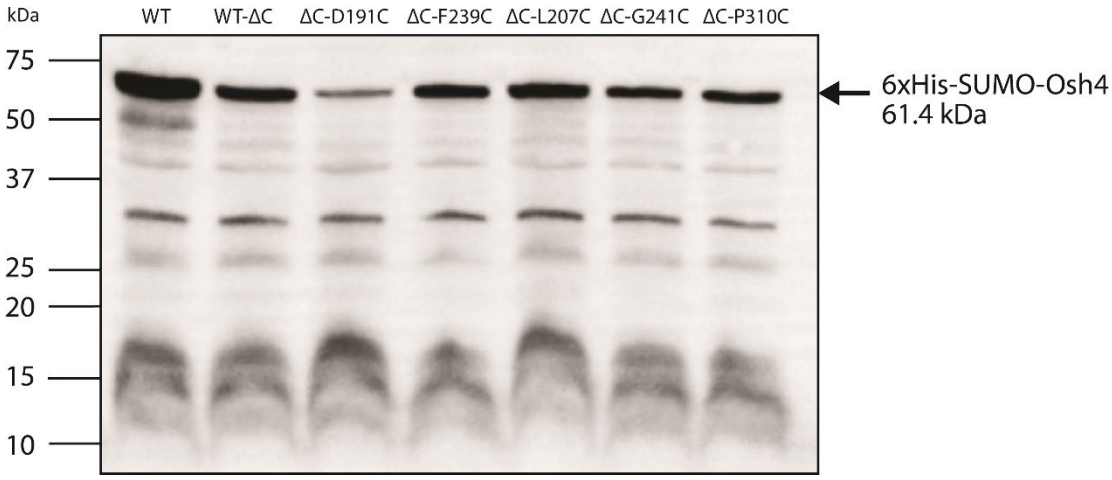

Figure 3.8. Expression of the 6×His-SUMO-Osh4 fusion protein which was expressed in BL21(DE3) cells at 37 °C for 5 h with 0.1 mM IPTG. The Western blots were probed using an anti-6×His (rabbit) antibody.

3.9. Media optimization

Media optimization revealed the highest expression levels of the GST-TEV site-Osh4 fusion protein in cells cultured in LB medium as shown in **Figure 3.9**. In contrast, TB and SB media did not show significant expression of the fusion protein and only produced non-target free GST. Therefore, it was determined that LB growth media would be used for all subsequent protein expressions.

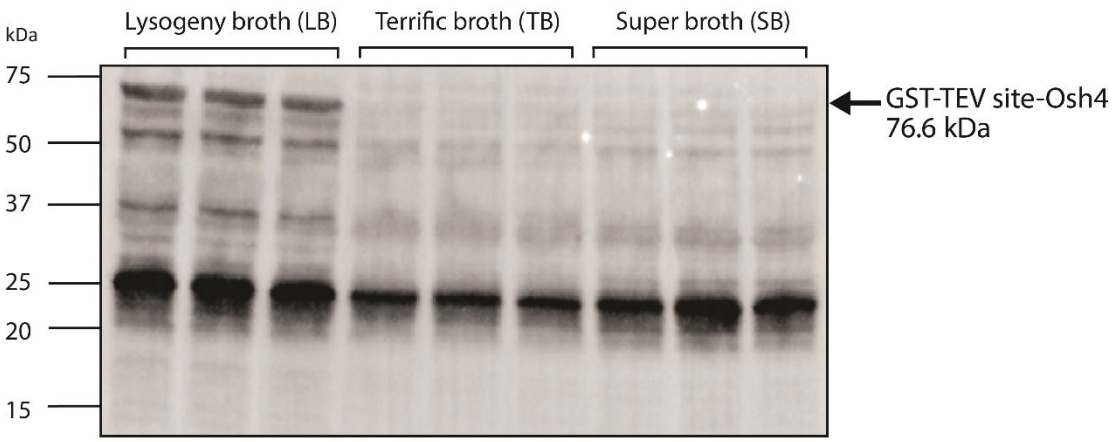

Figure 3.9. Expression of the GST-TEV site -Osh4 fusion protein, which was expressed in BL21(DE3) cells in three different media (LB. TB, and SB) at 37 °C for 5 h with 100 μM IPTG. Western blots were probed using an anti-GST (rabbit) antibody. To eliminate any variations between the samples, each of them was loaded into three wells.

3.10. Cell strain optimization

Cell strain optimization showed that the BL21 and BL21(DE3) strains exhibited the highest expression of the GST-Factor Xa site-Osh4 fusion protein (**Figure 3.10**). In contrast, the MC4100 strain showed negligible expression levels, and the DH5α strain produced an excess of non-target GST, potentially interfering with subsequent purification processes.

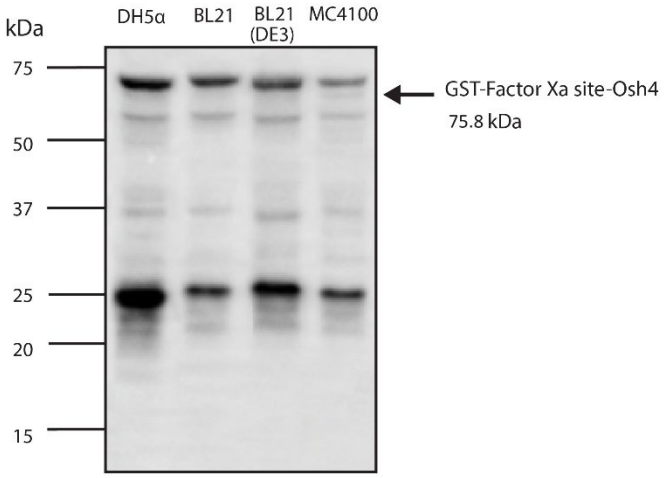

Figure 3.10. Expression of the GST-Factor Xa site -Osh4 fusion protein, which was expressed in four different *E. coli* strains (DH5α, BL21, BL21(DE3), AND MC4100) at 37 °C for 5 h with 0.1 mM IPTG. Western blots were probed using an anti-GST (rabbit) antibody.

3.11. Protein extraction and purification

3.11.1. GST-Osh4 constructs

The GST-TEV site-Osh4 fusion and GST-Factor Xa site-Osh4 fusion constructs were unable to generate an Osh4 protein solution of the necessary purity for our research (**Figures 3.11**). Furthermore, the protein yield was low, with only 0.1 mg/mL of a 0.5 mL solution per 2 L of BL21(DE3) cell culture. Moreover, the final protein solutions exhibited poor purity in both instances. The presence of impurities, closely matching the size of the Osh4 protein, complicated their removal via size-exclusion chromatography (SEC) columns. Consequently, we were compelled to explore alternative fusion constructs to enhance the purity and yield of the protein.

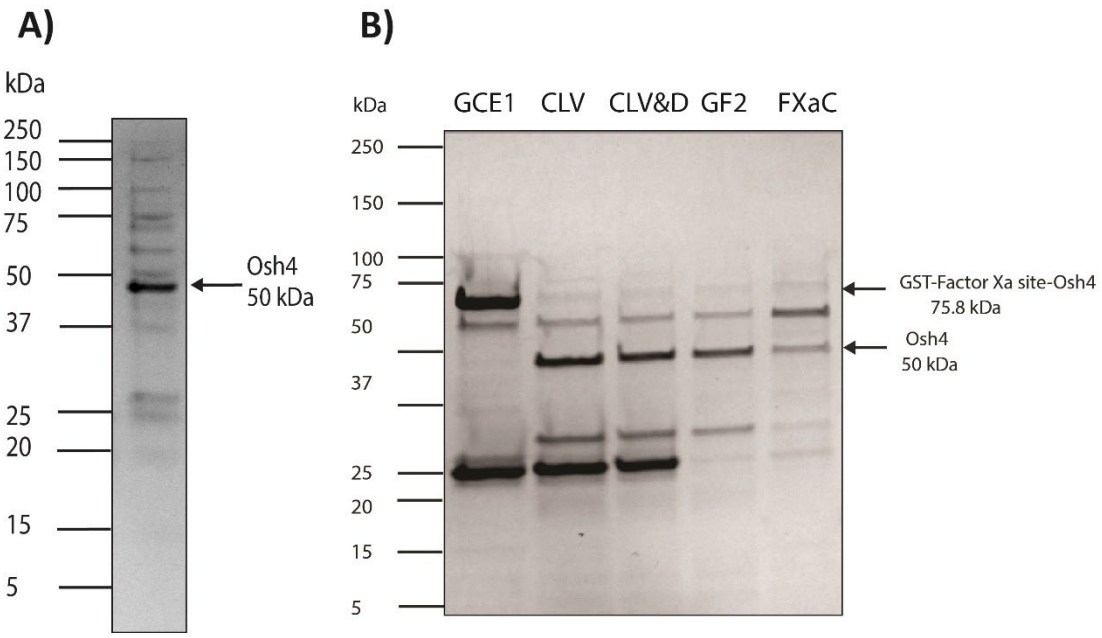

Figure 3.11. A) Purified and 3-fold concentrated Osh4 protein solution from the GST-TEV site-Osh4 fusion protein construct visualized via gel electrophoresis. **B)** Purification stages of the GST-Factor Xa site-Osh4 fusion protein visualized via gel electrophoresis. The image shows protein fractions collected at different purification steps: the initial eluate from the glutathione agarose column (GCE1), the overnight Factor Xa cleavage product (CLV), the dialyzed cleavage solution (CLV&D), the flow-through from a subsequent glutathione agarose column (GF2), and the final flow-through from the benzamidine-agarose column (FXaC) used for the removal of Factor Xa protease. The bands corresponding to the GST-Factor Xa site-Osh4 fusion protein (75.8 kDa) and the cleaved Osh4 protein (50 kDa) are indicated with arrows.The purity assessment of the fusion proteins was evaluated using Coomassie Brilliant Blue staining.

3.11.2. 6×HisSUMO-Osh4 construct

The SUMO protein is a fusion partner that has gained recognition for its ability to enhance the solubility and proper folding of proteins that are often difficult to express [100]. By attaching the SUMO protein to the target protein, it can help improve its stability, solubility, and overall functionality. Therefore, we decided to switch from using the GST tag to the SUMO tag. After purification on the IMAC column, the

protein solution was subjected to a size exclusion purification where monomers were purified from our the aggregates (**Figure 3.12**).

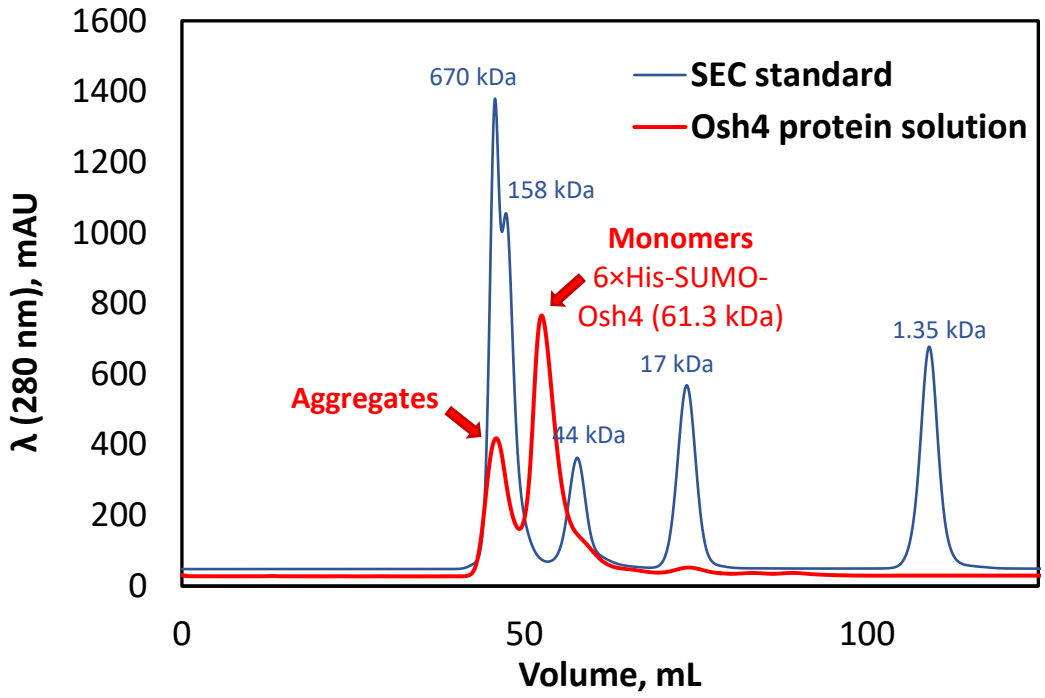

Figure 3.12. Size exclusion chromatogram of the 6xHisSUMO-Osh4 fusion protein compared to the gel filtration standard (Bio-Rad).

This allowed us to achieve around 85% purity and a significantly higher protein yield (**Figure 3.13**). From 2L of BL21(DE3) cell culture, we were able to obtain around 1 mL of Osh4 protein with a concentration of 0.4-0.5 mg/mL. Our results are in agreement with Marblestone et al [101] who demonstrated that purification with SUMO enhances protein expression and purity than GST, maltose-binding protein (MBP), thioredoxin (TRX), and ubiquitin (UB). The advantage of using SUMO is that it improves the expression and solubility of recombinant proteins, while also allowing for the production of proteins with native sequences.

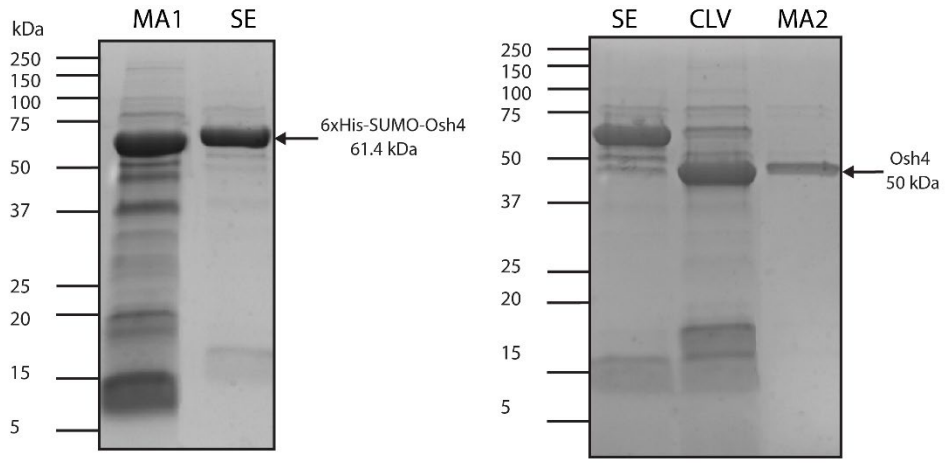

Figure 3.13. Purification stages of the 6×His-SUMO-Osh4 fusion protein. The purification process and purity assessment of the fusion proteins were monitored using Coomassie Brilliant Blue staining. Displayed are the fractions obtained from the initial immobilized metal affinity chromatography (MA1), followed by size exclusion chromatography (SE). Subsequent cleavage with SUMO protease is depicted (CLV), along with the resulting flow-through from a second round of immobilized metal affinity chromatography (MA2).

3.12. Conclusions

In conclusion, our initial attempts at recombinant protein production of Osh4 using the GST fusion partner resulted in low protein concentrations and poor purity. Despite optimizing various purification parameters such as culture media, growth temperature, plasmid backbone, and cleavage site, no substantial enhancements were observed with the GST fusion system. Consequently, we explored alternative strategies, specifically the combination of a 6×His tag with a SUMO tag. This approach significantly improved both the yield and purity of the Osh4 protein. The effectiveness of the SUMO tag aligns with existing literature that emphasizes its better ability to enhance protein solubility and expression. Our findings highlight the critical role of choosing an appropriate fusion tag for optimizing protein purification

processes, demonstrating that the SUMO tag system can be a more effective alternative for producing high-quality recombinant proteins.

4. Chapter 4: Conclusion and future work

The dissertation illustrated the preference of the ALPS peptide for specific lipid environments, especially its attraction to anionic lipids. The presence of anionic lipids was shown to be essential for the motif's ability to cause structural changes when binding to a membrane as shown in Chapter 2. These changes likely play a crucial role in intracellular lipid trafficking and membrane organization. To understand how Osh4 forms MCSs between two membranes, it is necessary to investigate how the membranes interact with the full-length protein, which was produced using recombinant protein production methods described in Chapter 3.

Previous research studies produced Osh4 protein using the pGEX-4T vector [42, 43], where Osh4 was fused to a GST tag. However, our attempts to purify Osh4 with this GST tag did not yield the high purity and yield necessary for our full-length protein studies. After comparing the use of two different fusion tags, it was determined that the SUMO tag resulted in higher protein yield and greater protein purity. Although refining this purification process was time-consuming, these improvements will facilitate future experiments with the full-length Osh4 protein to enhance our understanding of the mechanisms of lipid transport between membranes.

Building on the findings of this dissertation, several additional experiments could be conducted. This future work would involve further characterizing ALPS binding to a model membrane using neutron diffraction, as well as investigating the full-length protein using high resolution field cycling NMR and cryo-EM.

4.1. Neutron diffraction

Neutron diffraction (ND) can be valuable for studying the structure of ALPS-membrane complexes. These measurements can be done at the NIST Center for Neutron Research (NCNR). Our beam time was approved by NIST, and we have synthesized the ALPS peptides, both in deuterated (H_2N-**M**SQYASSSSWTS**FL**KSIASF-amide, with deuterated Met, Phe, and Leu) and non-deuterated forms. Currently, the instrument is under repair. Once operational, we can use the Mihailescu lab's ND methodology [83, 102-104] to elucidate the peptides' insertion depth and the lipid spacing in the multilayer. For that, we will need to prepare samples as oriented lipid multilayers incorporating ALPS.

These studies can clarify the ALPS-like peptide's structural details, including residue positions and orientations within various membrane compositions. ND is essential for resolving the peptide's structure within the bilayer. Deuterium difference analysis can help identify the deuterated peptides' distinct deuterium profiles. This method will facilitate understanding the peptide structure relative to lipid organization.

Additionally, we can use H_2O/D_2O exchange to explore the bilayer's structural changes and water infiltration caused by peptide binding. By varying H_2O/D_2O ratios, we can investigate the water distribution around the peptide and lipid headgroups, and assess the bilayer's scattering length density alterations due to the peptide. This comprehensive approach will enhance our understanding of the peptide's interaction with the membrane.

4.2. NMR and high resolution field cycling NMR

Nuclear magnetic resonance (NMR) spectroscopy methods can be utilized to obtain atomic-level details about the binding of Osh4 to phospholipid membrane. Naturally, phospholipids have two nuclei that can be detected by NMR–^{1}H and ^{31}P. Studying POPC lipids with ^{1}H NMR is challenging primarily due to the complexity of their spectrum, which arises from the many hydrogen atoms present in these molecules (**Figure 4.1**). Additionally, the motion of lipid molecules in bilayers or vesicles can cause the NMR signals to broaden, obscuring the detailed structure of the spectrum. Consequently, other NMR nuclei like ^{31}P or ^{13}C can yield more insights into lipid structure. For ^{13}C NMR experiments, phospholipids such as POPC need be labeled with stable ^{13}C isotope. In contrast, ^{31}P is a naturally occurring isotope of phosphorus. Therefore, ^{31}P NMR studies of phospholipids do not require labeling, as this isotope is already present in the phospholipid molecules.

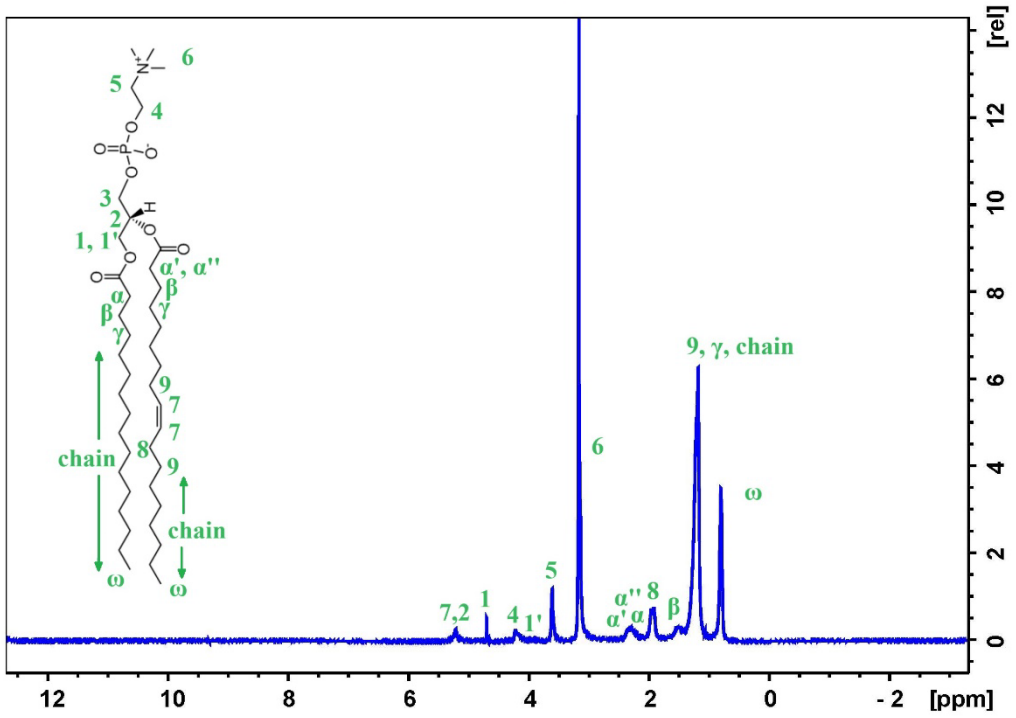

Figure 4.1. The ^{1}H NMR spectrum of vesicles containing POPC (5 mM) lipids sealed in a 5-mm NMR tube (524-PP-7 Wilmad-LabGlass) in ultrapure water measured by 600 MHz Bruker Ultrashield Plus NMR Spectrometer with BBFO probe.

The T_1 relaxation time constant, also referred to as the longitudinal (or spin-lattice) relaxation time, is a crucial parameter in NMR that indicates the speed at which magnetization reverts to its equilibrium state following pulse excitation. ^{31}P T_1 relaxation measurement was performed on POPC lipids using the pulse program described in the Appendix. POPC, which has one phosphorus in its headgroup, showed a chemical shift around -1 ppm.

In the T_1 experiment, nuclei are initially allowed to relax completely to their equilibrium states along the z-axis. The signals are then inverted by applying a 180° pulse. Subsequently, the signals undergo relaxation for a period τ, which is varied across different experiments. After each variable time interval, a 90° pulse is applied,

leading to the acquisition of an NMR spectrum [105]. The peak intensities in this spectrum change based on the adjustable delay τ and the specific T_1 relaxation time of the components. We applied a set of eight delays (τ = 0, 0.1 s, 1 s, 2 s, 4 s, 8 s, 10 s, and 20 s) and measured the ^{31}P NMR signal (**Figure 4.2**). Using TopSpin's built-in data analysis toolbox called Dynamic Center, the recorded signal intensity was then fitted into the following equation:

$$I = I_0\left(1 - e^{-\tau/T_1}\right) \qquad (4.1)$$

where I is the output variable intensity of signal, τ is the input variable delay time, and T_1 is the unknown relaxation time. Fitting revealed that POPC had a T_1 of 631 ms, which corresponds to a relaxation (R_1) of 1.58 s^{-1}. (**Figure 4.3**)

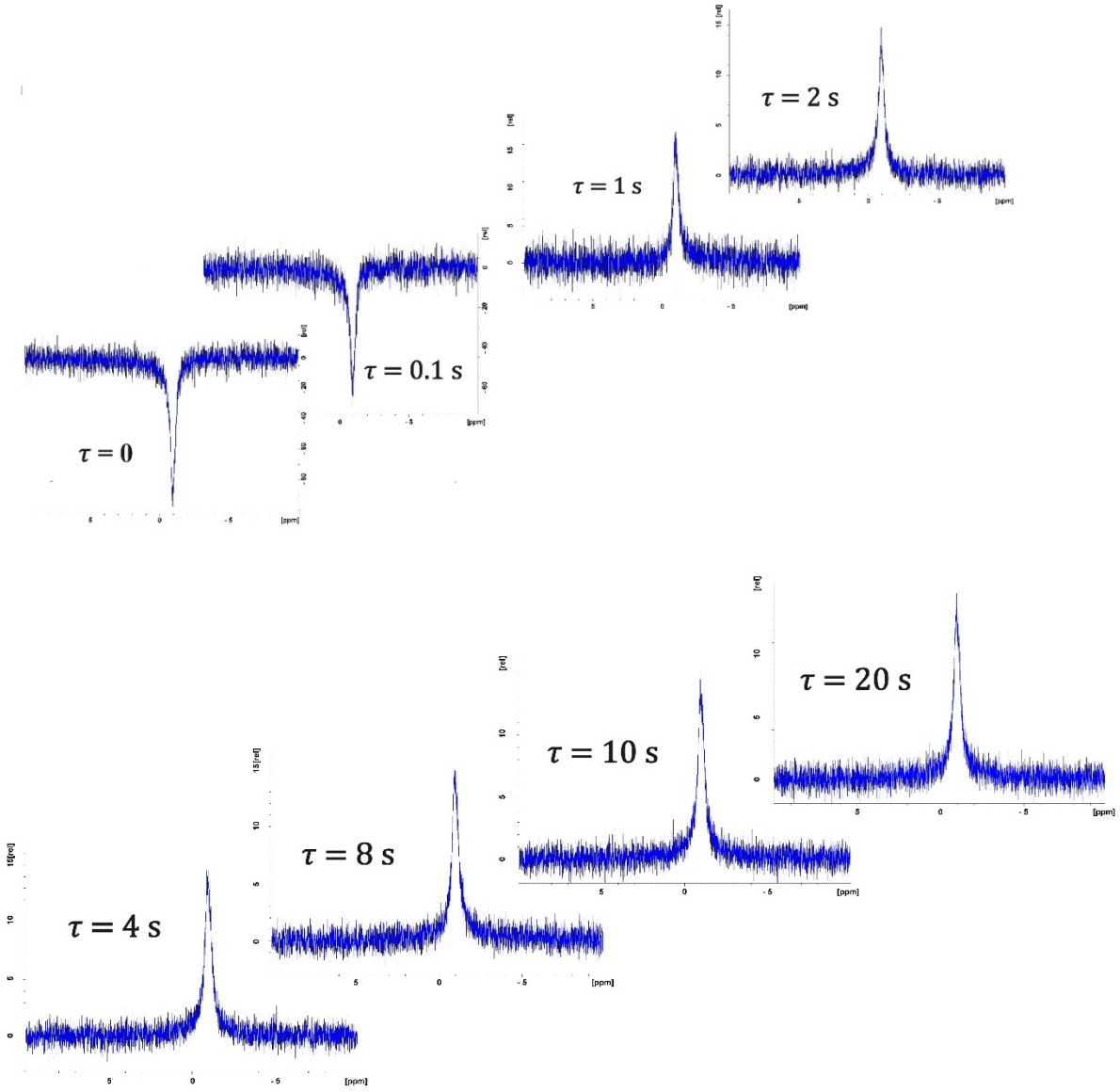

Figure 4.2. ^{31}P spectra from a T_1 experiment for POPC (10 mM) liposomes (100 nm in diameter) sealed in a 5-mm NMR tube (524-PP-7 Wilmad-LabGlass) in ultrapure water measured by 600 MHz Bruker Ultrashield Plus NMR Spectrometer with BBFO probe. The relaxation delay time, τ, in seconds spent is indicated next to each spectrum.

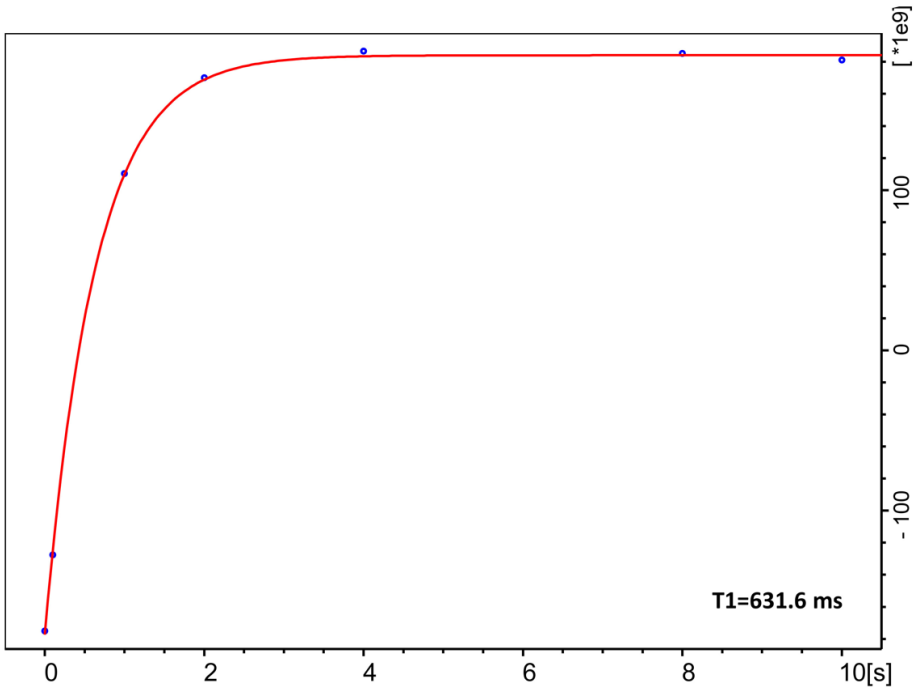

Figure 4.3.Peak fitting of ^{31}P spectra from a T_1 experiment for POPC (10 mM).

Standard T_1 NMR offers limited insights into membrane dynamics. Measuring spin-lattice relaxation rates (R_1) across various magnetic fields can potentially be highly effective for identifying the time scales of diverse movements within the lipid bilayer [106]. In field cycling NMR, the sample is mechanically moved back and forth between the center of the probe, where it experiences a high magnetic field, and a position above the probe with a lower magnetic field. This process occurs during the delay times typically employed in conventional NMR, and then the sample is returned to the probe's center for the relaxation measurement at the reduced magnetic field [106].

Roberts and Redfield [107] previously analyzed how the ^{31}P relaxation rate for POPC and DOPMe lipids varied with the magnetic field, observing changes from

11.74 down to 0.003 T (**Figure 4.4**). Various movements contribute to nuclear magnetic relaxation dispersions (NMRDs), each associated with correlation times corresponding to the particular motion. The field-dependent ^{31}P R_1 value is a cumulative result of these individual NMRDs. Analysis of these NMRD values in the presence and absence of protein can provide information about how protein alters the motion of the phospholipids about their long axis [1].

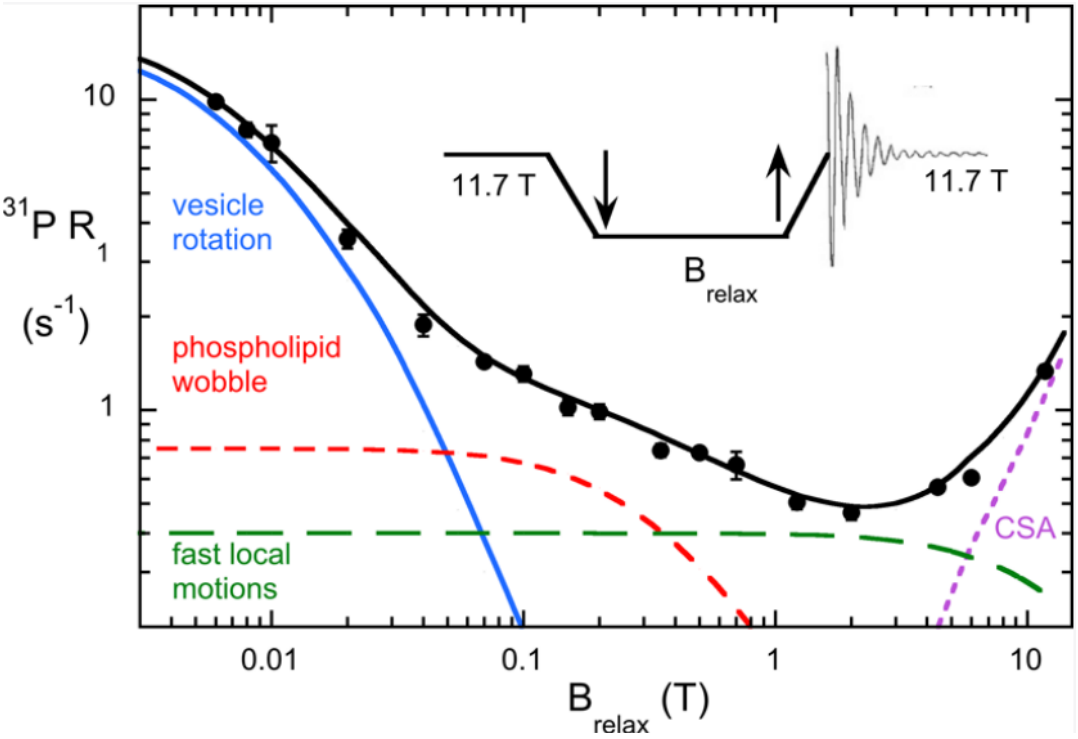

Figure 4.4. ^{31}P R_1 as function of magnetic field for 5 mM POPC in SUVs with 5mM d3-DOPMe. Image reprinted, with permission, from Ref. [108] © (2004) American Chemical Society Publications.

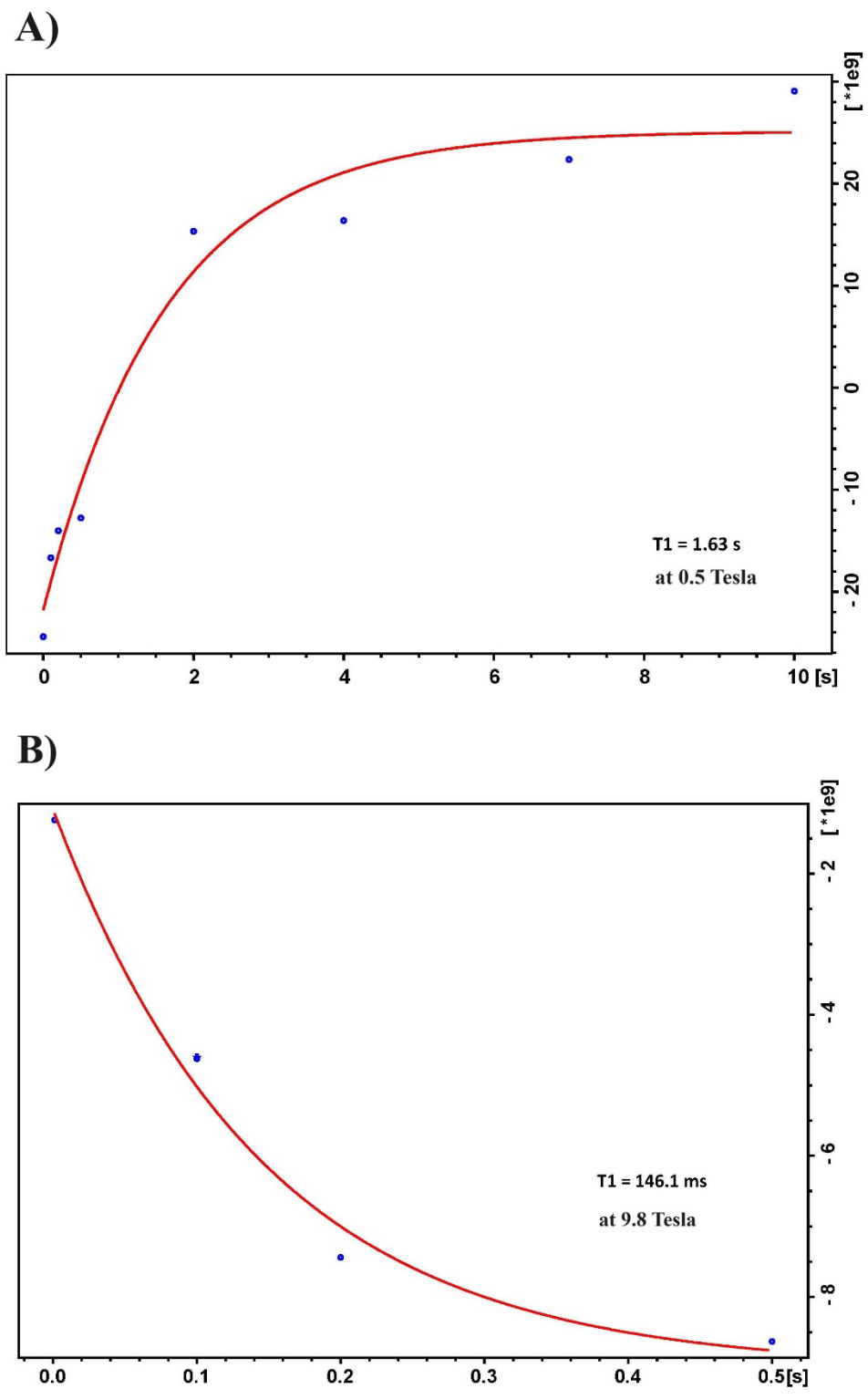

Figure 4.5. Peak fitting of ^{31}P high resolution field cycling NMR spectra from a T_1 experiment for POPC (10 mM) measured at: **A)** 0.5 T and **B)** at 9.8 T.

We collected some preliminary high-resolution ^{31}P field cycling NMR data at UMD's Biomolecular NMR using the pulse program described in the Appendix. We measured the relaxation time of POPC lipid at two different magnetic fields, 0.5 T (**Figure 4.5A**) and 9.8 T (**Figure 4.5B**). At 0.5 T, we obtained an R_1 of 0.61 s^{-1}, and at 9.8 T, 6.85 s^{-1}. R_1 recorded at 0.5 T was consistent with the literature value, but R_1 recorded at 9.8 T was higher than the one measured by Roberts's lab. This discrepancy may be due to the fewer time delays used in our fitting process. Regrettably, we were unable to measure R_1 in a different magnetic field due to the instrument's malfunction.

We had planned to complete these high-resolution field cycling NMR experiments, but the instrument is currently out of operation. Once the instrument is repaired, we will be able to measure the R_1 value of POPC lipid in the presence of spin-labeled Osh4 protein. As described in Chapter 3, we have already prepared a library of Osh4 mutants for spin labeling. Additionally, we can perform relaxation measurements with various lipids to study their interactions with Osh4.

4.3. Cryo-EM

Another method to investigate the interaction of the full-length Osh4 protein with model membranes is through the use of cryo-electron microscopy (cryo-EM). Cryo-EM is a microscopic method that allows the freezing of biological complexes in their natural state and capturing high-resolution images [109, 110]. This technique enables a thorough examination of binding sites and the mechanisms involved in protein

attachment to vesicle surfaces, including the structural changes during interaction [111].

For the Osh4 protein, it can be mixed with lipid vesicles and lipid nanodiscs to observe its dynamic interactions, such as binding to and detaching from the vesicles. By taking a series of cryo-EM images over time, we can gain insights into the sequence of events and the transient structures that occur during these processes [46]. Additionally, cryo-EM's capability to visualize samples in a hydrated state allows us to study the structural and biophysical aspects of protein-vesicle interactions in an environment that closely mimics physiological conditions.

Appendices

Field cycling T_1 ^{31}P NMR pulse program:

```
1 ze
2 d1
  p2 ph1
  50u LOCKH_ON
  50u TTL4_LOW   ;shuttle-up
  d21            ;shuttle-up time

 vd  ;relaxation delay

  50u TTL4_HIGH  ;shuttle-down
  d21   ;shuttle-down time
  d25           ;eq. time
       50u LOCKH_OFF

  p1 ph2
  go=2 ph31
  d11 wr #0 if #0 ivd
  lo to 1 times td1
exit
```

T_1 ^{31}P NMR pulse program:

```
;t1ir
;avance-version (12/01/11)
;T1 measurement using inversion recovery
;
;$CLASS=HighRes
;$DIM=2D
;$TYPE=
;$SUBTYPE=
;$COMMENT=


#include <Avance.incl>


"p2=p1*2"
"d11=30m"


"acqt0=-p1*2/3.1416"
```

```
1 ze
2 d1
  p2 ph1
  vd
  p1 ph2
  go=2 ph31
  d11 wr #0 if #0 ivd
  lo to 1 times td1
exit


ph1=0 2
ph2=0 0 2 2 1 1 3 3
ph31=0 0 2 2 1 1 3 3


;pl1 : f1 channel - power level for pulse (default)
;p1 : f1 channel -  90 degree high power pulse
;p2 : f1 channel - 180 degree high power pulse
;d1 : relaxation delay; 1-5 * T1
;d11: delay for disk I/O                    [30 msec]
;vd : variable delay, taken from vd-list
;ns: 8 * n
;ds: 4
;td1: number of experiments = number of delays in vd-list
;FnMODE: undefined

;define VDLIST

;this pulse program produces a ser-file (PARMOD = 2D)


;$Id: t1ir,v 1.13 2012/01/31 17:49:28 ber Exp $
```

List of Publications

1. **Konakbayeva D**, Allsopp R, Mihailescu E, Klauda JB, Karlsson AJ. (2024). "Elucidating of the lipid-binding mechanism of the ALPS-like motif of Osh4 protein". *Journal of Molecular Biology*. In preparation

2. **Konakbayeva D,** Karlsson AJ. (2023). "Strategies and opportunities for engineering antifungal peptides for therapeutic applications." *Current Opinion in Biotechnology* 81: 102926. ***Journal impact factor: 9.740.*** (Citation=6)

List of Presentation

1. **Konakabyeva D**, Allsopp RJ, Mihailescu E, Klauda JB, Karlsson AJ. (2023). Investigating the membrane-binding mechanism of the ALPS Peptide of Osh4. AIChE Annual Meeting, Orlando, FL, USA.

2. Loveland A *(undergraduate mentee),* **Konakabyeva D**, Klauda JB, Karlsson AJ. (2023). Comparison of GST and SUMO fusion tags for enhanced yield and purity of recombinant Osh4. AIChE Annual Meeting, Orlando, FL, USA.

3. **Konakabyeva D**, Allsopp RJ, Klauda JB, Karlsson AJ. (2022). Experimental investigation of the mechanism of lipid-binding of the ALP-like motif of Osh4 protein. BPS Annual Meeting, San Francisco, CA, USA.

4. Allsopp RJ, **Konakbayeva D**, Karlsson AJ, Klauda JB. (2022). Computational study of membrane binding and free energy of amphipathic helix (ALPS) on Osh4 to varied lipid bilayers. BPS Annual Meeting, San Francisco, CA, USA.

5. **Konakbayeva D**, Karlsson AJ, and Jeffery Klauda JB (2019). Studies on the Membrane-binding of Osh4 Protein. Graduate Open House, University of Maryland, MD, USA

References

[1] Watson H. Biological membranes. Essays Biochem. 2015;59:43-69.

[2] Cheng X, Smith JC. Biological membrane organization and cellular signaling. Chem Rev. 2019;119:5849-80.

[3] Castro BM, Torreno-Pina JA, van Zanten TS, Gracia-Parajo MF. Biochemical and imaging methods to study receptor membrane organization and association with lipid rafts. Methods Cell Biol. 2013;117:105-22.

[4] Alberts B. Molecular biology of the cell: Garland science; 2017.

[5] Payne S. Viruses: Academic Press; 2017. p. 23-35.

[6] Westra M, Gutierrez Y, MacGillavry HD. Contribution of membrane lipids to postsynaptic protein organization. Front Synaptic Neurosci. 2021;13:790773.

[7] Dufourc EJ. Sterols and membrane dynamics. J Chem Biol. 2008;1:63-77.

[8] Cheng Y, Li M, Wang S, Peng H, Reid S, Ni N, et al. Carbohydrate biomarkers for future disease detection and treatment. Sci China Chem. 2010;53:3-20.

[9] Karmakar S, Klauda JB. Modeling the membrane binding mechanism of a lipid transport protein Osh4 to single membranes. Biophys J. 2022;121:1560-75.

[10] Fadeel B, Xue D. The ins and outs of phospholipid asymmetry in the plasma membrane: roles in health and disease. Crit Rev Biochem Mol Biol. 2009;44:264-77.

[11] Rivel T, Ramseyer C, Yesylevskyy S. The asymmetry of plasma membranes and their cholesterol content influence the uptake of cisplatin. Sci Rep. 2019;9:5627.

[12] Manno S, Takakuwa Y, Mohandas N. Identification of a functional role for lipid asymmetry in biological membranes: Phosphatidylserine-skeletal protein interactions modulate membrane stability. Proc Natl Acad Sci U S A. 2002;99:1943-8.

[13] Zinser E, Sperka-Gottlieb CD, Fasch EV, Kohlwein SD, Paltauf F, Daum G. Phospholipid synthesis and lipid composition of subcellular membranes in the unicellular eukaryote *Saccharomyces cerevisiae*. J Bacteriol. 1991;173:2026-34.

[14] Milton Jr H, Stiles CD. Molecular dynamics in biological membranes: Springer Science & Business Media; 2012.

[15] Singer SJ, Nicolson GL. The fluid mosaic model of the structure of cell membranes. Science. 1972;175:720-31.

[16] Vance JE. Phospholipid synthesis and transport in mammalian cells. Traffic. 2015;16:1-18.

[17] Prinz WA. Lipid trafficking sans vesicles: where, why, how? Cell. 2010;143:870-4.

[18] Reinisch KM, Prinz WA. Mechanisms of nonvesicular lipid transport. J Cell Biol. 2021;220.

[19] Lev S. Non-vesicular lipid transport by lipid-transfer proteins and beyond. Nat Rev Mol Cell Biol. 2010;11:739-50.

[20] Oshima A, Nakashima H, Sumitomo K. Evaluation of lateral diffusion of lipids in continuous membranes between freestanding and supported areas by fluorescence recovery after photobleaching. Langmuir. 2019;35:11725-34.

[21] Contreras FX, Sanchez-Magraner L, Alonso A, Goni FM. Transbilayer (flip-flop) lipid motion and lipid scrambling in membranes. FEBS Lett. 2010;584:1779-86.

[22] Toulmay A, Prinz WA. A conserved membrane-binding domain targets proteins to organelle contact sites. J Cell Sci. 2012;125:49-58.

[23] Monje-Galvan V, Klauda JB. Peripheral membrane proteins: tying the knot between experiment and computation. Biochim Biophys Acta. 2016;1858:1584-93.

[24] Wong LH, Gatta AT, Levine TP. Lipid transfer proteins: the lipid commute via shuttles, bridges and tubes. Nat Rev Mol Cell Biol. 2019;20:85-101.

[25] Raychaudhuri S, Prinz WA. The diverse functions of oxysterol-binding proteins. Annu Rev Cell Dev Biol. 2010;26:157-77.

[26] Subra M, Antonny B, Mesmin B. New insights into the OSBP–VAP cycle. Curr Opin Cell Biol. 2023;82:102172.

[27] Singh RP, Poh YP, Sinha SD, Wideman JG. Evolutionary history of oxysterol-binding proteins reveals complex history of duplication and loss in animals and fungi. Contact (Thousand Oaks). 2023;6:25152564221150428.

[28] Beh CT, Cool L, Phillips J, Rine J. Overlapping functions of the yeast oxysterol-binding protein homologues. Genetics. 2001;157:1117-40.

[29] Lehto M, Olkkonen VM. The OSBP-related proteins: a novel protein family involved in vesicle transport, cellular lipid metabolism, and cell signalling. Biochim Biophys Acta. 2003;1631:1-11.

[30] Raychaudhuri S, Im YJ, Hurley JH, Prinz WA. Nonvesicular sterol movement from plasma membrane to ER requires oxysterol-binding protein-related proteins and phosphoinositides. J Cell Biol. 2006;173:107-19.

[31] Ngo MH, Colbourne TR, Ridgway ND. Functional implications of sterol transport by the oxysterol-binding protein gene family. Biochem J. 2010;429:13-24.

[32] Cho W, Stahelin RV. Membrane-protein interactions in cell signaling and membrane trafficking. Annu Rev Biophys Biomol Struct. 2005;34:119-51.

[33] Drin G, Casella JF, Gautier R, Boehmer T, Schwartz TU, Antonny B. A general amphipathic alpha-helical motif for sensing membrane curvature. Nat Struct Mol Biol. 2007;14:138-46.

[34] Bigay J, Antonny B. Curvature, lipid packing, and electrostatics of membrane organelles: defining cellular territories in determining specificity. Dev Cell. 2012;23:886-95.

[35] Bigay J, Casella JF, Drin G, Mesmin B, Antonny B. ArfGAP1 responds to membrane curvature through the folding of a lipid packing sensor motif. EMBO J. 2005;24:2244-53.

[36] Vanni S, Vamparys L, Gautier R, Drin G, Etchebest C, Fuchs PF, et al. Amphipathic lipid packing sensor motifs: probing bilayer defects with hydrophobic residues. Biophys J. 2013;104:575-84.

[37] Paloncyova M, DeVane R, Murch B, Berka K, Otyepka M. Amphiphilic drug-like molecules accumulate in a membrane below the head group region. J Phys Chem B. 2014;118:1030-9.

[38] Jackson CL, Walch L, Verbavatz JM. Lipids and their trafficking: an integral part of cellular organization. Dev Cell. 2016;39:139-53.

[39] Varnai P, Toth B, Toth DJ, Hunyady L, Balla T. Visualization and manipulation of plasma membrane-endoplasmic reticulum contact sites indicates the presence of additional molecular components within the STIM1-Orai1 complex. J Biol Chem. 2007;282:29678-90.

[40] Rogaski B, Klauda JB. Membrane-binding mechanism of a peripheral membrane protein through microsecond molecular dynamics simulations. J Mol Biol. 2012;423:847-61.

[41] Ghaemmaghami S, Huh WK, Bower K, Howson RW, Belle A, Dephoure N, et al. Global analysis of protein expression in yeast. Nature. 2003;425:737-41.

[42] Im YJ, Raychaudhuri S, Prinz WA, Hurley JH. Structural mechanism for sterol sensing and transport by OSBP-related proteins. Nature. 2005;437:154-8.

[43] de Saint-Jean M, Delfosse V, Douguet D, Chicanne Gt, Payrastre B, Bourguet W, et al. Osh4p exchanges sterols for phosphatidylinositol 4-phosphate between lipid bilayers. The Journal of Cell Biology. 2011;195:965-78.

[44] Schulz TA, Choi M-G, Raychaudhuri S, Mears JA, Ghirlando R, Hinshaw JE, et al. Lipid-regulated sterol transfer between closely apposed membranes by oxysterol-binding protein homologues. J Cell Biol. 2009;187:889-903.

[45] Allsopp R, Klauda JB. Impact of PIP2 lipids, force field parameters, and mutational analysis on the binding of the Osh4's α6-α7 domain. J Phys Chem B. 2021;125:5296-308.

[46] Matthies D, Bae C, Toombes GE, Fox T, Bartesaghi A, Subramaniam S, et al. Single-particle cryo-EM structure of a voltage-activated potassium channel in lipid nanodiscs. Elife. 2018;7.

[47] Ranjbar B, Gill P. Circular dichroism techniques: biomolecular and nanostructural analyses- a review. Chem Biol Drug Des. 2009;74:101-20.

[48] Kelly SM, Price NC. The use of circular dichroism in the investigation of protein structure and function. Curr Protein Pept Sci. 2000;1:349-84.

[49] Wei Y, Thyparambil AA, Latour RA. Protein helical structure determination using CD spectroscopy for solutions with strong background absorbance from 190 to 230 nm. Biochim Biophys Acta. 2014;1844:2331-7.

[50] Corrêa DH, Ramos CH. The use of circular dichroism spectroscopy to study protein folding, form and function. Afr J Biochem Res. 2009;3.

[51] Rodger A, Marrington R, Roper D, Windsor S. Circular dichroism spectroscopy for the study of protein-ligand interactions. Methods Mol Biol. 2005;305:343-64.

[52] Wallace BA, Lees JG, Orry AJ, Lobley A, Janes RW. Analyses of circular dichroism spectra of membrane proteins. Protein Sci. 2003;12:875-84.

[53] Siaw HMH, Raghunath G, Dyer RB. Peripheral protein unfolding drives membrane bending. Langmuir. 2018;34:8400-7.

[54] Miles AJ, Wallace BA. Circular dichroism spectroscopy of membrane proteins. Chem Soc Rev. 2016;45:4859-72.

[55] Davidson WS, Jonas A, Clayton DF, George JM. Stabilization of alpha-synuclein secondary structure upon binding to synthetic membranes. J Biol Chem. 1998;273:9443-9.

[56] Kraft CA, Garrido JL, Leiva-Vega L, Romero G. Quantitative analysis of protein-lipid interactions using tryptophan fluorescence. Sci Signal. 2009;2:pl4.

[57] Christiaens B, Symoens S, Verheyden S, Engelborghs Y, Joliot A, Prochiantz A, et al. Tryptophan fluorescence study of the interaction of penetratin peptides with model membranes. Eur J Biochem. 2002;269:2918-26.

[58] Zhao H, Kinnunen PK. Binding of the antimicrobial peptide temporin L to liposomes assessed by Trp fluorescence. J Biol Chem. 2002;277:25170-7.

[59] Ladokhin AS, Jayasinghe S, White SH. How to measure and analyze tryptophan fluorescence in membranes properly, and why bother? Anal Biochem. 2000;285:235-45.

[60] Galdiero S, Falanga A, Cantisani M, Vitiello M, Morelli G, Galdiero M. Peptide-lipid interactions: experiments and applications. Int J Mol Sci. 2013;14:18758-89.

[61] Pignataro MF, Herrera MG, Dodero VI. Evaluation of peptide/protein self-assembly and aggregation by spectroscopic methods. Molecules. 2020;25.

[62] Ladokhin AS. Fluorescence spectroscopy in peptide and protein analysis. Encyclopedia of analytical chemistry 2000. p. 5762-79.

[63] Killian JA, Keller RC, Struyve M, de Kroon AI, Tommassen J, de Kruijff B. Tryptophan fluorescence study on the interaction of the signal peptide of the Escherichia coli outer membrane protein PhoE with model membranes. Biochemistry. 1990;29:8131-7.

[64] Wieprecht T, Seelig J. Isothermal titration calorimetry for studying interactions between peptides and lipid membranes. Curr Top Membr. 2002;52:31-56.

[65] Velazquez-Campoy A, Ohtaka H, Nezami A, Muzammil S, Freire E. Isothermal titration calorimetry. Curr Protoc Cell Biol. 2004;Chapter 17:Unit 17-8.

[66] Boudker O, Oh S. Isothermal titration calorimetry of ion-coupled membrane transporters. Methods. 2015;76:171-82.

[67] Linkuviene V, Krainer G, Chen WY, Matulis D. Isothermal titration calorimetry for drug design: Precision of the enthalpy and binding constant measurements and comparison of the instruments. Anal Biochem. 2016;515:61-4.

[68] Srivastava VK, Yadav R. Isothermal titration calorimetry. Data processing handbook for complex biological data sources: Elsevier; 2019. p. 125-37.

[69] Mertins O, Dimova R. Binding of chitosan to phospholipid vesicles studied with isothermal titration calorimetry. Langmuir. 2011;27:5506-15.

[70] Swamy MJ, Sankhala RS, Singh BP. Thermodynamic analysis of protein-lipid interactions by isothermal titration calorimetry. Methods Mol Biol. 2019;2003:71-89.

[71] Atri MS, Saboury AA, Ahmad F. Biological applications of isothermal titration calorimetry. Phys Chem Res. 2015;3:319-30.

[72] Saponaro A. Isothermal titration calorimetry: a biophysical method to characterize the interaction between label-free biomolecules in solution. Bio Protoc. 2018;8:e2957.

[73] Liu W, Jiang J, Lin Y, You Q, Wang L. Insight into thermodynamic and kinetic profiles in small-molecule optimization. J Med Chem. 2022;65:10809-47.

[74] Lee M. X-Ray diffraction for materials research: from fundamentals to applications: CRC Press; 2017.

[75] Brown JG. X-rays and their applications: Springer Science & Business Media; 2012.

[76] Perutz MF. How WL Bragg invented X-ray analysis. Acta Crystallogr, Sect A: Foundations of Crystallography. 1990; 46:633-43.

[77] Pope CG. X-ray diffraction and the Bragg equation. J Chem Educ. 1997;74:129-31.

[78] Zhao C, Wang B, Zhong S, Akhtaruzzaman M, Liang W, Chen H. NDT studies of nanoscale polymeric coatings. Polymer-Based Nanoscale Materials for Surface Coatings2023.

[79] Wiener MC, White SH. Fluid bilayer structure determination by the combined use of x-ray and neutron diffraction. I. Fluid bilayer models and the limits of resolution. Biophys J. 1991;59:162-73.

[80] Wiener MC, White SH. Fluid bilayer structure determination by the combined use of x-ray and neutron diffraction. II. "Composition-space" refinement method. Biophys J. 1991;59:174-85.

[81] Comert F, Greenwood A, Maramba J, Acevedo R, Lucas L, Kulasinghe T, et al. The host-defense peptide piscidin P1 reorganizes lipid domains in membranes and decreases activation energies in mechanosensitive ion channels. J Biol Chem. 2019;294:18557-70.

[82] Mihailescu M, Sorci M, Seckute J, Silin VI, Hammer J, Perrin BS, Jr., et al. Structure and function in antimicrobial piscidins: histidine position, directionality of membrane insertion, and pH-dependent permeabilization. J Am Chem Soc. 2019;141:9837-53.

[83] Mihailescu M, Krepkiy D, Milescu M, Gawrisch K, Swartz KJ, White S. Structural interactions of a voltage sensor toxin with lipid membranes. Proc Natl Acad Sci U S A. 2014;111:E5463-70.

[84] Comert F, Heinrich F, Chowdhury A, Schoeneck M, Darling C, Anderson KW, et al. Metallated anticancer peptides: an expanded mechanism that encompasses physical and chemical bilayer disruption. FASEB journal. 2022;36.

[85] Zhang L, Tian X, Wang C. In vitro application of Langmuir monolayer model: the interfacial behavior of myelin basic protein with a plasma membrane model. J Membr Biol. 2022;255:71-8.

[86] Monje-Galvan V, Klauda JB. Preferred binding mechanism of Osh4's amphipathic lipid-packing sensor motif, insights from molecular dynamics. J Phys Chem B. 2018;122:9713-23.

[87] Wildermuth KD, Monje-Galvan V, Warburton LM, Klauda JB. Effect of membrane lipid packing on stable binding of the ALPS peptide. J Chem Theory Comput. 2019;15:1418-29.

[88] King GI, Jacobs RE, White SH. Hexane dissolved in dioleoyllecithin bilayers has a partial molar volume of approximately zero. Biochemistry. 1985;24:4637-45.

[89] Jacobs RE, White SH. The Nature of the hydrophobic binding of small peptides at the bilayer interface - implications for the insertion of transbilayer helices. Biochemistry. 1989;28:3421-37.

[90] Tatulian SA. Interfacial enzymes: membrane binding, orientation, membrane insertion, and activity. Methods Enzymol. 2017;583:197-230.

[91] MicroCal. ITC data analysis in Origin® tutorial guide version 7.0. 2004.

[92] Möller M, Denicola A. Protein tryptophan accessibility studied by fluorescence quenching. Biochem Mol Biol Educ. 2002;30:175-8.

[93] Breukink E, van Kraaij C, van Dalen A, Demel RA, Siezen RJ, de Kruijff B, et al. The orientation of nisin in membranes. Biochemistry. 1998;37:8153-62.

[94] Ludtke S, He K, Huang H. Membrane thinning caused by magainin 2. Biochemistry. 1995;34:16764-9.

[95] Hristova K, Dempsey CE, White SH. Structure, location, and lipid perturbations of melittin at the membrane interface. Biophys J. 2001;80:801-11.

[96] Garidel P, Eiperle A, Blech M, Seelig J. Thermal and chemical unfolding of a monoclonal IgG1 antibody: application of the multistate Zimm-Bragg theory. Biophys J. 2020;118:1067-75.

[97] Esposito D, Chatterjee DK. Enhancement of soluble protein expression through the use of fusion tags. Curr Opin Biotechnol. 2006;17:353-8.

[98] Young CL, Britton ZT, Robinson AS. Recombinant protein expression and purification: a comprehensive review of affinity tags and microbial applications. Biotechnol J. 2012;7:620-34.

[99] Zhao X, Li G, Liang S. Several affinity tags commonly used in chromatographic purification. J Anal Methods Chem. 2013;2013:581093.

[100] Butt TR, Edavettal SC, Hall JP, Mattern MR. SUMO fusion technology for difficult-to-express proteins. Protein Expr Purif. 2005;43:1-9.

[101] Marblestone JG, Edavettal SC, Lim Y, Lim P, Zuo X, Butt TR. Comparison of SUMO fusion technology with traditional gene fusion systems: enhanced expression and solubility with SUMO. Protein Sci. 2006;15:182-9.

[102] Han X, Mihailescu M, Hristova K. Neutron diffraction studies of fluid bilayers with transmembrane proteins: structural consequences of the achondroplasia mutation. Biophys J. 2006;91:3736-47.

[103] Krepkiy D, Mihailescu M, Freites JA, Schow EV, Worcester DL, Gawrisch K, et al. Structure and hydration of membranes embedded with voltage-sensing domains. Nature. 2009;462:473-9.

[104] Cruz J, Mihailescu M, Wiedman G, Herman K, Searson PC, Wimley WC, et al. A membrane-translocating peptide penetrates into bilayers without significant bilayer perturbations. Biophys J. 2013;104:2419-28.

[105] Rosen BR, Brady TJ. Principles of nuclear magnetic resonance for medical application. Semin Nucl Med. 1983;13:308-18.

[106] Sivanandam VN, Cai J, Redfield AG, Roberts MF. Phosphatidylcholine "wobble" in vesicles assessed by high-resolution 13C field cycling NMR spectroscopy. J Am Chem Soc. 2009;131:3420-1.

[107] Roberts MF, Redfield AG. High-resolution ^{31}P field cycling NMR as a probe of phospholipid dynamics. J Am Chem Soc. 2004;126:13765-77.

[108] Roberts MF, Cai J, S VN, Khan HM, Reuter N, Gershenson A, et al. Phospholipids in motion: high-resolution (31)P NMR field cycling studies. J Phys Chem B. 2021;125:8827-38.

[109] Bai XC, McMullan G, Scheres SH. How cryo-EM is revolutionizing structural biology. Trends Biochem Sci. 2015;40:49-57.

[110] Benjin X, Ling L. Developments, applications, and prospects of cryo-electron microscopy. Protein Sci. 2020;29:872-82.

[111] Yao X, Fan X, Yan N. Cryo-EM analysis of a membrane protein embedded in the liposome. Proc Natl Acad Sci USA. 2020;117:18497-503.